ABSTRACT

MALHOTRA, BHARAT. Plasmonic Enhancement of Silicon Solar Cells with Metal Nanoparticles. (Under the direction of Dr. John F. Muth.)

Plasmonic effects are investigated to improve the absorption of long wavelength light in silicon solar cells. Metal nanoparticles on top of the solar cell can be incorporated to capture and couple more light into the cell by forward scattering. The interaction of the light with the metal nanoparticles is the maximum near the wavelengths corresponding to the metal plasmon resonance frequency. This frequency can be tuned by changing the size and shape of the nanoparticle and the dielectric environment surrounding it. An enhancement in the electric field can be observed near the metal particles which determine the extent of coupling to some extent. The External Quantum Efficiency (EQE) can thus be improved at longer wavelengths where the performance is poor.

This research presents a comprehensive study about the enhancement of the photocurrent of silicon solar cells by exploiting the optical properties of metal nanoparticles. The factors which affect the plasmon resonance, namely the choice of metal, size of the particle and the dielectric environment are investigated in this study and the results are presented.

An overall 3.25 % increase in the photocurrent of mono crystalline solar cells was demonstrated in this study. A high EQE and photocurrent was observed above 800nm for almost all the samples. A 2.5 fold increase in photocurrent was observed at 1100 nm and a 3 fold increase at 1130 nm.

Plasmonic Enhancement of Silicon Solar Cells with Metal Nanoparticles

by
Bharat Malhotra

A thesis submitted to the Graduate Faculty of
North Carolina State University
in partial fulfillment of the
requirements for the degree of
Master of Science

Electrical Engineering

Raleigh, North Carolina

2011

APPROVED BY:

_____	_____
Dr. Salah Bedair	Dr. Michael Escuti

_____
Dr. John F. Muth
Committee Chair

DEDICATION

To my dad, mom and brother. This would not have been possible without your support and prayers.

BIOGRAPHY

Bharat Malhotra was born in New Delhi, India in March 1988. He received his Bachelor of Engineering (B.E.) degree in Electronics and Communication Engineering from Birla Institute of Technology, Ranchi, India in June 2009. In August 2009, he began his graduate studies in Electrical Engineering at North Carolina State University with a focus on Nanoelectronics. In the summer of 2010, he interned with Semprius, Durham, NC and worked with innovative solar technology. While working towards his Masters degree, he worked on his thesis under the guidance of Dr. John F. Muth. His research interest includes Silicon and non-Silicon based solar cells, process integration and nanoscale device design. He plans to further pursue his career in Nanotechnology and other related fields.

ACKNOWLEDGEMENTS

Firstly, I thank my parents for the much needed motivation throughout the duration of my graduate studies and particularly thesis work. It was their love and support that helped me during stressful times.

I sincerely want to thank my advisor Dr. John Muth for believing in me and giving me the opportunity to work with him. It was his timely guidance and support because of which I could get this far in the project and finish it. I am grateful to him for his positive attitude, kind support and encouragement for innovative and 'out of box' thinking.

I want to thank Dr. Michael Escuti for agreeing to be on my committee and giving his technical insights in this project. I would also like to thank Dr. Robert Kolbas for imparting conceptual knowledge through his course and igniting my interest in Nanoelectronics.

I would like to thank Dr. Etienne Menard of Semprius, who provided me with solar cell samples and helped me develop technical skills during my internship period at Semprius.

I am highly grateful to Joe Mathews for teaching me new tools and equipment. My research could have been completed in a timely manner without his help. A word of thanks also goes out to Yi Lou, Yan Wang and Haojun Luo for helping me in the various experiments.

Lastly, I would want to thank Geoff Bradshaw of Dr. Salah Bedair's group for taking time out of his schedule and helping me on many experiments thus enabling me to get good results.

TABLE OF CONTENTS

LIST OF TABLES

LIST OF FIGURES

CHAPTER 1

INTRODUCTION

1.10 Overview

Solar energy has tremendous potential to replace the traditional fossil fuels as sources of power. This can reduce pollution and mitigate the global warming crisis currently plaguing our present. Solar cells provide clean renewable energy and can enable many applications. In 2010, solar photovoltaics generated electricity in more than 100 countries but comprised only a tiny fraction of the 4.8 TW produced globally from all sources. It is the fastest growing power-generation technology in the world. According to a new report published by the International Energy Agency (IEA), solar power is expected to provide almost a quarter of the world's electricity supplies by 2050. Photovoltaics could thus make a considerable contribution to solving the energy problem that our society faces in the next generation. Currently 90 % of the solar cell market is based on crystalline silicon wafers, with thickness of 200-300 µm. Around 40% of the cost of a solar module made from crystalline silicon is the cost of the silicon wafers [1]. While research continues to provide high efficiency solar cells, efforts are also underway to reduce the cost per watt of energy produced. One simple way is to reduce the amount of semiconductor material required to fabricate these solar cells, or in other words, use thin film solar cells.

Thin-film solar cells are made from a variety of semiconductors including amorphous and poly-crystalline Si, GaAs, CdTe and $CuInSe_2$, as well as organic semiconductors [2]. The thicknesses of these solar cells are in the range of 1-3 µm. Thin-film solar cells reduce the production cost since less semiconducting material is needed to fabricate them but also reduces the efficiency. This is mainly due to its poor absorption ability. As cells become thinner, the light trapping becomes more important. More efficient light trapping

mechanisms are therefore required to improve its performance compared to the wafer-based solar cells. Usual methods such as surface texturing for light trapping cannot be applied to thin-film cells. Micron scale texturing has a relatively large size, while submicron surface texturing inevitably increases the surface area and hence the minority carrier recombination on the surface [3]. Texturing also degrades the quality of the semiconductor material to some extent reducing efficiency.

A more promising way is to use surface plasmons to enhance the optical absorption by light trapping in the thin-film solar cells. Recent experimental studies on both organic and inorganic solar cells have shown that the performance of thin-film cells can be improved significantly by metallic nanoparticles deposited on top of the photo-active layer [3]. This allows more light to be collected and thus absorbed in the solar cell.

The field of plasmonics has emerged rapidly in the past few years and is playing a vital role in new technologies. Studies are starting to illustrate the coupling of plasmons to optical emitters; plasmon focusing; hybridized plasmonic modes in nanoscale metal shells; nanoscale waveguiding; nanoscale optical antennas; plasmonic integrating circuits; nanoscale switches; plasmonic lasers; surface plasmon enhanced light emitting diodes; imaging below the diffraction limit and materials with negative refractive index [2].

Surface plasmons are collective oscillations of the electrons and behave like surface electromagnetic waves which propagate in the direction parallel to the metal/dielectric layer. Due to the resonant interaction between the incident light and the metal nanoparticles, there is an enhancement of scattering and local fields .This directly contributes to the amount of photocurrent generated as more light can be collected and absorbed. The physics behind this concept is affected by many different factors such as the size, shape and distribution of the particles, the dielectric spacer between the metal and semiconductor and the type of metal nanoparticles used.

The main point is that, silicon is a poor absorber of light especially in the near band gap region so the plasmonic enhancement becomes even more relevant at longer wavelengths. A major advantage of plasmonic light trapping is that the metal nanoparticles can be deposited at the final stage of the device fabrication process without the need to change any processing conditions or compromise the material or surface quality. Moreover, the optical properties of the surface plasmons are independent of the electrical properties of the solar cell and hence can be optimized independent of the cell structure.

1.11 Goal of Dissertation

The rapid emerging field of plasmonics has demonstrated the enhancement in optical absorption in both organic and inorganic solar cells. This stems from the improved light trapping techniques provided by metal nano particles deposited on the front of the solar cells. Due to the resonant interaction of the incident light and these metal nanoparticles, light can be coupled into the photo-active layer of the solar cell providing enhancement in photoelectric current. The resonant nature of the metal nanoparticles makes it an efficient and a flexible tool for solar cell applications and can be used to manipulate the light trapping and energy conversion efficiency. The plasmon frequencies of these nanoparticles can be tuned (by changing their size, shape, arrangement or by changing the dielectric environment) to modify the spectral profile of the absorbed power in the photo-active layer, as well as the total absorbed power [3].

The absorption of light at long wavelengths (above 800 nm) by Si solar cells can be significantly enhanced by surface plasmons. Such an effect are not only limited to solar cells, it can also be incorporated for Si photodiodes and can help in improving their sensitivities at long wavelengths.

The goal of the this research is to boost the efficiency of silicon based solar cells near the band gap region thus enabling them to compete with the other existing high efficiency solar cells in the market. Since silicon is the most widely used material in the semiconductor industry, any attempt to improve the effectiveness of these silicon based solar cells would be generally accepted.

This dissertation provides a systematic study in the field of plasmonics and its applicability to solar cells. The effect of varying metal nanoparticle sizes and distribution and also the change in dielectric environment on the photoelectric current generation is investigated.

The fabrication procedure involved is relatively simple, cost friendly and can be introduced in the later part of the fabrication process thus not interfering with any existing methods of solar cell production.

1.12 References

[1] K. R. Catchpole and A. Polman, "Plasmonic solar cells," Optics Express, vol. 16, pp. 21793- 21800, Dec 2008.

[2] H. A. Atwater and A. Polman, "Plasmonics for improved photovoltaic devices," Nature Materials, vol. 9, pp. 205-213, Mar 2010.

[3] Y. A. Akimov, et al., "Enhancement of optical absorption in thin-film solar cells through the excitation of higher-order nanoparticle plasmon modes," Optics Express, vol. 17, pp. 10195-10205, Jun 2009.

CHAPTER 2

BACKGROUND

This chapter provides an introduction to the various principles and device physics of the processes under. The first section discusses concepts relating to solar cells and its operation mechanism. The second section throws light into the theory of plasmonics and the various factors affecting it. Finally the third section deals with the viability of the plasmonics for solar cell applications.

2.10 Solar Cells

Photovoltaics is the process of converting sunlight directly into electricity using solar cells. It is still a relative newcomer, with the first practical photovoltaic devices demonstrated in the 1950s. Research and development of photovoltaics received its first major boost from the space industry in the 1960s which required a power supply separate from grid power for satellite applications. These space solar cells were several thousand times more expensive than they are today and the perceived need for an electricity generation method apart from grid power was still a decade away, but solar cells became an interesting scientific variation to the rapidly expanding silicon transistor development with several potentially specialized niche markets [1]. It took the oil crisis in the 1970s to focus world attention on the desirability of alternate energy sources for terrestrial use, which in turn promoted the investigation of photovoltaics as a means of generating terrestrial power. Although the oil crisis proved short-lived and the financial incentive to develop solar cells lessened, solar cells had entered the arena as a power generating technology. Their application and advantage to the remote power supply area was quickly recognized and prompted the development of terrestrial photovoltaics industry. Small scale transportable applications (such as calculators and watches) were utilized and remote power applications began to benefit from photovoltaics.

In the 1980s research into silicon solar cells paid off and solar cells began to increase their efficiency. In 1985 silicon solar cells achieved the milestone of 20% efficiency. Over the next decade, the photovoltaic industry experienced steady growth rates of between 15% and 20%, largely promoted by the remote power supply market. The year 1997 saw a growth rate of 38% and today solar cells are recognized not only as a means for providing power and increased quality of life to those who do not have grid access, but they are also a means of significantly diminishing the impact of environmental damage caused by conventional electricity generation in advanced industrial countries [1]. The highest efficiency demonstrated by a state of the art solar cell today is around 41%. Figure 1 shows a National Renewable Energy Laboratory (NREL) compilation of the best research solar cell efficiency till date.

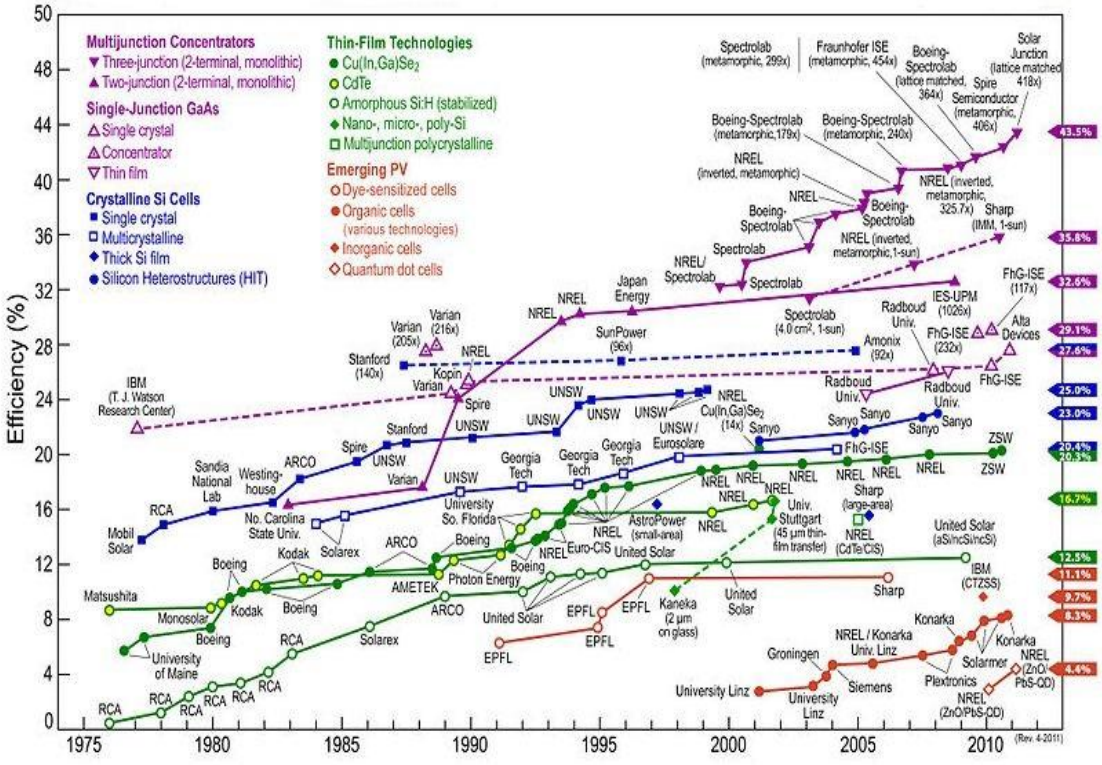

Figure 1.NREL compilation of the best solar cell efficiencies [13].

2.11 Photovoltaic Energy Conversion

Photovoltaic energy conversion is the direct production of electrical energy in the form of current and voltage from electromagnetic (infrared, visible, and ultraviolet light) energy. The four basic steps needed for photovoltaic energy conversion are [2]:

1. A light absorption process which causes an electronic transition in a material (the absorber) from a ground state to an excited state.

2. The conversion of the excited state into an electron-hole pair.

3. A discriminating transport mechanism; an applied or inherent electric field which causes the resulting free negative-charge carriers to move in one direction (to a contact that we will call the cathode) and the resulting free positive charge carriers to move in the other direction (to a contact that we will call the anode). The energetic, photogenerated negative-charge carriers arriving at the cathode result in electrons which travel through an external path (an electric circuit). While traveling this path, they lose their energy doing something useful at an electrical load, and finally they return to the anode of the cell.

4. At the anode, to maintain charge neutrality, the returning electrons complete the fourth step of photovoltaic energy conversion, by combining with an arriving positive-charge carrier.

2.12 Solar Radiation

Like all devices, solar cells need a driving force or energy to function. The energy supply for a solar cell is the photons coming from the sun. This input is distributed, in ways that depend on variables like latitude, time of day, and atmospheric conditions, over different wavelengths. The various distributions that are possible are called solar spectra [2]. Some common standard energy supplies from the sun, which are available at or on the earth, are plotted against wavelength (λ) in W/m^2 /nm spectra in Figure2a. An alternative photons/m^2 -

s/nm spectrum is seen in Figure 2b. The spectra in Figure 2a gives the power impacting per area (m^2) in a band of wavelengths 1 nm wide (the bandwidth $\Delta \lambda$) centered on each wavelength.

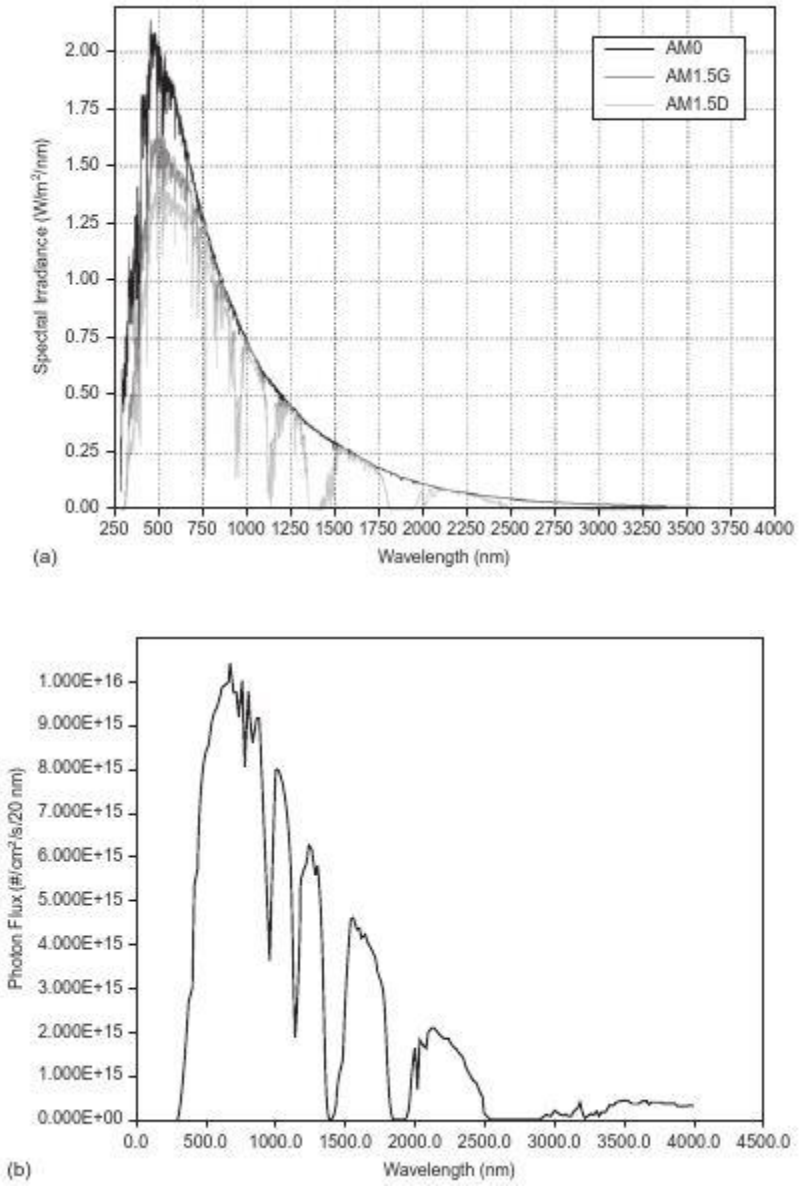

Figure 2.Solar energy spectra. (a) Data expressed in W/m/1 nm bandwidth for AM0 and for AM1.5G, and AM1.5D spectra (b) The AM1.5G data expressed in terms of impinging photons per second per cm^2 per 20nm bandwidth [2].

The spectrum in Figure 2b has been obtained from the AM1.5G spectrum of Figure 2a by converting power to photons per second per cm^2 and by using a bandwidth of 20 nm. Photon spectra Φ_0 (λ), exemplified by that in Figure 2b, are more convenient for solar cell assessments, because optimally one photon translates into one free electron–free hole pair via steps 1 and 2 (mentioned before) of the four steps needed for photovoltaic energy conversion.

The air mass coefficient defines the direct optical path length through the earth's atmosphere, expressed as a ratio relative to the path length vertically upwards, i.e. at the zenith (z). The air mass coefficient can be used to help characterize the solar spectrum after solar radiation has traveled through the atmosphere. The air mass coefficient is commonly used to characterize the performance of solar cells under standardized conditions, and is often referred to using the syntax "AM" followed by a number.

AM0: The spectrum outside the atmosphere, the 5,800 K black body, is referred to as "AM0", meaning "zero atmospheres". Solar cells used for space power applications, like those on communications satellites are generally characterized using AM0.

AM1: The spectrum after travelling through the atmosphere to sea level with the sun directly overhead is referred to, by definition, as "AM1". This means "one atmosphere". AM1 ($z=0°$) to AM1.1 ($z=25°$) is a useful range for estimating performance of solar cells in equatorial and tropical regions.

AM1.5: Solar panels do not generally operate under exactly one atmosphere's thickness if the sun is at an angle to the Earth's surface the effective thickness will be greater. "AM1.5", 1.5 atmosphere thickness, corresponds to a solar zenith angle of $z=48.2°$. The solar industry uses AM1.5 for all standardized testing of terrestrial solar panels [3], [4].

The ***AM1.5G*** (Global) spectrum is for terrestrial applications and includes direct and diffuse light. It integrates to 1000 W/m^2. The ***AM1.5D*** (Direct) spectrum is for terrestrial applications but includes direct light only. It integrates to 888 W/m^2 [2].

Having standard spectra allows the solar cell performance of one device to be compared to that of other devices and to be judged fairly, since the cells can be exposed to the same agreed-upon spectrum [2]. The comparisons can be done even in the laboratory since standard distributions can be duplicated using solar simulators.

2.13 Solar Cell Efficiency

A cross section of a typical solar cell is shown in Figure 3. The area of the photon impingement and the area of the current production are the same. The anti-reflection coating is employed at the top layer to reduce the reflective losses. The collecting electrodes (cathode and anode) are shown.

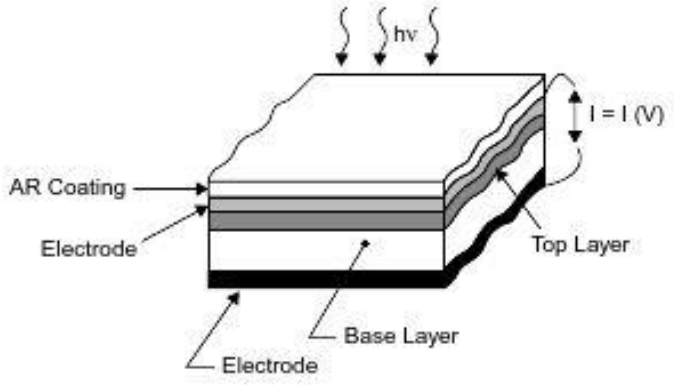

Figure 3. Cross section of a typical solar cell [2].

The total power P_{IN} per area impinging on a cell for a given photon spectrum $\Phi_0(\lambda)$ is the integral of the incoming energy per time per area per bandwidth over the entire photon spectrum;

$$\boldsymbol{P_{IN} = \int \frac{hc}{\lambda} \Phi_0 (\lambda)\, d\lambda} \qquad (2.1)$$

where an example of Φ_0 (λ), expressed as photons/time/area/bandwidth, is plotted in Figure 2b. In Equation 2.1 the quantity *h* is Planck's constant and *c* is the speed of light. The electrical power P_{OUT} per area produced by the cell of Figure 3 operating at the voltage *V* and delivering the current *I* as a result of this incoming solar power is the product of the current *I* times *V* divided by the cell area. By introducing the current density *J*, defined as I divided by the cell area:

$$\boldsymbol{P_{OUT} = JV} \qquad (2.2)$$

A plot of the possible J-V characteristic of the cell of Figure 3 can be seen in Figure 4. The points labeled J_{sc} and V_{oc} represent respectively, the cases of no voltage produced between the anode and cathode (i.e., the illuminated solar cell is short-circuited) and of no current flowing between the anode and cathode (i.e., the illuminated solar cell is open-circuited).

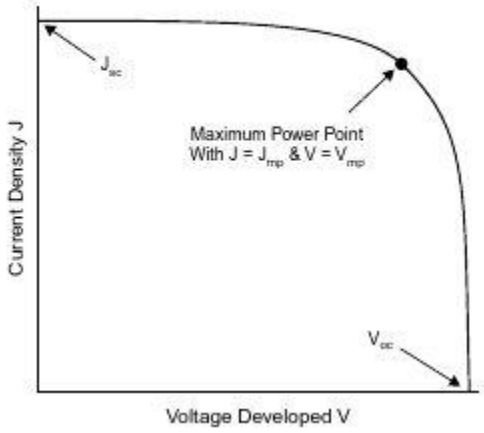

Figure 4. The current density-voltage (J-V) characteristic of the solar cell structure of Figure 3 under illumination [2].

The quantity P_{OUT} has its best value at the maximum power point shown by the current density J_{mp} and the voltage V_{mp} in the light J-V characteristic in Figure 4. This operating point gives the maximum obtainable current density-voltage product. Therefore, the best

thermodynamic efficiency η of the photovoltaic energy conversion process for the cell of Figure 20 is:

$$\boldsymbol{\eta = \frac{J_{mp} V_{mp}}{P_{IN}}} \qquad (2.3)$$

which assumes the photon impingement area and the area generating the current are the same. For cells collecting light over a larger area than that generating the current (i.e., for concentrator solar cells), this expression is replaced by

$$\boldsymbol{\eta = A_S \frac{J_{mp} V_{mp}}{A_C P_{IN}}} \qquad (2.4)$$

where A_S is the solar cell area generating current and A_C is the area collecting the photons. The advantage of a concentrator configuration lies in its being able to harvest more incoming solar power with a given cell size.

As can be seen from Figure 4, the ideal shape J-V characteristic would be a rectangle and would deliver a constant current density J_{sc} until the open circuit voltage V_{oc} is reached.

The fill factor (FF) measures how close a given characteristic is to conforming to the ideal rectangular J-V shape. The fill factor is given by

$$\boldsymbol{FF = \frac{J_{mp} V_{mp}}{V_{OC} I_{OC}}} \qquad (2.5)$$

By definition $FF \leq 1$

A fill factor value closer to 1 is desired.

2.14 Device Physics of p-n Junction Solar Cells

In this section the device physics for p-n junction solar cell would be discussed in detail. The p-n junction solar cell has a very basic structure and its operation can be easily understood. The structure for such a cell is shown in Figure 5.

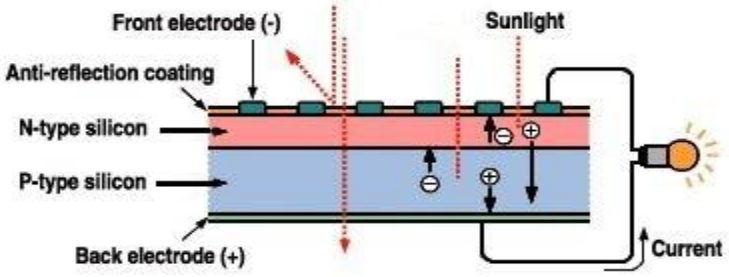

Figure 5. Typical structure for a p-n junction silicon solar cell.

The generation of current in the solar cell known as light generated current involves two key mechanisms (similar to the principle of photovoltaic energy generation). The first process involves the absorption of the photon to create an electron-hole pair, provided that the energy of the incoming photon is higher than the semiconductor band gap energy of the cell. The minority carriers: the electrons in the p-type material and holes in the n-type material are meta-stable and will only exist for a length of time equal to the minority carrier lifetime before they recombine. The light generated electron-hole pair can be lost and no current can be generated if the recombination occurs [1]. The second process is the collection of these carries by the p-n junction preventing this recombination. The carriers are separated by the action of the electric field existing at the p-n junction. If the light generated minority carrier reaches the p-n junction then it is swept across the junction by the electric field and now becomes a majority carrier. The energy band diagram of a p-n junction solar cell and its equivalent circuit diagram are shown in Figure 6. A constant current source (I_L) is in parallel with the junction. The source I_L results from the excitation of excess carriers by solar radiation; I_S is the diode saturation current and R_L is the load resistance.

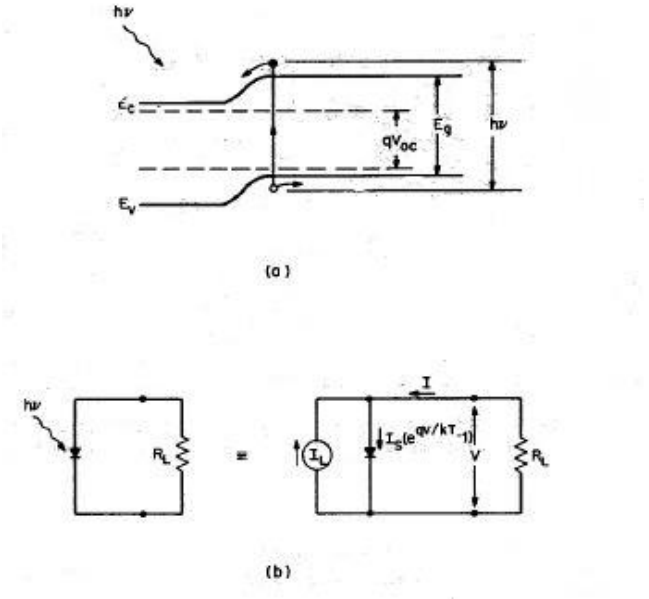

Figure 6. (a) Energy band diagram of a p-n junction solar cell under solar irradiation. (b) Idealized equivalent circuit of a solar cell [5].

Following the derivation by S.M Sze, the I-V characteristics of such a device is given by

$$\boldsymbol{I = I_S \left(e^{\frac{qV}{kT}} - 1\right) - I_L} \tag{2.6}$$

And

$$\boldsymbol{J_S = \frac{I_S}{A} = qN_C N_V \left(\frac{1}{N_A}\sqrt{\frac{D_n}{\tau_n}} + \frac{1}{N_D}\sqrt{\frac{D_p}{\tau_p}}\right) e^{-E_g/kT}} \tag{2.7}$$

Where A is the device area,

N_C and N_V are the effective density of states in the conduction and valence band respectively.

N_A and N_D are the acceptor and donor impurity density.

D_n and D_p are the electron and hole diffusion constants.

τ_n and τ_p are the electron and hole lifetime.

E_g is the band gap.

k is the Boltzmann constant.

T is the temperature.

From Equation 8 we can obtain the open-circuit voltage V_{OC} (I=0)

$$\boldsymbol{V_{OC} = \frac{kT}{q} ln\left(\frac{I_L}{I_S} + 1\right) \cong \frac{kT}{q} ln\,(\frac{I_L}{I_S})} \tag{2.8}$$

Hence for a given I_L, the open –circuit voltage increases logarithmically with decreasing saturation current I_S. The output power is given by

$$\boldsymbol{P = IV = I_S V\left(e^{\frac{qV}{kT}} - 1\right) - I_L V} \tag{2.9}$$

The maximum power output is P_m (= $I_m V_m$)

The condition for maximum power can be obtained when dP/dV=0 or

$$\boldsymbol{I_m = I_S \beta V_m e^{\beta V_m} \cong I_L\{1 - \frac{1}{\beta V_m}\}} \tag{2.10}$$

$$\boldsymbol{V_m = \frac{1}{\beta} ln\left(\frac{\frac{I_L}{I_S}+1}{1+\beta V_m}\right) \cong V_{oc} - \frac{1}{\beta} ln(1 + \beta V_m)} \tag{2.11}$$

where $\beta = q/kT$. The maximum power output P_m is then

$$\boldsymbol{P_m = I_m V_m \cong I_L\left[V_{oc} - \frac{1}{\beta} ln(1 + \beta V_m) - \frac{1}{\beta}\right] = I_L(\frac{E_m}{q})} \tag{2.12}$$

Where $$\boldsymbol{E_m = q[V_{oc} - \frac{1}{\beta} ln(1 + \beta V_m) - \frac{1}{\beta}]} \tag{2.13}$$

This E_m corresponds to the energy per photon delivered to the load at the maximum power point.

2.20 Surface Plasmons

The aim of this section is to give an overview of the physics of plasmons and their applications, so-called plasmonics. The emphasis will be on the concepts rather than the

methods, since the goal is primarily to understand what plasmons are and which type of plasmons can exist under different conditions.

Surface plasmons (SPs), are coherent electron oscillations that exist at the interface between any two materials where the real part of the dielectric function changes sign across the interface (e.g. a metal-dielectric interface). SPs have lower energy than bulk plasmons which quantize the longitudinal electron oscillations about positive ion cores within the bulk of an electron gas (or plasma). When SPs couple with a photon, the resulting hybridized excitation is called surface plasmon polariton (SPP). This SPP can propagate along the surface of a metal until energy is lost either via absorption in the metal or radiation into free-space. There are two important types of plasmons: localized surface plasmon-polaritons (LSPP or LSP) and propagating surface plasmon-polaritons (PSPP).The Drude model is introduced here which is used to model the motion of free electrons in the metal as free particles.

2.21 Maxwell's Equation and Boundary Conditions

Maxwell's equations are a set of partial differential equations that, together with the Lorentz force law, form the foundation of classical electrodynamics, classical optics, and electric circuits. These in turn underlie modern electrical and communications technologies. These first-order differential equations describe the electromagnetic effects based on the spatial parameters and permittivity of the object. The constitutive relations determine the electric and magnetic flux that results from an imposed electromagnetic field and the material's susceptibility to electric and magnetic polarization. Conceptually, Maxwell's equations explain how electric charges and electric currents act as sources for the electric and magnetic fields. Further, it describes how a time varying electric field generates a time varying magnetic field and vice versa. Following the explanation and derivation given by J.D. Jackson in his book, the Maxwell's equations are given as follows:

$$\boldsymbol{\nabla} \times \boldsymbol{E} = -\frac{\boldsymbol{\partial B}}{\boldsymbol{\partial t}} \qquad (2.14)$$

$$\boldsymbol{\nabla} \times \boldsymbol{H} = \boldsymbol{J} + \frac{\boldsymbol{\partial D}}{\boldsymbol{\partial t}} \qquad (2.15)$$

$$\boldsymbol{\nabla}.\boldsymbol{D} = \boldsymbol{\rho} \qquad (2.16)$$

$$\boldsymbol{\nabla}.\boldsymbol{B} = \boldsymbol{0} \qquad (2.17)$$

where E (V/m) is the electric field and H (A/m) is the magnetic field. The electric flux density is given D (C/m^2) while the magnetic flux density is given by B (Tesla). The total charge density (including both free and bound charge) is denoted by ρ (C/m^3) and the total current density is denoted by J (A/m^2).

The relation between field and flux density is given by:

$$\boldsymbol{D} = \boldsymbol{\varepsilon \varepsilon_o E} \qquad (2.18)$$

$$\boldsymbol{B} = \mu\mu_{\boldsymbol{o}}\boldsymbol{H} \qquad (2.19)$$

Where ε and ε_o are the electrical permittivity of the material and of the free space respectively, while μ and μ_o are the magnetic permeability of the material and of the free space respectively.

The current density and the electric field are related by the expression:

$$\boldsymbol{J} = \boldsymbol{\sigma E} \qquad (2.20)$$

where σ is the electrical conductivity.

The wave equation for E and H can be derived as

$$\boldsymbol{\nabla^2 E} = \boldsymbol{\sigma}\mu\mu_{\boldsymbol{0}}\frac{\boldsymbol{\partial E}}{\boldsymbol{\partial t}} + \mu\mu_{\boldsymbol{0}}\boldsymbol{\varepsilon\varepsilon_0}\frac{\boldsymbol{\partial^2 E}}{\boldsymbol{\partial t^2}} \qquad (2.21)$$

$$\boldsymbol{\nabla^2 H} = \boldsymbol{\sigma}\mu\mu_{\boldsymbol{0}}\frac{\boldsymbol{\partial H}}{\boldsymbol{\partial t}} + \mu\mu_{\boldsymbol{0}}\boldsymbol{\varepsilon\varepsilon_0}\frac{\boldsymbol{\partial^2 H}}{\boldsymbol{\partial t^2}} \qquad (2.22)$$

When electric field has a planar wave form then

$$\mathbf{E} = \mathbf{E_0}\mathbf{exp}\ (\mathbf{i}(\mathbf{k}.\mathbf{r} - \mathbf{wt})) \qquad (2.23)$$

Where k is the direction in which the wave propagates and its magnitude equals

$$\mathbf{k^2} = \mathbf{i}\sigma\mu\mu_0\boldsymbol{\omega} + \mu\mu_0\boldsymbol{\varepsilon}\boldsymbol{\varepsilon_0}\boldsymbol{\omega^2} \qquad (2.24)$$

In the case of vacuum, when ε=1, μ=1, σ=0 and k=ω/c then

$$\boldsymbol{c} = \frac{\mathbf{1}}{\sqrt{\mu_0}\boldsymbol{\varepsilon_0}} \qquad (2.25)$$

It is important to note that the material parameters are often a function of frequency;

$$\boldsymbol{\varepsilon} = \boldsymbol{\varepsilon}(\boldsymbol{\omega}) \qquad \mu = \mu(\boldsymbol{\omega}) \qquad \boldsymbol{\sigma} = \boldsymbol{\sigma}(\boldsymbol{\omega})$$

The complex optical index is expressed by $\tilde{\boldsymbol{n}} = \boldsymbol{n} + \boldsymbol{i\kappa}$, where n and k are the real and imaginary parts respectively. While n indicates the phase speed, κ indicates the amount of absorption loss when the electromagnetic wave propagates through the medium. κ is often called the extinction coefficient in physics. In most circumstances $\kappa > 0$ (light is absorbed) or $\kappa = 0$ (light travels forever without loss). In special situations, especially lasers, it is also possible that $\kappa < 0$ (light is amplified).

The dielectric constant is simply the square of the (complex) refractive index in a non-magnetic medium (one with a relative permeability of unity). The refractive index is used for optics in Fresnel equations and Snell's law; while the dielectric constant is used in Maxwell's equations and electronics.

$$\tilde{\boldsymbol{\varepsilon}} = \boldsymbol{\varepsilon_1} + \boldsymbol{i\varepsilon_2} = \tilde{\boldsymbol{n}}^{\mathbf{2}} = (\boldsymbol{n} + \boldsymbol{i\kappa})^{\mathbf{2}} \qquad (2.26)$$

where $\tilde{\epsilon}$, ϵ_1, ϵ_2, *n*, and κ are functions of wavelength.

Conversion between refractive index and dielectric constant is done by:

$$\boldsymbol{\varepsilon_1} = \boldsymbol{n^2} - \boldsymbol{\kappa^2}\ , \qquad \boldsymbol{\varepsilon_2} = \mathbf{2}\boldsymbol{n\kappa} \qquad (2.27)$$

$$\boldsymbol{n} = \sqrt{\frac{\sqrt{\varepsilon_1{}^2 + \varepsilon_2{}^2} + \varepsilon_1}{2}} \qquad (2.28)$$

$$\boldsymbol{\kappa} = \sqrt{\frac{\sqrt{\varepsilon_1{}^2 + \varepsilon_2{}^2} - \varepsilon_1}{2}} \qquad (2.29)$$

The boundary conditions between two mediums 1 and 2 are given by

Normal components:

$$\boldsymbol{n}.[\boldsymbol{D_1} - \boldsymbol{D_2}] = \boldsymbol{\sigma_{12}} \qquad (2.30)$$

$$\boldsymbol{n}.[\boldsymbol{B_1} - \boldsymbol{B_2}] = \boldsymbol{0} \qquad (2.31)$$

Tangential components:

$$\boldsymbol{t}.[\boldsymbol{E_1} - \boldsymbol{E_2}] = \boldsymbol{0} \qquad (2.32)$$

$$\boldsymbol{t}.[\boldsymbol{H_1} - \boldsymbol{H_2}] = \boldsymbol{J_s} \qquad (2.33)$$

After solving the reflection and transmission field intensity at the interface between two mediums, the reflection (r) and transmission (t) coefficient for both the s and p polarized waves are observed.

These are also called the Fresnel's equations. Figure 7 shows the interface between two mediums along with the various variables used. As a consequence of the conservation of energy, the transmission coefficient in each case is given by $\boldsymbol{t_p} = \boldsymbol{1} - \boldsymbol{r_p}$ and $\boldsymbol{t_s} = \boldsymbol{1} - \boldsymbol{r_s}$.

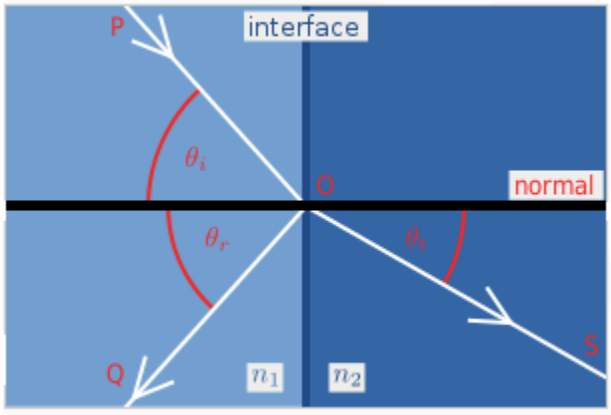

Figure 7. Interface between two medium showing various variables of the Fresnel's equation.

If the incident light is unpolarized (containing an equal mix of *s*- and *p*-polarizations), the reflection coefficient is: $\frac{r_s+r_p}{2}$

Where,

$$\mathbf{r_p} = \frac{-\mathbf{n_1}\cos\boldsymbol{\theta_t}+\mathbf{n_2}\cos\boldsymbol{\theta_i}}{\mathbf{n_1}\cos\boldsymbol{\theta_t}+\mathbf{n_2}\cos\boldsymbol{\theta_i}} \qquad (2.34)$$

$$\mathbf{t_p} = \frac{2\mathbf{n_1}\cos\boldsymbol{\theta_i}}{\mathbf{n_1}\cos\boldsymbol{\theta_t}+\mathbf{n_2}\cos\boldsymbol{\theta_i}} \qquad (2.35)$$

$$\mathbf{r_s} = \frac{\mathbf{n_1}\cos\boldsymbol{\theta_i}-\mathbf{n_2}\cos\boldsymbol{\theta_t}}{\mathbf{n_1}\cos\boldsymbol{\theta_i}+\mathbf{n_2}\cos\boldsymbol{\theta_t}} \qquad (2.36)$$

$$\mathbf{t_s} = \frac{2\mathbf{n_1}\cos\boldsymbol{\theta_i}}{\mathbf{n_1}\cos\boldsymbol{\theta_i}+\mathbf{n_2}\cos\boldsymbol{\theta_t}} \qquad (2.37)$$

The fraction of the power that has been reflected and transmitted depends on the ratio of the squares of the amplitudes, which can be expressed as:

$$\boldsymbol{R = r^2} \qquad (2.38)$$

$$\boldsymbol{T = \frac{n_2 t^2}{n_1}} \qquad (2.39)$$

2.22 Drude Model and Dielectric Constant of Metal

The Drude model was proposed in 1900 by Paul Drude to explain the transport properties of electrons in materials (especially metals).The model is based on treating electrons as damped harmonically bound particles, subjected to external electric fields. It explains the phenomena of normal and anomalous dispersion and their relation to the absorption of radiation.

The dielectric constant is

$$\boldsymbol{\varepsilon_r(\omega) = 1 + \frac{Ne^2}{\varepsilon_o m}\frac{1}{\omega_0{}^2 - \omega^2 - i\gamma\omega}} \qquad (2.40)$$

Where N (m^{-3}) is the number of free electrons per unit volume and m (Kg) is their mass. The damping term, γ (rad s^{-1}), here corresponds to the collision rate of free electrons with the crystal or impurities [6]. The resonant frequency is given by ω_0.

We can define the plasma frequency as the natural oscillation frequency of the free-electron-plasma charge density; $\boldsymbol{\omega_p = \sqrt{\frac{Ne^2}{\varepsilon_0 m}}}$ .The conduction electrons in a metal are not bound and can therefore is described without the restoring force (i.e. $\omega_0 \approx 0$).

The Drude model for metal dispersion then becomes

$$\boldsymbol{\varepsilon_r(\omega) = 1 - \frac{\omega_p{}^2}{\omega^2 + i\gamma\omega}} \qquad (2.41)$$

The damping effect in metals due to electron collision occurs at a rate $\tau = 1/\gamma$. The real and the imaginary part of the dielectric constant can be written as

$$\boldsymbol{Re\big(\varepsilon_r(\omega)\big) = 1 - \frac{\omega_p{}^2\tau^2}{1 + \omega^2\tau^2}} \qquad (2.42)$$

$$\boldsymbol{Im\left(\varepsilon_r(\omega)\right) = \frac{\omega_p{}^2\tau}{\omega(1+\omega^2\tau^2)}} \qquad (2.43)$$

The collision time in metals is typically ~10^{-14} s, thus it can be easily assumed that $\boldsymbol{\omega^2\tau^2 \gg 1.}$

The real and imaginary parts can further be approximated to

$$\boldsymbol{Re\left(\varepsilon_r(\omega)\right) = 1 - \frac{\omega_p{}^2}{\omega^2}} \qquad (2.44)$$

$$\boldsymbol{Im\left(\varepsilon_r(\omega)\right) = \frac{\omega_p{}^2}{\omega^3\tau^2}} \qquad (2.45)$$

We see that in the region where $\omega < \omega_p$(wavelength longer thanλ_p), we have $Re\left(\varepsilon_r(\omega)\right) < 0$. Moreover, if ω is not too small, the absorption, characterized by $Im\left(\varepsilon_r(\omega)\right)$, is also small in this region. It is these two conditions, $Re\left(\varepsilon_r(\omega)\right) < 0$ and small$Im\left(\varepsilon_r(\omega)\right)$, that makes possible a whole range of interesting optical effects, including plasmon resonances. These conditions are never fulfilled in standard dielectrics where *Re (ε)* is typically between 1 and ~10. For many metals, the plasma frequency is in the UV part of the electromagnetic spectrum, and the regions of interest are therefore in the visible (and close UV, or near infrared, depending on the metal) [6].

2.23 Metal Choices for Surface Plasmon

The decay of *Re (ε)* from small values in the UV region to negative values in the visible, and more negative values in the infrared, is common to all metals and is predicted by the Drude model [6]. This is one of the most important characteristics of metals, as far as optical properties are concerned, and it is a consequence of the optical response of the free conduction electrons, as explained by the Drude model. The real and imaginary parts of the dielectric function of various metals are plotted in Figure 8.

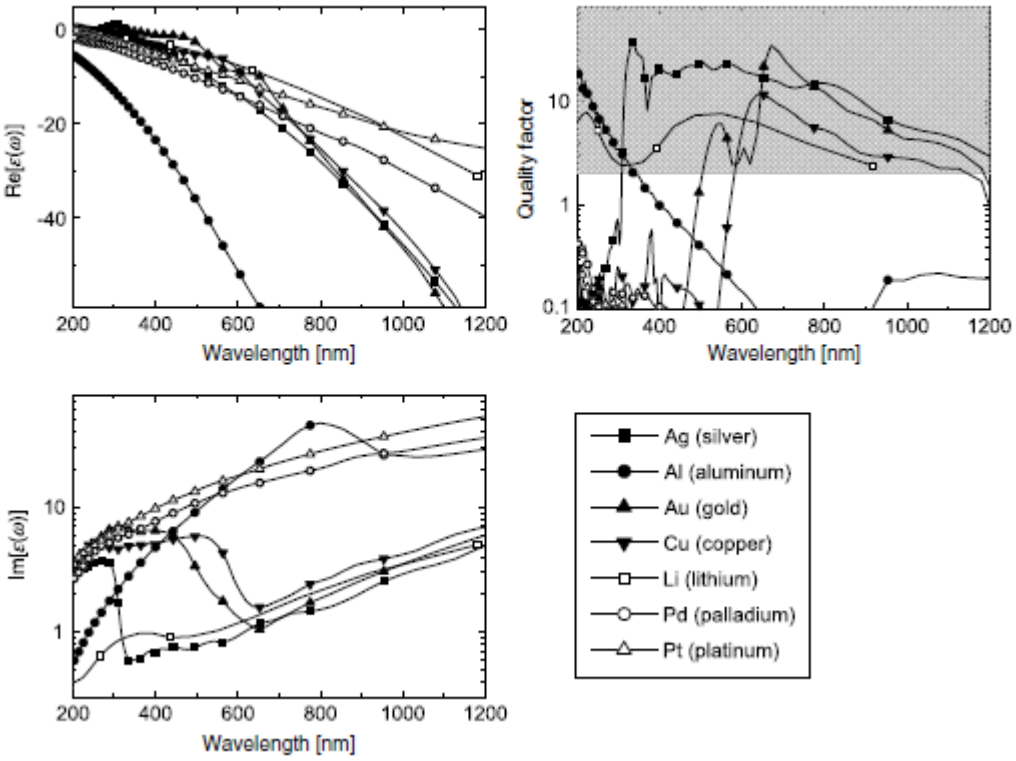

Figure 8. Overview of the optical properties of a selection of metals in the (extended) visible range. The real (top) and imaginary (bottom) parts of ε are plotted against wavelength. Also shown (top-right) is the predicted approximate quality factor Q of localized surface plasmon resonances for a metal/air nanoparticle. The shaded area is the area of interest to many plasmonics applications [6].

The negativity of the *Re (ε)* at visible wavelengths is also the origin of many of the known optical properties of metals, including plasmon-related effects. It implies that the refractive index is smaller than one and even close to zero, while most common materials have a refractive index of ~1 or more. The reflection coefficient at a dielectric/metal interface is derived simply from the relative refractive indices (already shown earlier), and the small refractive index of metals directly leads to a reflection coefficient close to one (almost perfect reflector), which is arguably one of the best known and most visible properties of metals [6]. Figure 8 also shows a plot of the quality factor (Q) plotted against the wavelength. To understand the quality factor, an example of a small metallic sphere interacting with an electromagnetic field can be considered. The (complex) electric field inside the sphere can then be shown to be constant and proportional to the incident field E_0:

$$\boldsymbol{E_{in}} = \frac{3\epsilon_m \boldsymbol{E_0}}{\epsilon(\boldsymbol{\omega})+2\epsilon_m} \qquad \text{Where m: medium} \qquad (2.46)$$

The important part in this expression is the denominator. If it were close to zero (a condition which can be achieved if $\varepsilon(\omega) \cong -2\varepsilon_m$) then the fraction would be very large (infinite for perfect equality). This is not possible for standard dielectrics, for which ε is typically between 1 and ~10. But for metals, this condition can be approximately met if the absorption is small ($\text{Im}(\varepsilon(\omega)) \cong 0$) at a wavelength where $\text{Re}(\varepsilon(\omega)) \cong -2\varepsilon_m$. The optical response (absorption and scattering) at this particular frequency (or wavelength) is then very large, i.e. this is the signature of a resonance [6]. This is explicitly illustrated in Figure 9 where the absorption coefficient (proportional to $|E_{in}|^2$) is shown as a function of wavelength for a small silver sphere in air ($\varepsilon_m = 1$).

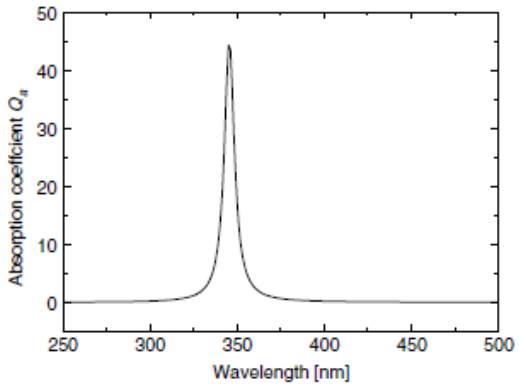

Figure 9. Absorption coefficient (Q_abs) as a function of wavelength for a silver sphere of 25nm radius [6].

There is a clear resonant response at ~345 nm, which corresponds to the condition $\text{Re}(\varepsilon(\omega)) \cong -2$. It is interesting to note at this stage that while the resonance condition is determined primarily by the real part of ε (ω), it is actually its imaginary part that limits how large the resonance can be [6].

Both types of plasmons (LSP and PSPP) are strongly affected by optical absorption, i.e. the larger the Im (ε), the more lossy they are. For LSP resonances, this damping can further be characterized by a quality factor defined as

$$\boldsymbol{Q = \omega \frac{(d\varepsilon')/d\omega}{2(\varepsilon''(\omega))^2}} \qquad (2.47)$$

Where $\in' = Re(\varepsilon)$ and $\in'' = Im(\varepsilon)$. In plain terms, Q is large when Im (ε) is small and, therefore, characterizes the strength (and width) of the resonance.

From the above discussion, one can consider that a metal is a good choice for plasmonics if

- Re (ω) is negative in the wavelength range of interest (typically, visible and near IR). For LSP applications, one in fact needs $-20 \leq Re(\omega) \leq -1$.
- Im (ω) is small (or Q is large) in the range of interest. Typically, Q must be larger than ~2, preferably larger than ~10 [6].

From the quality factor plot in the Figure 8, it can be seen that viable choices for plasmonics (shaded region in Figure 8) are silver, gold, lithium and copper. These have higher values of Q. Lithium is highly unstable and its use is not practical. It reacts easily and does not occur freely in nature due to its chemical activity. Copper can be a good choice at longer wavelengths (typically more than ~600nm) though its Q is not as high compared to gold or silver. Silver has the least absorption among all, it's inter band transition frequency does not lie in the visible regime and thus can be widely used in plasmon applications. However it suffers from oxidation effects and having an oxide layer on top of the metal surface might alter its optical properties. Gold, being a noble element does not face this crisis and its availability, ease of manipulation, especially for the fabrication of nanostructures, toxicity, durability, cost, etc, it is certainly the most promising in these categories, and should therefore be the material of choice.

2.30 Plasmonic Enhancement of Solar Cells

This section combines the two earlier sections and talks about various factors that are involved in the plasmonic enhancement of solar cells. Two main mechanisms proposed to explain the photocurrent enhancement by metal nanoparticles incorporated on top of solar cells: light scattering and near-field concentration of light are explained.
The effect of shape, size and distribution of the metal nanoparticles on the enhancement is also discussed in this section.

2.31 Light Scattering by Metal Nanoparticles

Metal nanoparticles are strong scatterers of light at wavelengths near plasmon resonance, which is due to the collective oscillation of the conduction electrons in the metal. For particles with diameters well below the wavelength of light, the scattering and absorption cross-section are given below (also mentioned earlier):

$$C_{scat} = \frac{1}{6\pi}\left(\frac{2\pi}{\lambda}\right)^4 |\alpha|^2 \qquad (2.48)$$

$$C_{abs} = \frac{2\pi}{\lambda} Im|\alpha| \qquad (2.49)$$

Where $\alpha = 3V\left[\frac{\varepsilon_p/\varepsilon_m - 1}{\varepsilon_p/\varepsilon_m + 2}\right]$ is the polarizability and V is the volume of the particle [7]. We can see from the above equations that the particle polarizability becomes very large when $\varepsilon_p = -2\varepsilon_m$.When that happens, phenomenon known as surface plasmon resonance occurs. At the surface plasmon resonance, the scattering cross-sectional area can well exceed the geometrical cross-sectional area of the particle. For the case of small silver nanoparticles in air, at resonance the scattering cross-section is about 10 times the geometric cross-section of the silver nanoparticles. Typically, for a 100nm Ag particle, the albedo (scattering cross-

section over sum of scattering and absorption cross-section) is more than 0.9. For large particle sizes, dynamic depolarization and radiation damping become important corrections to the quasi-static expressions mentioned above. Furthermore, for larger particle sizes, the excitation higher-order plasmon modes must be taken into consideration [7].

Dynamic depolarization occurs because as the particle size increases, conduction electrons across the particle no longer move in phase. This leads to a reduction in the depolarization field (which is generated by the surrounding polarized matter) at the centre of the particle. Consequently, there is a reduced restoring force and thus a red-shift in the particle resonance. For particle sizes where scattering is significant, this re-radiation leads to a radiative damping correction to the quasi-static polarizability, the effect of which is to significantly broaden the plasmon resonance. The red-shift and broadening of the resonance with increased particle size would be expected to be an advantage for solar cell applications, since light-trapping should occur over a relatively broad wavelength range. While an increased size leads to a larger absolute scattering cross section, these effects do lead to a reduced cross section when normalized by size. Inclusion of dynamic depolarization and radiative damping effects can give reasonably accurate predictions of many features of the extinction spectra for larger particles for cases where the contribution of higher order multipoles can be neglected [7].

For excitation at wavelengths below the resonance, the scattered radiation is out of phase with the incident radiation with the phase difference depending on the frequency, and as a result the scattered light interferes destructively with the direct incident light. This leads to reduced coupling of light into the semiconductor and consequently a reduced photocurrent for wavelengths below the resonance wavelength. Thus the maximum in-coupling and maximum photo-current occurs slightly above the surface plasmon resonance wavelength, where the scattering cross-section is high but the scattered field is still approximately in phase with the incident field [7].

2.32 Local Field Enhancement

For particles with a diameter d<<λ (wavelength of incident light), the conduction electrons inside the particle move all in phase upon excitation, leading to the buildup of polarization charges on the particle surface. These charges act as an effective restoring force, allowing resonance to occur at a specific frequency (particle dipole plasmon frequency. Thus, a resonantly enhanced field builds up inside the particle, which in the small particle limit is homogeneous throughout its volume, producing a dipolar field outside the particle. This leads to a strongly enhanced near field in the immediate vicinity of the particle surface [8]. It is this resonantly enhanced near field, which gives rise to many of the promising applications of metal nanoparticles.

Generally, numerical methods such as the T-matrix method, the discrete dipole approximation or finite difference time domain simulations (FDTD) have to be used in recent past to calculate the resonance frequencies and mode profiles of more complex shapes. Such simulations have especially been employed to determine the local-field enhancement at the particle surface [8].
The direct examination of single particles has been established using both dark-field and near-field optical microscopies. The former method allows for a remarkable visualization of the spectral properties of single particles, as can be seen by the example in Figure 10. The measured spectra (black curves) show good agreement with the predictions from a simple analytical extension of quasi-static Mie theory (open circles) [8].

In arrays of nanoparticles, each nanoparticle with a diameter much smaller than the wavelength of the exciting light acts as an electric dipole. The spacing between nanoparticles determines the type of electromagnetic interaction.

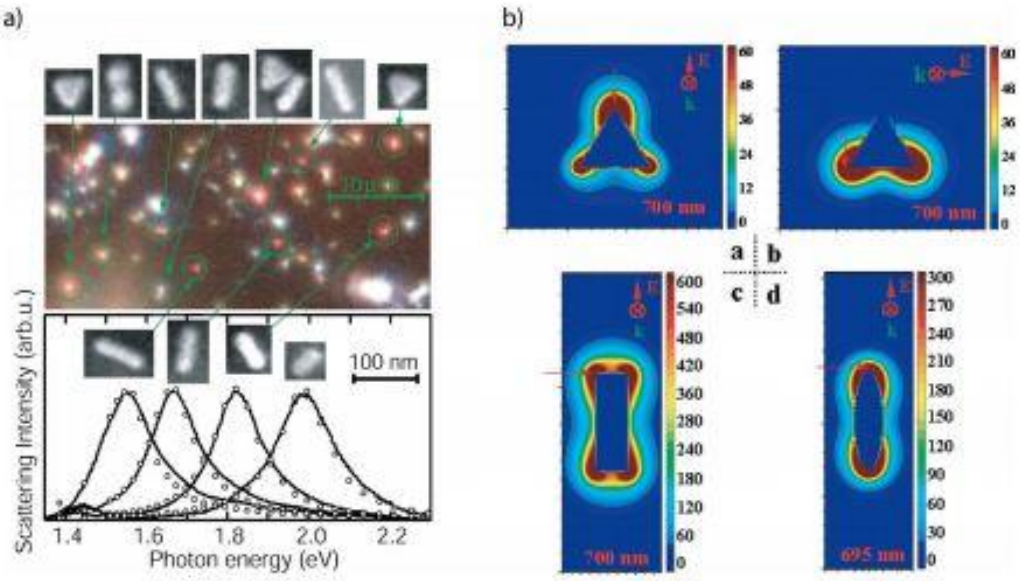

Figure 10. a) Dark field microscopy image (top) and light scattering spectra (bottom) of Au nanocrystals of different shapes. b) Electric near-field profile of the lowest order modes of Ag nanoprisms calculated using discrete dipole approximation formalism [8].

For particle spacing of the order of the exciting wavelength λ, the far-field dipolar interactions with a distance dependence of d^{-1}dominate.

For particle spacings much smaller than the wavelength of light, near-field dipolar interactions between adjacent particles with a distance dependence of d^{-3} dominate [8]. The near-field interactions between such particles have been directly visualized using near field optical microscopy, confirming a strongly enhanced field between the particles (Figure 11), and indicative of near-field coupling.

Localized plasmon excitations caused by particle interactions also occur in randomly nanostructured metallic surfaces. In this case, multiple-scattering processes can lead to hot spots of extremely large field enhancement (on the order of 1000), which has enabled the use of such structures for single-molecule spectroscopy [8].

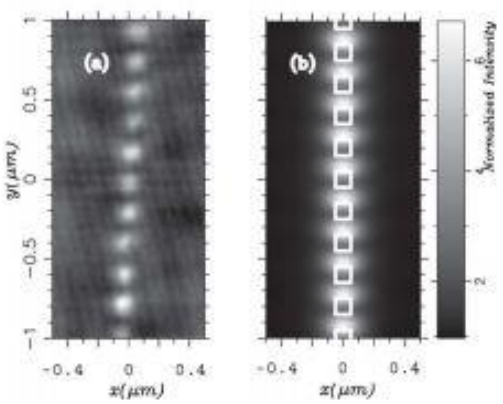

Figure 11. Optical near field around a chain of nanoparticle obtained using collection mode near field optical microscopy [8].

2.33 Factors Effecting Plasmonic Enhancement

The field of plasmonics is vast and complex. There needs to be a systematic study to understand fully all the processes that are involved in this area. Even though a lot of research still needs to be undertaken in this field, recent and past studies have shown that plasmons are affected by a few well known factors which influence their properties and basic functioning.

a) Shape and Size of Metal Nanoparticles

It is well evident that both shape and size of metal nanoparticles are key factors determining the in-coupling efficiency of the plasmon system. It refers to the amount of light that can be coupled into the semiconductor substrate due to scattering by the metal nanoparticles. This is illustrated in Figure 12a, which shows that smaller particles having their effective dipole moment located closer to the semiconductor layer, couple a larger fraction of the incident light into the underlying semiconductor because of enhanced near-field coupling [9].

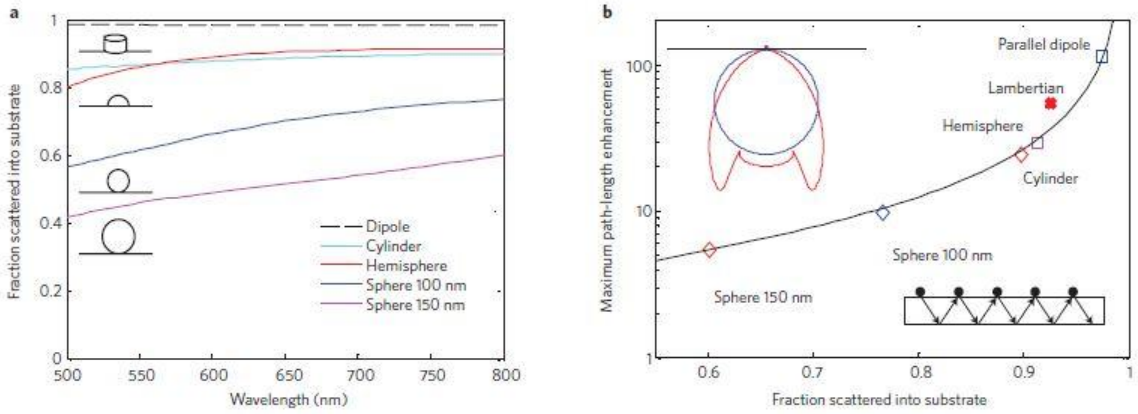

Figure 12. Light scattering and trapping is very sensitive to particle shape. a) Fraction of light scattered into the substrate, divided by total scattered power, for different sizes and shapes of Ag particles on Si. Also plotted is the scattered fraction for a parallel electric dipole that is 10 nm from a Si substrate. b) Maximum path-length enhancement, according to a first-order geometrical model, for the same geometries as in a) at a wavelength of 800 nm. Absorption within the particles is neglected for these calculations, and an ideal rear reflector is assumed. The line is a guide for the eye. Insets: (top left) angular distribution of scattered power for a parallel electric dipole that is 10 nm above a Si surface (red) and a Lambertian scatterer (blue); (lower right) geometry considered for calculating the path-length enhancement [9].

From the above figure, it can be seen that for a point dipole very near to a silicon substrate, 96% of the incident light is scattered into the substrate, demonstrating the power of the particle scattering technique. Figure 12b shows the path-length enhancement in the solar cell derived from Figure 12a using a simple first-order scattering model. For 100-nm-diameter Ag hemispheres on Si, a 30-fold enhancement is found. These light-trapping effects are most pronounced at the peak of the plasmon resonance spectrum, which can be tuned by engineering the dielectric constant of the surrounding matrix [9]. It can be clearly seen that when shape is considered, hemisphere and cylinder show better performance compared to spheres. However fabricating these complex structures is a difficult task and requires more time and is economically challenging. On the other hand, metal nanospheres can be easily incorporated on the solar cell structure and is widely used in plasmonics.

Figure 12 demonstrates the advantage of using small particles to create the forward scattering anisotropy. But smaller particles suffer from significant ohmic losses, which scale with volume v, whereas scattering scales with v^2, thus using larger particles is more gainful to increase the scattering rate. Interestingly, the effective scattering cross-section can be

increased by spacing the particles further away from the substrate, as this prevents destructive interference between the incident and reflected fields from occurring, although at the price of reduced near-field coupling. For frequencies above the plasmon resonance, fano resonance effects can cause destructive interference between scattered and unscattered light beams, and thus can cause reflection rather than enhanced incoupling [9].

b) Arrangement of Metal Nanoparticles

The arrangement of the nanoparticles on top of the solar cell goes a long way in influencing the amount of light scattered into the semiconductor waveguide. Optical scattering by nanoparticles atop a semiconductor photodetector device structure can lead to coupling of photons incident normal to the device surface into lateral optical propagation paths within appropriately designed semiconductor thin-film device structures, due to the introduction of a lateral wave vector component in the scattered wave [10]. SOI photodetector structures were used to investigate the influence of nanoparticle periodicity on coupling of normally incident light into the SOI waveguide in one study

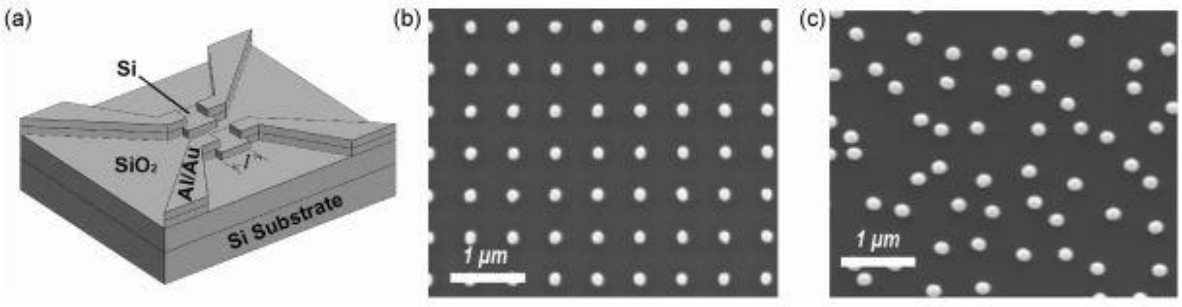

Figure 13. (a) Schematic diagram of SOI photodetector device structure. Also shown are SEM images of (b) periodic and (c) random arrays of Au nanodots patterned on the surface of the active device region [10].

Figure 13a shows a schematic diagram of the basic device structure employed, and Figure 13(b) and (c) show the SEM images of Au nanodots, produced by electron-beam lithographic

patterning and a liftoff process, arranged in a periodic and a random array atop the active region of the silicon-on-insulator photodetector.

For the random array, enhancements in photocurrent response by a factor of up to ~2.5 was observed in a broad enhancement peak centered at a wavelength of ~1000nm, consistent with the relatively low nanodot density of ~2.8×10^{8} cm^{-2} in these structures. For the periodic array, much sharper peaks in photocurrent enhancement, with increases in photocurrent response by factors as large as 5-6, were observed at wavelengths corresponding to confined waveguide modes of the SOI structure and constructive interference of electromagnetic wave components scattered by adjacent or nearby nanodots [10]. These results indicate that definite enhancements in photocurrent response at specific wavelengths can be engineered by appropriate design of metal nanodot arrays combined with thin-film semiconductor structures with corresponding waveguiding behavior.

c) Effect of the Dielectric Spacer

The coupling of the localized surface plasmons to an underlying substrate is very sensitive to the spacing between the particles and the underlying substrate. The spacer layer plays a vital role in plasmonics. For instance, the surface of a crystalline Si solar cell has large disturbances in the crystal lattice due to non-saturated or dangling bonds, allowing energy states in the forbidden band gap. This can result in a recombination process via defect levels or surface states resulting in loss of light generated current and reduction in cell efficiency. Thus for high efficiency crystalline Si solar cell especially, it is crucial that a thin dielectric layer be deposited on the Si to reduce the surface recombination and improve the electrical properties of the device []. The addition of this spacer layer is not just limited to crystalline Si solar cells, but to other semiconductor based solar cells as well, the motivation being: provide a good surface passivation and electrical isolation.

The plasmonic scattering is not only sensitive to the type of the dielectric environment but also its thickness. Both of these would be discussed in this section.

i) Type of dielectric layer

Through the works of Beck et.al, we can understand this section very easily. In their work, the nanoparticles were formed directly on top of three different dielectrics commonly used in solar cell fabrication: silicon dioxide (SiO_2), silicon nitride (Si_3N_4), and titanium dioxide (TiO_2), with refractive indices of 1.5, 2 and 2.5 respectively [11].

The Si wafer samples used for optical characterization had 15 nm of SiO_2 layer for consistency. On top of the oxide layer, the Si samples received further one of the following dielectric layer depositions: 14 nm of thermally grown SiO_2, 17 nm of Si_3N_4 grown by low-pressure chemical vapor deposition (LPCVD), or 15 nm of TiO_2 grown by atmospheric-pressure chemical vapor deposition (APCVD).Three types of bifacial solar cells were made, with oxide layers of 40 nm (sample A), 26 nm (sample B), and 26 nm (sample C). They were all coated with 20 nm of LPCVD Si_3N_4. The Si_3N_4 layer was then etched back to a final thickness of 3 nm (sample B) and 8 nm (sample C) and completely removed for sample A (residual thickness <2 nm).Sample C also received 15 nm of TiO2 by APCVD. All samples and cells were annealed at 400 ° C for 30 min in forming gas before nanoparticle deposition [11].

Figure 14 shows measured optical absorption spectra derived from a combination of reflection and transmission measurements of 200 μm thick Si wafers with nanoparticles on the front and the rear of the samples. A reference measurement taken on a Si wafer with 15 nm of SiO2 thermally grown on the surface is included for comparison.

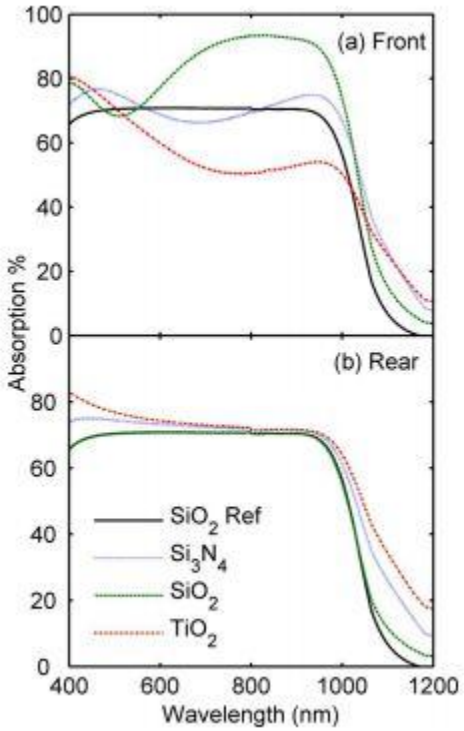

Figure 14. Measured absorption spectra derived from transmission and reflectance measurement. Ag nanoparticles films on layers of SiO2, Si3N4 and TiO2 are plotted with illumination from the front (a) and from the rear (b). A reference measurement for a Si wafer with a SiO_2 layer and no nanoparticles is also shown in each graph [11].

For light incident from the front of the samples (Figure 14a), a large enhancement in absorption, by as much as 23%, is observed for the SiO_2 sample for wavelengths above 600 nm. For the Si_3N_4 layer an enhancement is seen only for wavelengths above 800 nm; no enhancement is observed for the TiO_2 below 1000 nm. In all three geometries, an increase in absorption is observed at wavelengths below 500 nm.

A local minimum in the absorption spectra is observed at 515 nm for SiO_2, 677 nm for Si_3N_4, and 775 nm for TiO_2 [11]. This position of the local minima shows the reduction in absorption around the respective plasmon resonances of the 3 materials, which is attributed to interference between light that is transmitted at the Si interface and light that is scattered by the nanoparticles. For light incident on the rear of the sample, a clear absorption enhancement is observed for all three dielectrics above 1000 nm, while the major absorption

dips around λ_{SPR} seen in Figure 14a are not observed. The latter is due to the fact that the Si wafer is strongly absorbing up to wavelengths of 900 nm, so the nanoparticles are not expected to affect absorption in this spectral region with light incident from the rear [11]. The slight increases in the absorption at short wavelengths are due to the different dielectric coatings on each wafer acting as short wavelength anti-reflection coatings. Figure 15 shows EQE spectra measured for bifacial Si solar cells with and without Ag nanoparticles and with different dielectric layer configurations.

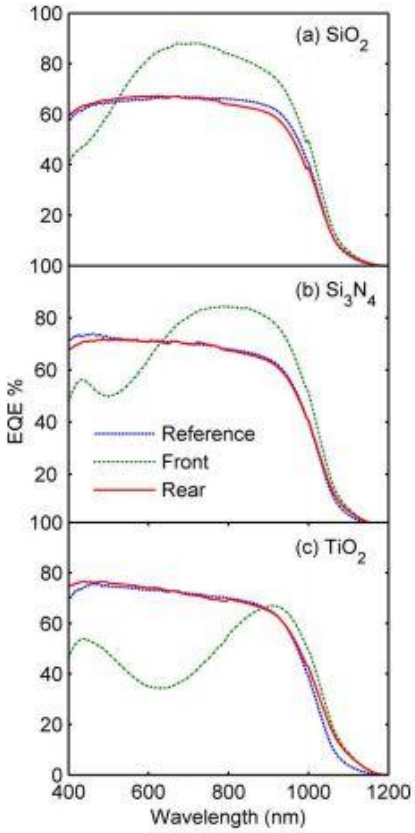

Figure 15. Measured EQE of 100 µm thick, crystalline bifacial solar cells, with nanoparticle arrays on the front and rear. Cells had a dielectric layer structure of SiO2 and Si3N4 (etched off for sample A) with a top layer of (a) SiO2 on sample A, (b) Si3N4 on sample B and (c) TiO_2 on sample C. Included is a reference measurement (dashed lines) without particles for each of the different dielectric configurations [11].

The reference measurements for the three different dielectric layer configurations show an increase in EQE for the higher index dielectrics as they act as anti-reflection coatings. A clear

enhancement in EQE is observed for light incident from the front for sample A, with an over layer of SiO_2, and sample B with Si_3N_4 on top. Interference effects around λ_{SPR} can be clearly seen. Small variations in the position of the local minima between figures 14 and 15 are ascribed to the differences in dielectric layer structure and Ag nanoparticle films produced by dissimilar surface conditions [11].

ii) Thickness of the dielectric layer

The work of Pillai et. al. has been referred in this section to explain the effect of varying dielectric thicknesses on the plasmon physics.
In this work, Polycrystalline Si thin film solar cells deposited on glass and Si thin film samples on glass (which had not been processed into solar cells) were used for the investigation. A thin non-stoichiometric layer of SiO_2 of varying thickness was sputtered on some of the samples. Thicknesses of 30 nm were deposited for finished cells and 5, 20, and 30 nm was deposited for the plain thin film samples. Metal nanoparticles were then deposited by thermally evaporating a 16 nm mass thickness of Ag and annealing it in flowing nitrogen for an hour at200^{o}C on the finished solar cells (for electrical measurements) as well as the thin film samples (for optical measurements) [12].

Figure 16(a) and 16(c) shows the EQE spectra for thin Si solar cells with Ag nanoparticle deposited directly on the front and rear surface respectively, and when separated from the Si active layer by a 30 nm oxide spacer layer.
Figure 16(b) and 16(d) show optical absorption of the Si films on glass with varying oxide thicknesses for particles on the front and rear respectively.

It can be clearly seen that the particles on the front on the oxide performed better than particles directly on Si over the measured spectrum. The particles with an oxide increased the EQE from a wavelength of 600 to 1200 nm, while particles without the spacer layer were

useful above 700 nm. Beyond wavelengths of 900 nm the enhancement was similar for both cases. The reduction in the cell response below 500 nm for the oxide case, and 650 nm for the no oxide case, can be due to the suppression of the photocurrent response at wavelengths below resonance as a result of interference [12].

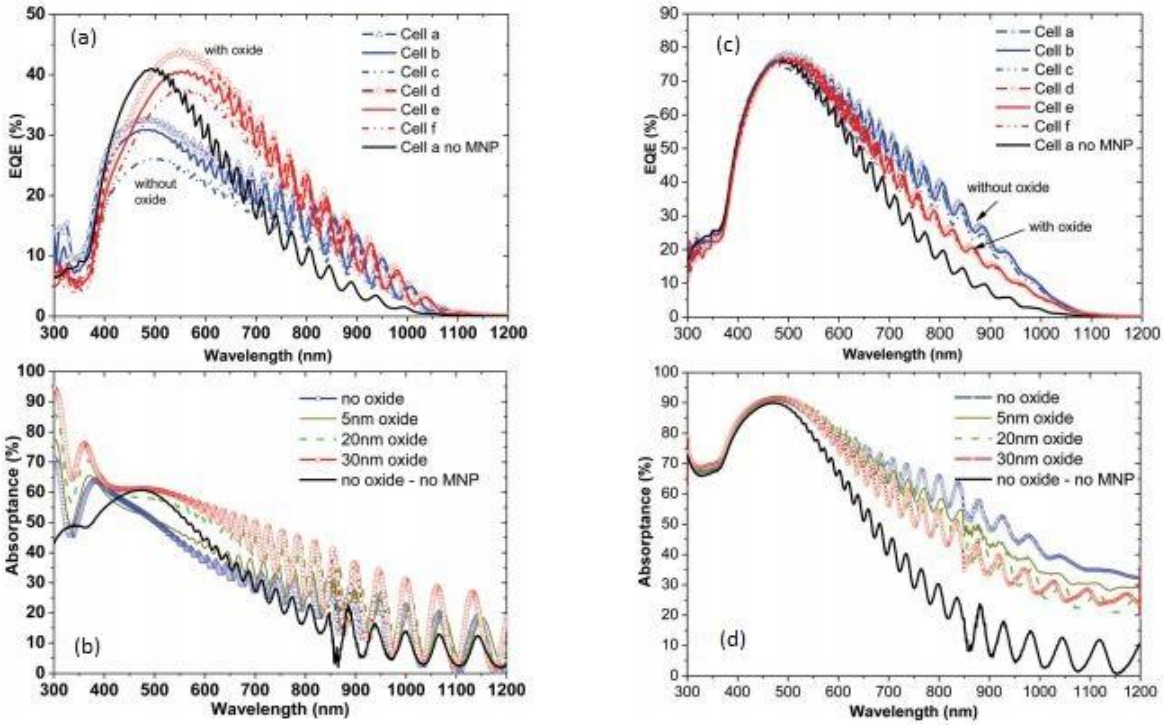

Figure 16. (a), (c) The external quantum efficiency of 2 µm thick poly-Si cells deposited on glass for front and rear side illumination respectively. The blue plots (cells a, b, and c) are with no oxide layer, and the red plots (cells d, e, and f) are with 30 nm oxide (b),(d) the corresponding optical absorptance from a similar sample with 0, 5, 20, and 30 nm of oxide for front and rear particles respectively. The solid black line in the two figures shows the base measurements without dielectric and without any metal nanoparticles (MNP) [12].

The absorptance measurements in Figure 16(b) are in good agreement with the above EQE results in the wavelength region beyond 450 nm as the optical results below this wavelength can involve absorption in the Ag which cannot be isolated from absorption in the Si. The results showed that particles on a relatively thick spacer layer of 20 to 30 nm provide greater

absorption enhancement over a larger wavelength region, compared to particles directly on the Si and on 5nm thick spacer layers [12].

From the figures 16(c) and 16(d), it can be seen that all samples with particles on the rear, both on Si and on oxide layers, performed better than the case without any nanoparticles beyond 500 nm. This is can be attributed to the fact that transmission losses begin to occur for a 2 μm thick Si cell above this wavelength, and hence the light trapping provided by the scattering layer results in an increase in photocurrent and absorptance [12]. Unlike in figures 16(a) and 16(b), where particles are on the front of the cells, any photocurrent suppression at short wavelengths is not observed. This is since the cell is thick enough to absorb the incoming light at wavelengths below 500 nm before it reaches the particles. The maximum EQE enhancement occurs for particles deposited directly on the Si surface [12].

2.40 Summary

This section has attempted to explain some basic fundamentals relating to solar cell and its operation. The physics behind the plasmonics and its application to solar cells has also been discussed. Enhancement in near electric field and scattering are the two main reasons for the improved efficiencies.

The various factors affecting the plasmon resonance are: a) size and shape of nanoparticle, b) arrangement of the nanoparticles and c) dielectric environment.

The structure and the process variations can be engineered to tune the plasmon resonances of these metal nanoparticles according to the need and requirement.

2.50 References

[1] Christiana Honsberg and Stuart Bowden, 'Welcome to PVCDROM' [online], http://pveducation.org/pvcdrom.

[2] Stephen J. Fonash, Device Physics of Solar Cells, 2nd Edition, USA: Elsevier, 2010.

[3] Gueymard,C.; Myers, D.;Emery, K. Proposed reference irradiance spectra for solar energy systems testing, Solar Energy, Volume 73, Issue 6, December 2002, Pages 443-467.

[4] Gueymard, C. The sun's total and spectral irradiance for solar energy applications and solar radiation models, Solar Energy, Volume 76, Issue 4, April 2004, Pages 423-453.

[5] S.M. Sze, Physics of Semiconductor Devices, 2nd Edition, USA: John Wiley & Sons, Inc., 1981.

[6] Eric C. Le Ru, Pablo G. Etchegoin, Principles of surface- enhanced Raman spectroscopy and related plasmon effects, First edition, Amsterdam: Elsevier, 2009.

[7] K. R. Catchpole and A. Polman, "Plasmonic solar cells," Optics Express, vol. 16, pp. 21793-21800, Dec 2008.

[8] Maier, Stefan A., "Plasmonics: Localization and guiding of electromagnetic energy in metal/dielectric structures". Journal of applied physics (0021-8979), 98 (1), p. 011101, 2005.

[9] H. A. Atwater and A. Polman, "Plasmonics for improved photovoltaic devices," Nature Materials, vol. 9, pp. 205-213, Mar 2010.

[10] Lim, S. H. "Light scattering into silicon-on-insulator waveguide modes by random and periodic gold nanodot arrays". Journal of applied physics (0021-8979), 105 (7), p. 073101, 2009.

[11] F. J. Beck, et al., "Tunable light trapping for solar cells using localized surface plasmons," Journal of Applied Physics, vol. 105, Jun 2009.

[12] Pillai, S. "The effect of dielectric spacer thickness on surface plasmon enhanced solar cells for front and rear side depositions". Journal of applied physics (0021-8979), 109 (7), p. 073105, 2011.

[13] Harriet Kung, 'Basic Research for Energy', Office of Science, US Department of Energy, July 2010.

CHAPTER 3

LITERATURE REVIEW

3.10 Review

The optical properties of metal particles have been studied since the time of Faraday. In recent decades, the interest in plasmons has spiked up due to the discovery that Raman scattering can be increased by orders of magnitude through the use of metal nanostructures. Subsequently, there has been great deal of work in fundamental properties and applications of plasmonic resonances, especially in integrated optics and biosensing [1].

Stuart and Hall presented exceptional work in the area of plasmonic enhanced of light sensitive devices and showed that an enhancement in photocurrent of nearly factor of 20 could be achieved for a silicon-on-insulator photo-detector at a wavelength of 800nm [2].The island films of the metals (gold, silver, copper) were formed by thermal deposition under high vacuum followed by an annealing step. The island films were formed on a 30nm Lithium Fluoride (LiF) spacer layer [2]. Stuart and Hall showed that silver (Ag) offered a distinct advantage over both gold (Au) and copper (Cu) since it is the least lossy out of the three materials. Figure 17 shows plots of scattering efficiency (Q_{rad}) for the three materials. Q_{rad} is given by the following equation:

$$\boldsymbol{Q_{rad=}C_{sca}/(C_{sca}+C_{abs})}, \tag{3.1}$$

C_{abs} and C_{sca} are the absorption and scattering cross-sections respectively given by

$$\boldsymbol{C_{abs}} = \frac{\boldsymbol{2\pi}}{\boldsymbol{\lambda}}\,\mathbf{Im[\alpha]}, \qquad \boldsymbol{C_{sca}} = \frac{\mathbf{1}}{\boldsymbol{6\pi}}\left(\frac{\mathbf{2\pi}}{\boldsymbol{\lambda}}\right)^{\mathbf{4}}|\boldsymbol{\alpha}|^{\mathbf{2}} \tag{3.2}$$

Where α is the polarizability of the particle.

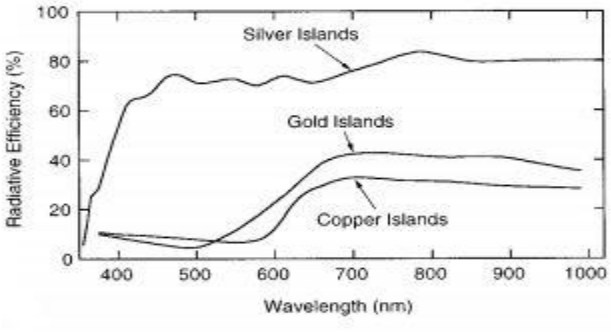

Figure 17. Scattering efficiency for spherical islands (Ag, Au, and Cu) for a 50nm particle diameter [2].

Q_{rad} increases as particle size increases; this is due to the fact that because large particles have higher polarizabilities, causing higher radiative rates. The particle size cannot be increased indefinitely and must be smaller than the optical wavelength. For particles exceeding this size constraint, the strong dipole resonance mode will not be efficiently excited and weaker multipole resonances will dominate the particle response [2].

The photocurrent enhancement (G) produced in the detectors by each of the metal films were measured, where G is defined as the ratio of the photocurrent with and without the Ag-island layer. These results for layers of Ag with three different particle sizes are shown in Figure 18.

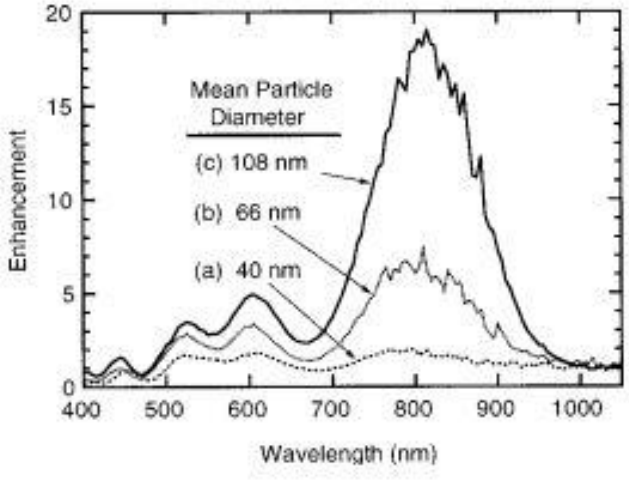

Figure 18. The photocurrent enhancement spectrum for three Ag island layers [2].

Significant differences in the detector response were observed as the island size was increased resulting in an increase in the photocurrent as well. Film (c) with the largest nanoparticles produced an18 fold enhancement in the photocurrent at 800 nm. Enhancements at shorter wavelengths were also measure and were found out to be 5 and 3 corresponding to the wavelengths of 600 nm and 525 nm respectively [2].

Subsequently Schaadt et al. engineered enhancement of optical absorption and photocurrent in a semiconductor via the excitation of surface plasmon resonances in spherical gold (Au) nanoparticles deposited on its surface. The Au nanoparticles were deposited by placing a drop of Au colloidal solution containing Au particles of uniform size onto the surface of the fabricated silicon pn junctions after it had been treated with poly-L-lysine solution. This was done to facilitate the immobilization of the Au particles on the device surface [3]. The basic device structure is shown in Figure19.The ohmic contact on the p-type and n-type surface was formed by thermal evaporation of aluminum (Al). Gold nanoparticles with diameters of 50, 80 and 100nm were deposited on the surface of the silicon pn junction diodes.

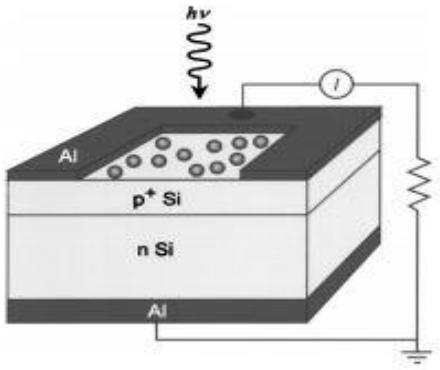

Figure 19. Schematic diagram of Si pn junction diode device structure with metallic nanoparticles [3].

As a result of an enhanced optical absorption in the pn junction diode due to the presence of the metal nanoparticles, an increase in photocurrent response was observed at wavelengths

corresponding to those of the nanoparticle surface plasmon resonances. Figure20 (a) shows the photocurrent response as a function of wavelength for a reference Si pn junction diode

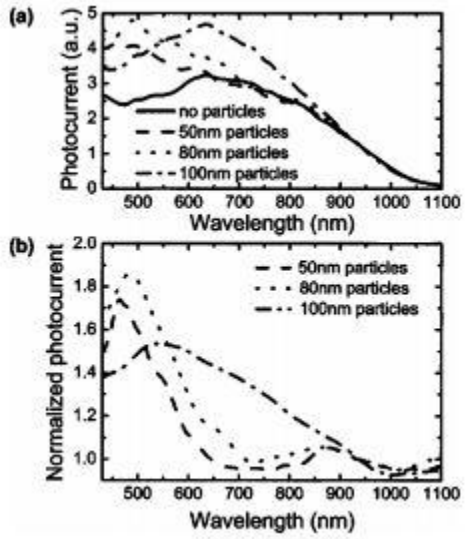

Figure 20. (a) Photocurrent response as a function of wavelength in the absence and presence of Au nanoparticles. (b) Photocurrent response spectra from part (a), normalized to the photocurrent response measured in the absence of nanoparticles, revealing the increased response arising from the presence of the nanoparticles [3].

with no Au nanoparticles present, and for diodes on which Au nanoparticles of 50, 80 and 100nm diameter were deposited. An enhanced photocurrent response was observed at wavelengths of around 900nm and shorter for devices upon which Au nanoparticles were deposited. The degree and wavelength range of this enhancement are dependent on the Au nanoparticle size [3]. Figure 20(b) shows the photocurrent response spectra for diodes upon which Au nanoparticles have been deposited normalized to the measured photocurrent response of the diode itself. The shift to slightly shorter wavelengths in the diode response is a result of the change in local dielectric environment. Near the plasmon resonance wavelengths, an increase in the photocurrent response of 50%-80% relative to that of the reference silicon pn junction diode was observed. Considerably larger increases would be possible at greater nanoparticle densities [3].

Derkacs et al. engineered an enhancement in short circuit current density and energy conversion efficiency in amorphous silicon p-i-n solar cells by achieving an improved transmission of electromagnetic radiation arising from forward scatting by the surface plasmon polaritons modes in Au nanoparticles deposited above the amorphous silicon film[4]. An overall increase of 8% in conversion efficiency was demonstrated by his group. Like Schaadt et al., they used Au colloidal particles (100nm diameter) after the surface was subjected to poly-l-lysine solution. However this was done after a thin layer of indium tin oxide (ITO) was sputtered over the p-type surface. The basic device structure used is shown in Figure 21.

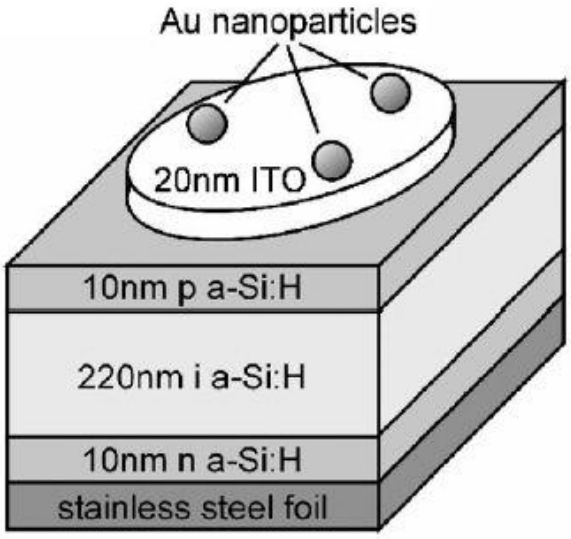

Figure 21. Schematic diagram of a-Si:H p-i-n solar cell structure with Au nanoparticles [4].

Hydrogenated amorphous silicon (a-Si: H) solar cells were employed for this research as it is a thin-film, low-cost alternative to bulk crystalline Si cells and it also offers a much larger absorption coefficient across the solar radiation spectrum. The J-V characteristics, and the corresponding power output, for the reference device structure without Au nanoparticles and for the same structure following the Au nanoparticle deposition were carried out and is shown by Figure 22.

An 8.1% increase in short-circuit current density, from 6.66 to 7.20 mA/cm^2, an 8.3% increase in power output, from 2.77 to 3.0 mW/cm^2, were observed [4].

As explained previously, for smaller particles (diameter below ~10 nm), only a single dipolar mode is supported and as the particle size increases, dipolar, quadrupolar, and other higher-order modes may be supported. For smaller particles supporting only dipolar modes, the total extinction cross section consists of a large absorption cross section and a smaller scattering cross section. For larger particles (diameters of ~100nm or larger), the exact opposite is true: the scattering cross section is much larger than the absorption cross section.

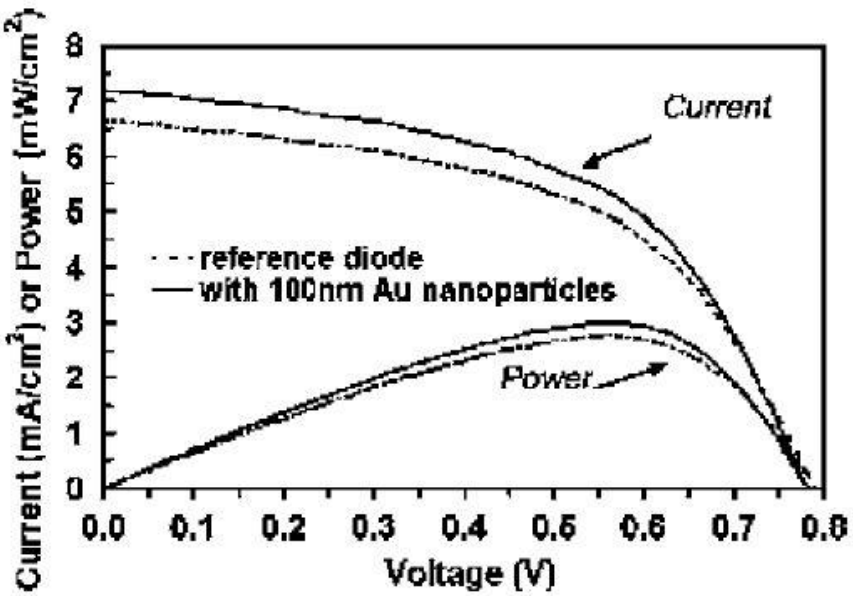

Figure 22. J-V and power output curves measured for reference diodes without Au nanoparticles (dashed lines), and for the same diodes after deposition of 100-nm diameter Au nanoparticles (solid lines) [4].

Note that this is in direct agreement with the Equation 2 provided earlier in this section. In addition, scattering from large particles at and above the Au nanoparticle resonant wavelength (~500nm) is predominantly in the forward direction [4]. The increased short circuit density and power output observed by Derkacs et al. is largely due to this enhanced forward scattering which enables more light to be collected and be absorbed.

Pillai et al. reported an overall photocurrent enhancement of 33% and 19% for 1.25µm thick silicon-on-insulator (SOI) solar cells and planar wafer based cells respectively by using Ag nanoparticles [1]. Silver nanoparticles were deposited by thermal evaporation of thin layer layers of Ag followed by annealing. The advantage of Ag over other metals is that it is less lossy: low absorption loss compared to other metals. The structures for the SOI and the planar solar cells are given in Figure 23.

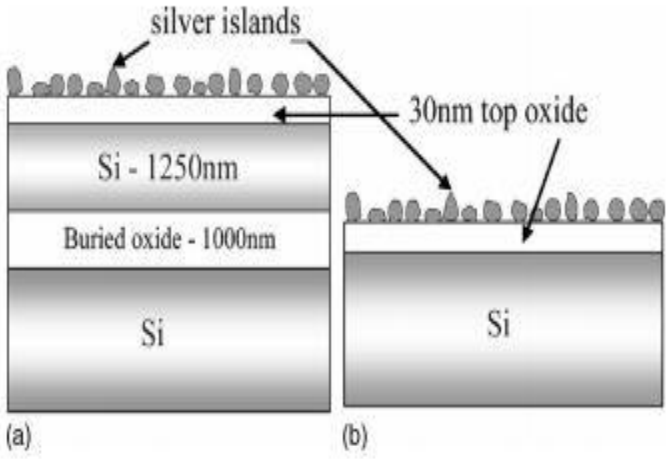

Figure 23. The silicon test structures used. (a) Silicon-on-insulator (SOI) with 1.25µm active Silicon and (b) wafer based 300 µm planer Silicon cell [5].

The SOI cells used here were formed from a lateral pn junction diffused into a p-type layer. The p and n metal contacts were interdigitated for maximum carrier extraction. The thicknesses of the Si and buried oxide layer which were determined from reflectivity measurements and W-Vase simulation were found to be 1250 nm and 1000 nm respectively [5]. All the cells had a thin 30 nm top oxide which acts as a passivating layer, the thickness of which strongly influences the coupling between the active silicon and the plasmons.

The bare island resonance of the particles is the resonance of the particles on a low refractive index medium, which was done to minimize the interaction between the substrate and the nanoparticles. The bare island resonance of the Ag nanoparticles was measured on a plain microscope glass slide, which was used as a substrate. The particles formed as a result of

annealing tend to become larger, more elongated (loose the spherical shape), and also more irregular as the mass thickness of Ag is increased. This causes the bare island resonance to red shift as seen from the transmittance plot in Figure 24.

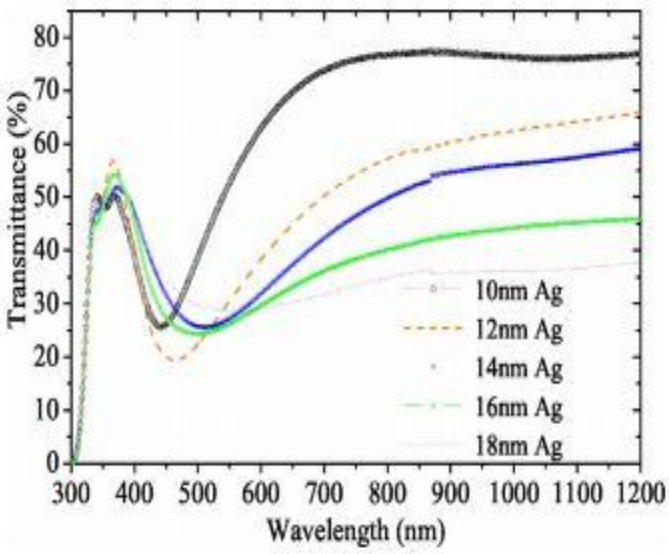

Figure 24. Transmittance measurements showing red shifting of the bare island resonance of particles corresponding to increasing mass thickness of silver, which implies larger particle sizes [5].

A dip in the transmittance plots shows the resonance position. The resonance curves are sharper for lower mass thickness and tend to broaden for larger mass thicknesses [5]. The bare island resonance plot can give the extinction (1- transmittance) of the nanoparticles and can be used as a good starting point in understanding the absorption in the solar cell structures incorporated with metal nanoparticles.

Figure 25(a) below shows the photocurrent enhancement from the 1.25 µm SOI solar cell. It is interesting to note here that there is an overall increase in current throughout the visible and the near-infrared and a close to 16-fold enhancement at around 1050 nm with particle sizes corresponding to 16 nm mass thickness of Ag. These results correspond to a 33% increase of the total current of the device, when averaged over AM 1.5 global radiation for particle sizes corresponding to 12 nm mass thickness of Ag and 16% increase for particle

sizes corresponding to 16 nm Ag thickness [5]. Figure 25(b) shows a comparison of the modeled and experimental results. The plot shows the effect of the plasmons both with and without the effect of the waveguide on the scattering cross section of the particles for externally incident light.

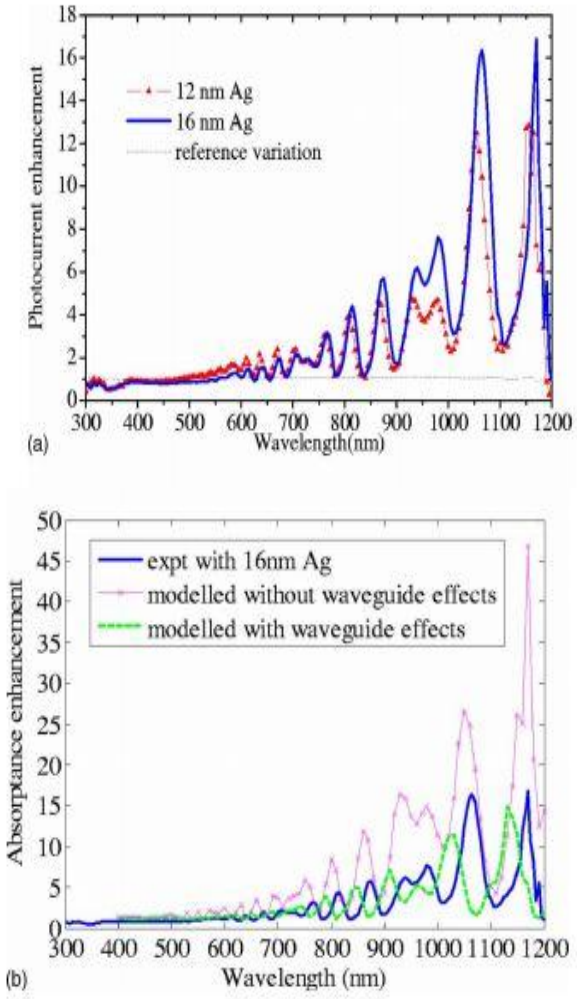

Figure 25. (a) Photocurrent enhancement from a 1.25 µm thick SOI solar cell for particle sizes corresponding to 12 and 16nm mass thickness of Ag relative to the cell without silver particles. (b) Photocurrent enhancement for the 1.25 µm SOI device with 16nm mass thickness Ag particles, and modeled results with and without modification of the scattering cross section for normally incident light by the waveguide [5].

It can be seen that there is a better agreement in the position of the peaks when it is assumed that the waveguide does not modify the external scattering cross section. The effect of including the waveguide modification for externally incident light is that the scattering cross section is enhanced at some wavelengths because the local field is enhanced due to constructive interference of the incident and reflected light, and decreased at other wavelengths due to destructive interference [5]. The overall effect is the shift in the position of the enhancement peaks. One explanation to the fact that the model predicts larger peaks than those observed experimentally can be that it is based on the bare island resonance data for particles on glass, which are known to be more elongated owing to the reduced refractive index of the glass slide, with a larger variety of shapes than particles deposited on silicon with equivalent deposition parameters.

Similar plots for the 300 μm planar silicon solar cell were observed and are shown in Figure 26. The corresponding increase in the photocurrent with AM 1.5 global spectrum for 12,14, and 16 nm mass thickness of Ag are approximately 19%, 14%, and 2% respectively [5]. In general, the photocurrent enhancement is more evident for larger sized particles at longer wavelengths close to the silicon band gap, where the potential for enhancement is larger.

The smaller sized particles contribute to the enhancement in the entire wavelength range above 500 nm, which explains the overall increase in enhancement of the particles corresponding to 12 nm mass thickness of Ag [5]. The results show good agreement with the modeled result shown in Figure 26(b). Here again, the larger enhancement in the model at long wavelengths seem likely to be due to a broader surface plasmon resonance for particles on glass than particles on silicon.

While larger particles tend to give a bigger enhancement at longer wavelengths, smaller particles give increased absorption in the visible regime. From the above results it can be seen that (a) enhancement is significant for thinner layers over the entire spectrum and (b) with increasing particle sizes there tends to be a reduction in absorption at shorter wavelengths, and an increase at longer wavelengths.

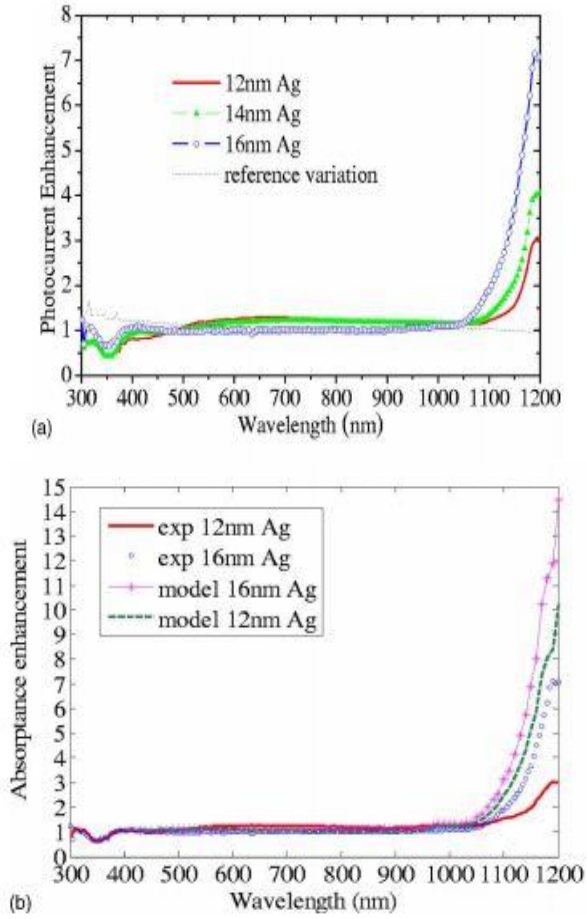

Figure 26. (a) Photocurrent enhancement for a 300 µm Si solar cell for particle sizes corresponding to 12,14 and 16 nm mass thickness of Ag in comparison to the cell without Ag particles. (b) Modeled enhancement result for a wafer-based planar Si solar cell [5].

The wafer based cells are thick and are already good absorbers in the visible region, hence the enhancement in the visible region is not very prominent but it is quite significant close to the band gap. But, in contrast to the case for thin films, the impact of the larger sized particles for wafer based cells is clearly evident. Smaller particles have a smaller scattering cross section and lower radiative efficiency, and hence tend to blue shift the absorption peak compared to larger particles with higher scattering cross section and radiative efficiency. However, there is an optimum size of the particles beyond which large particles tend to

initiate multipole oscillations, which eventually tends to reduce the scattering efficiency. Hence, it is necessary to optimize the particle size to get an overall enhancement over a broad wavelength regime [5].

Plasmon enhancement has also been reported for other semiconductors than silicon. Here, early work was done by Stenzel et al. who reported an enhancement in photocurrent of a factor of 2.7 for ITO-copper phthalocyanine-indium structures [1].

Westphalen et al. reported an enhancement for silver clusters incorporated in an ITO and zinc phthalocyanine solar cell [1].

Nakayama et al. demonstrated an improvement in efficiency of optically thin GaAs solar cells incorporated with size controlled Ag nanoparticles fabricated by masked deposition through anodic aluminum oxide (AAO) templates. The strong scattering by interacting surface plasmons in densely formed nanoparticles effectively increased the optical path of the incident light in the absorber layers resulting in an 8% increase in the short circuit current density of the cell [6].

AAO can serve as an evaporation mask for metal deposition to form size-controlled nanoparticle array on a substrate. The through-hole AAO template was placed directly onto the window layer of the GaAs solar cell. Thermal evaporation of Ag through the AAO templates resulted in formation of dense arrays of Ag nanoparticles (110 nm diameter) on GaAs solar cells which possess the same diameters and interparticle spacing as the nanopores in the AAO templates [6]. The height of the nanoparticles can be controlled simply with the deposition thickness. The nanoparticles would change their shape from hemispheres to cones as their height keep on increasing.

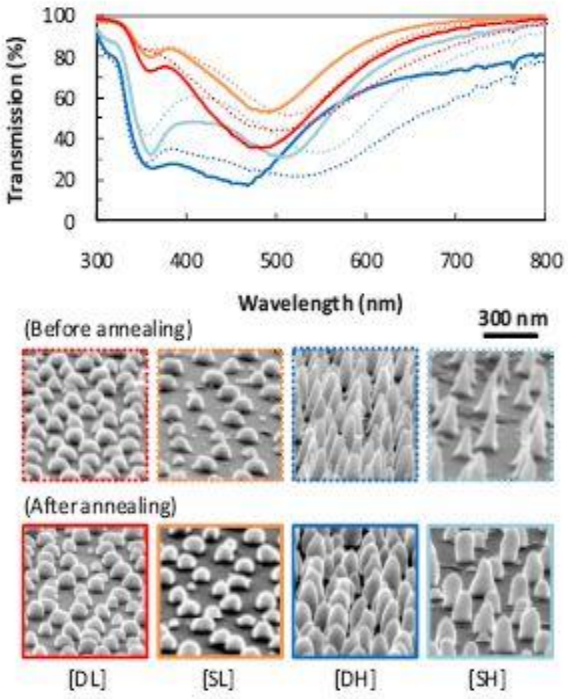

Figure 27. Extinction spectra of the Ag nanoparticles on glass substrates before (dot lines) and after annealing at 200o C (solid lines) corresponding to the SEM images below [6].

The extinction spectra along with the scanning electron microscope (SEM) images of the glass slides after the Ag deposition and subsequent annealing are shown above in Figure 27. Four arrays of nanoparticles were studied by Nakayama and group; densely formed low (DL), sparsely formed low (SL), densely formed high (DH), and sparsely formed high (DH). Low and high represents the height of the nanoparticles or in other words the elongatedness of their cone structure.

The relatively sharp absorption peak at 360 nm (as seen in Figure 27) is related to the electronic interband transitions in Ag. Annealing the nanoparticles resulted in blueshifting the surface plasmon resonances, which are attributed to the improvements in the symmetry of these nanoparticles [6].

In the GaAs solar cell, the photovoltaic layers were intentionally designed to be much thinner than the absorption length. It was grown on *n*-GaAs substrate by metal organic chemical vapor deposition with Zn as the *p*-type dopant and Si as the *n*-type dopant. In addition, a high band gap back surface field (BSF) layer of *n*-$Al_{0.8}Ga_{0.2}As$ was formed to prevent carrier generation in this layer. Half of the light above the band gap of GaAs is absorbed by the *p*-$Al_{0.8}Ga_{0.2}As$ window and *p-n* GaAs photovoltaic layers and the remaining light transmitted through the layers is absorbed by the underlying GaAs without carrier collection. After both front and bottom Au contacts were formed [6]. The layered structure of the cell along with the current density and EQE plots are shown below in Figure 28.

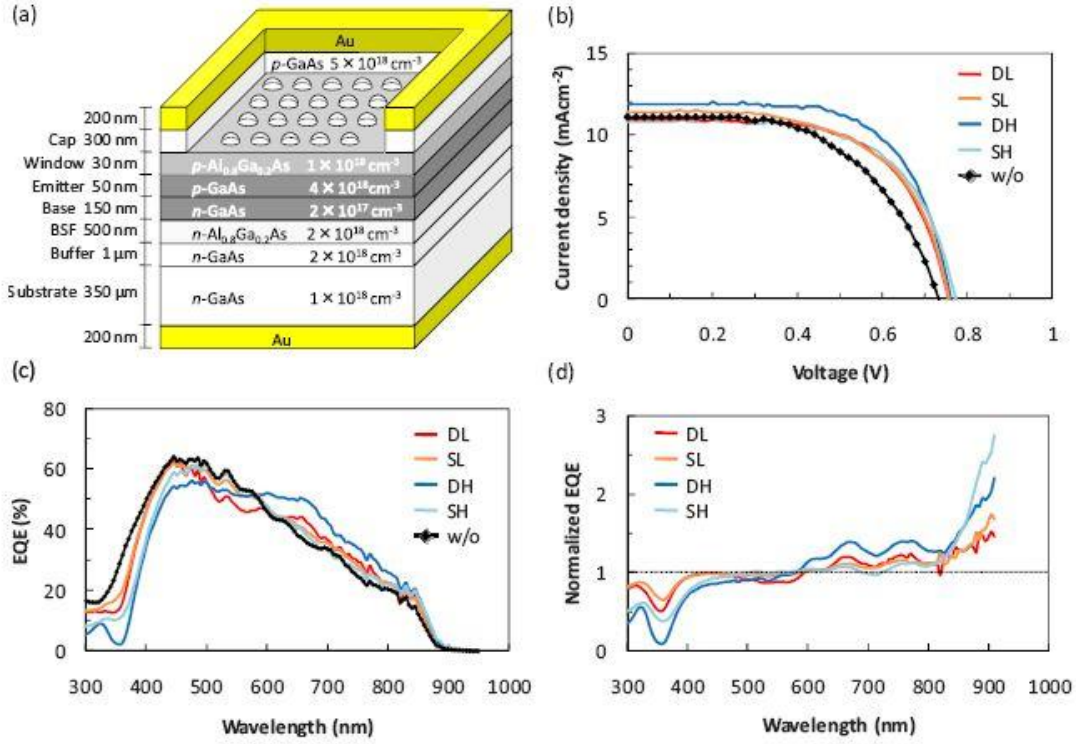

Figure 28. (a) A layer structure of the GaAs solar cell. (b) Photovoltaic I-V curves for the GaAs solar cells under one-sun illumination (AM1.5), using a solar simulator. (c) Photovoltaic spectral responses for the GaAs solar cells measured by shining monochromatic light. (d) Normalized spectral responses for the nanoparticle-decorated GaAs solar cells by the spectrum for the reference cell [6].

The arrays had great influence on the photocurrent of the cells, in which the best photocurrent enhancement was induced by the DH nanoparticles with an 8% increase in the short circuit current density (*J*sc) [6]. The external quantum efficiencies (EQEs) of the nanoparticle incorporated cells were normalized by that of the reference cell (28d). This gave a nice demonstration of the enhancement compared to the reference. All the nanoparticle-incorporated solar cells have reduced photocurrents below 600 nm where the surface plasmon resonance effects show up more strikingly, while the cells have the enhanced photocurrent responses at longer wavelengths. This is in agreement to all the previous works mentioned in this section.

The sparse nanoparticle arrays enable the reduction in the loss of incident light resulting from either absorption or backscattering by the nanoparticles near the surface plasmon resonances, while the plasmonic scattering can be enhanced in the dense array cases at wavelengths below the surface plasmon resonances. Especially the DH nanoparticles significantly enhance the photocurrent, which can be attributed to the strong scattering by the interacting surface plasmons [6].

Table 1. I-V characteristics of the GaAs solar cells.

	Designed values						
Ag array	Diameter (nm)	Height (nm)	Density (cm^{-2})	J_{sc} ($mA\,cm^{-2}$)	V_{oc} (V)	FF	η (%)
DL	110	55	3.3×10^{9}	10.9	0.76	0.62	5.1
SL			1.8×10^{9}	11.4	0.75	0.60	5.1
DH		220	3.3×10^{9}	11.9	0.76	0.65	5.9
SH			1.8×10^{9}	10.8	0.77	0.64	5.3
W/o	N/A (reference)			11.0	0.73	0.55	4.7

Table 1 above lists the measured I-V characteristics of the GaAs solar cells.

Another advantage of nanoparticle arrays as seen from Table 1 is the improvements in the fill factor (FF) for the cells, indicating the reduction in the surface sheet resistance. This effect can be expected in all solar cells that form Ohmic contact between the nanoparticle array and the cell window layer. This suggests, that in even optically thick cells, plasmonic nanoparticles could be employed to serve as transparent conductors to increase the FF and in turn the cell efficiency for thin lightly doped top window layers, though they do not increase the photocurrent [6].

The scope of plasmons are not limited to just semiconductor based solar cells. Rand et al have reported enhanced efficiencies for ultra-thin film tandem organic solar cells due to the presence of very small Ag nano clusters [7]. The optical field enhancement caused by plasmons on the cluster surfaces is, in part, responsible for the high efficiencies observed in tandem organic PV cells whose individual subcells are separated by ultrathin metal cluster layers. Figure 29 shows the schematic diagram and the high resolution transmission electron micrograph (TEM) of a cross section of a tandem organic PV cell.

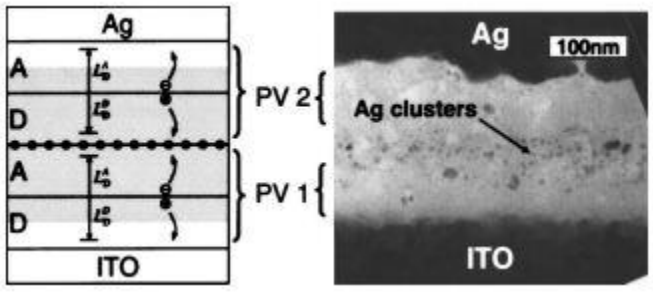

Figure 29. Schematic (left) and TEM (right) of a cross section of a tandem organic solar cell [7].

The two cells (labeled PV1 and PV 2) are contacted by an indium tin oxide (ITO) anode and a Ag cathode, and are separated by a Ag nanocluster layer. The enhancement distance (shaded region) and the diffusion lengths L_D^D and L_D^A of the donor (D) layer and acceptor (A) layer of each device are also shown. The organic layers consisted of the electron donor,

copper phthalocyanine (CuPc), and the acceptor, 3,4,9,10- perylenetetracarboxylic bis-benzimidazole (PTCBI) [7].

When light is absorbed, excitons are formed in both photovoltaic subcells. After dissociation at a DA interface, the hole in PV 1 and electron in PV 2 are collected at the adjacent electrodes. The buildup of charge is prevented by recombination of the electron from PV 1 and hole from PV 2 in the metal nanocluster layer. The attraction of the initial charge to the nanoparticle is primarily a result of image charge effects. Once the metal particle is singly charged, the coulomb attraction of the free counter charge leads to a rapid recombination at the Ag surface. Metal nanoclusters can also increase the incident optical field, which in turn enhances the absorption in the nearby organic thin film. The field enhancement results from the surface-plasmon polariton (SPP) resonances which are optically excited on the metal particle surfaces [7]. The SPP resonance originates from the displacement of the negative conduction electrons against the positively charged background due to an applied electric field. This results in polarization charges at the cluster surface which leads to a restoring force and thus a resonance eigen frequency [7]. The measured absorption spectra for three films on quartz with and without nanoclusters are shown in Figure 30.

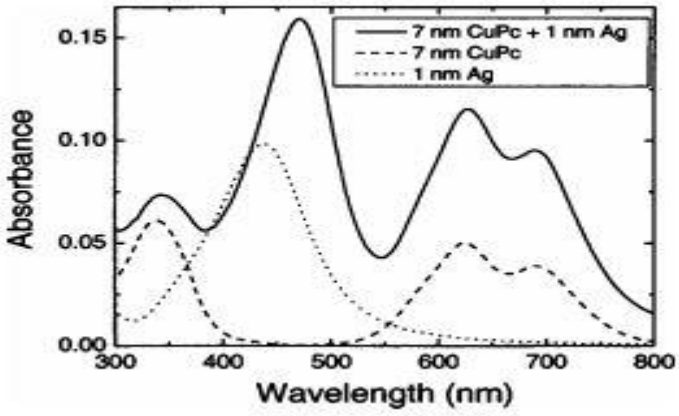

Figure 30. Measured absorption spectra for 1 nm Ag (dotted curve), 7 nm CuPc (dashed curve) and 7 nm CuPc film on 1 nm Ag (solid curve). All films are deposited on quartz substrates [7].

From the above figure it can seen that the 1 nm thick Ag island film has a 100 nm wide peak centered at a wavelength of λp =440 nm , which is due to surface-plasmon excitation of the nanoclusters. The peak position and intensity are indicative of a distribution in particle shape and size, as well as the dipolar coupling between clusters that broadens the optical response with decreasing particle spacing. Absorption by a 7 nm thick film of CuPc is also shown. The solid curve represents the 7 nm thick CuPc film deposited on top of the 1 nm thick Ag film. Due to the CuPc dielectric, the plasmon peak of the Ag cluster layer is red shifted by 30 nm to λp =470 nm. The most evident feature, however, is the increase of CuPc absorption at wavelengths λ >470 nm. This broadband, nonresonant enhancement leads to an approximately 15% increase in the efficiency of tandem PV cells [7].

Figure 31 shows a representative field distribution for a one-dimensional (1D) array of Ag cylinders on a quartz substrate surrounded by a CuPc dielectric of finite thickness with a diameter of 5 nm and a uniform surface-to-surface spacing δ=5 nm.

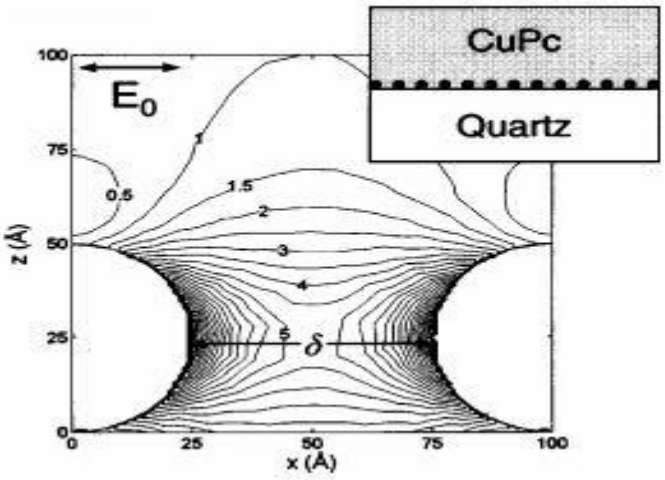

Figure 31. Contour map of the calculated intensity enhancement (I / Io) of a chain of Ag particles .The particles lie on a quartz substrate and are embedded in a dielectric medium (CuPc). Contour labels represent the intensity enhancement and are spaced by 0.5. Inset: schematic of the simulated geometry containing a CuPc film on a Ag cluster covered quartz substrate [7].

The field distribution is for an excitation wavelength of λ=690 nm, polarization parallel to the nanoparticle chain and propagation in the +z direction. The contours indicate the intensity

enhancement of the electric field, I / I_0, where I is the local-field intensity and I_0 is the intensity of the incident field. These intensities are proportional to the squares of their electric-field amplitudes; $|E|^2$ and $|E_o|^2$ respectively. Twelvefold intensity enhancements are found in the interstices of the Ag cylinders [7].

Other works, in use of plasmon to enhance efficiency of organic solar cells have also been demonstrated. Morfa et al. have reported an increase in efficiency by a factor of 1.7 for organic bulk heterojunction solar cells. Plasmon-active silver nanoparticle layers were included in solution-processed bulk-heterojunction (BHJ) solar cells. Nanoparticle layers were deposited by vapor-phase deposition on indium tin oxide electrodes. Due to the increase in electrical field inside the photoactive layer, the inclusion of such metal particle films lead to increased optical absorption and subsequently increased photo conversion at certain wavelengths. The active layer for this device consisted of a 1:1 mixture of poly (3-hexylthiophene) (P3HT) and [6, 6]-phenyl C_{61}butyric acid methyl ester (PCBM). The P3HT: PCBM system was chosen for its proven photovoltaic device efficiency and its ease of fabrication [8]. Light absorbed in the bulk heterojunction active layer, generates mainly excitons that dissociate into electrons and holes. Exciton dissociation takes place by charge separation between the electron donor, P3HT, and the electron acceptor, PCBM. Since the dipole allowed photogeneration of excitons in the BHJ layer should scale with the electric field squared, it can be hypothesized that by enhancing the local electro-magnetic field with the inclusion of surface-plasmon active materials, enhancing the photogeneration of excitons in P3HT and, to a lesser degree, in PCBM is possible [8]. Enhancements to the photogeneration of excitons would lead to a higher observable photocurrent from wavelengths near the plasmon resonance towards longer wavelengths.
Discontinuous Ag thin films deposited on the ITO glass provide an easy to fabricate, optically tunable surface plasmon active system. By varying average film thickness, the surface plasmon resonance can be tuned from the blue to the red region of the visible spectrum. The final device structure with an incorporated plasmon active Ag layer is shown

schematically in Figure 32. Thin Silver film thicknesses of 1, 2, 3, and 4 nm were chosen to minimize the amount of light absorbed before reaching the active layer.

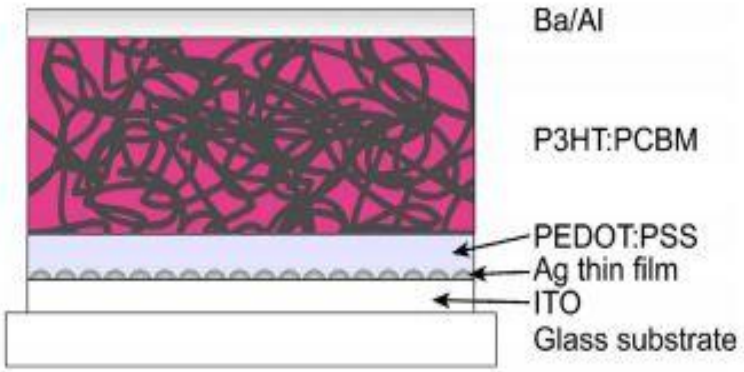

Figure 32. The device fabricated with a thin silver film deposited onto ITO on a glass substrate. PEDOT: PSS was spun onto the silver layer followed by P3HT: PCBM and a barium/aluminum back electrode [8].

The average island diameter for 2 and 4 nm thick films were 11.6 and 13.0 nm respectively. To determine the effect of the plasmon-active layer on the exciton creation in the BHJ layer, current-voltage (IV) and incident photon-to-current conversion efficiency (IPCE) measurements were performed.

For the 1nm Ag film thickness, the average short current density (J_{sc}) was 6.93 mA/cm^2. This is a 1.49 fold increase over the average reference J_{sc} of about 4.65 mA/cm^2. The highest increase in J_{sc} was observed for devices with 2 nm thickness of Ag. The average Jsc value was 7.33 mA/cm^2, which is an increase of factor of 1.58 over the average reference value. The maximum J_{sc} observed was 7.71 mA/cm^2, a 1.43 fold increase with respect to the maximum reference Jsc of 5.39 mA/cm^2 [8]. As the Ag film thickness was increased beyond 2 nm, a downward trend in

Jsc was observed. Table 2 shows an overview of the relevant average device parameters [Jsc, efficiency (η) and open-circuit voltage (V_{oc})] with their associated standard deviations. On average, the reference and devices incorporating 1 nm of Ag were 1.31% and 2.23% efficient respectively. This corresponds to an increase of a factor of 1.7.

Table 2. Average device parameters as a function of nominal silver film thickness.

Ag height (nm)	J_{sc} (mA/cm^2)	η (%)	V_{oc} (mV)
0 (Ref)	4.6±0.4	1.3±0.2	566±5.6
1	6.9±0.2	2.2±0.1	590±5.8
2	7.3±0.3	2.1±0.1	581±8.8
3	6.5±0.1	1.8±0.2	564±30.9
4	2.6±0.4	0.9±0.1	599±6.2

Beyond about 2 nm of Ag, the efficiency decreases again. The V_{oc} decreases slightly with increasing silver coverage. The IPCE spectra are shown in Figure 33.

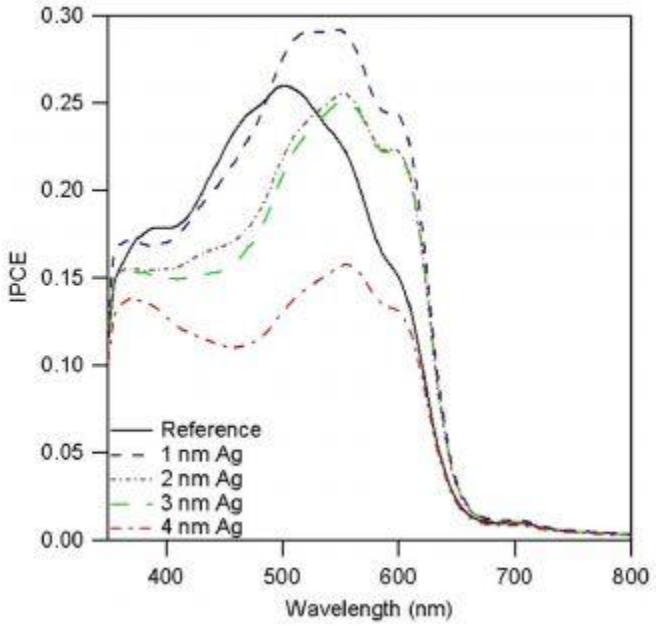

Figure 33. IPCE spectra of devices containing 1, 2, 3, and 4 nm silver films demonstrate the increased photocurrent at wavelengths over 500 nm. The strong absorption of the silver films on the IPCE is also seen as a dip centered near 450 nm [8].

Two significant differences with respect to the reference are observed. The Ag samples show a decrease in quantum efficiency at around 450 nm. This corresponds with the dip observed in the transmission spectra due to the surface plasmon resonance of the Ag nanoparticles (not

shown here). At longer wavelengths (>500 nm), a strong increase in external quantum efficiency is observed in all silver samples, except that with a thickness of 4 nm. This increase is the source of the increased short circuit current and thus the efficiency [8].

3.20 Summary

The works of a lot of research groups were talked about in this section. The studies relating to the improvement in different types solar cell performances by the plasmon theory was explained.

Table 3 sums up the different studies undertaken by these research groups and their significant contribution to this field.

Table 3. Research work and contributions in the field of plasmons for photovoltaics.

Research Group	Type of Photo Device	Contribution
Stuart and Hall	SOI photodetector	Near 20 fold photocurrent enhancement observed at around 800 nm with Ag nanoparticles.
Schaadt et al.	Silicon pn junction diode	Photocurrent enhancement of up to 80% obtained around 500 nm with Au nanoparticles.
Derkacs et al.	Silicon p-i-n solar cell	8.1% increase in J_{sc} and 8.3% increase in energy conversion efficiency using Au nanoparticles.
Pillai et al.	Silicon wafer based cells and thin SOI cells (1.25 μm)	7 fold photocurrent enhancement for wafer based cells at 1200 nm and a 16 fold increase for thin SOI cells at 1050

		nm with Ag nanoparticles.
Nakayama et al.	Thin GaAs solar cells	8% increase in J_{sc} of the cell with Ag nanoparticles.
Rand et al.	Organic Tandem thin film cells	14 % increase in J_{sc} with Ag nanoparticles.
Morfa et al.	Organic bulk heterojunction cells	Improvement factor of 1.7 observed in solar energy conversion with Ag nanoparticles.

Note that the results mentioned in the table above are focused mostly on improving the performance of thin film solar cells. In our work, we will examine the plasmon enhancement in commercially available wafer based cells.

3.30 References

[1] K. R. Catchpole and A. Polman, "Plasmonic solar cells," Optics Express, vol. 16, pp. 21793-21800, Dec 2008.

[2] H. R. Stuart and D. G. Hall, "Island size effects in nanoparticle-enhanced photodetectors," Applied Physics Letters, vol. 73, pp. 3815-3817, Dec 1998.

[3] D. M. Schaadt, et al., "Enhanced semiconductor optical absorption via surface plasmon excitation in metal nanoparticles," Applied Physics Letters, vol. 86, Feb 2005.

[4] D. Derkacs, S. H. Lim, P. Matheu, W. Mar, and E. T. Yu, "Improved performance of amorphous silicon solar cells via scattering from surface plasmon polaritons in nearby metallic nanoparticles," Applied Physics Letters, vol. 89, Aug 2006.

[5] S.Pillai, "The effect of dielectric spacer thickness on surface plasmon enhanced solar cells for front and rear side depositions". Journal of applied physics (0021-8979), 109 (7), p. 073105, 2011

[6] K. Nakayama, et al., "Plasmonic nanoparticle enhanced light absorption in GaAs solar cells," Applied Physics Letters, vol. 93, Sep 2008.

[7] B. P. Rand, P. Peumans, and S. R. Forrest, "Long-range absorption enhancement in organic tandem thin-film solar cells containing silver nanoclusters," Journal of Applied Physics, vol. 96, pp. 7519-7526, Dec 2004.

[8] A. J. Morfa, K. L. Rowlen, T. H. Reilly, M. J. Romero, and J. van de Lagemaat, "Plasmon-enhanced solar energy conversion in organic bulk heterojunction photovoltaics," Applied Physics Letters, vol. 92, Jan 2008.

CHAPTER 4

EQUIPMENT AND TOOLS

This chapter discusses about these tools and equipment which were used to prepare and characterize the samples.

4.10 Electron Beam Deposition Tool

The gold film was deposited on the samples by Edwards Auto 360 electron beam tool (shown in Figure 34).

Figure 34. Edwards auto 360 e-beam deposition tool.

The samples were placed on a rotating plate inside a chamber which was pumped down to a pressure of 2.5e-5 Torr. The current was slowly ramped up to 65mA (for gold). At this point the filament of the electron gun gets hot enough to emit a beam of electron towards the target metal which is placed in a crucible. When the electron beam strikes the metal target, the kinetic energy of motion gets converted by the impact into thermal energy. This causes the atoms of the target metal to be released from its surface and be deposited on the sample. The deposition rate was usually around 0.02-0.06 nm/s. The thickness of the film can be controlled by observing the reading of the quartz crystal monitor. Gold thicknesses ranging from 4-20 nm were deposited for this research through this process. Other metals like aluminum, titanium and chromium can also be deposited by this tool.

4.11 Plasma-Enhanced Chemical Vapor Deposition (PECVD)

To deposit the dielectric spacer layer (SiO_2, Si_3N_4), PECVD tool was used (shown in Figure 35). This is normally a low temperature deposition process (300-400^o K).

Figure 35. Plasmalab PECVD system.

In this method, deposition of thin films from a gas state (vapor) to a solid state on a substrate is done. The plasma is generally created by RF (AC) frequency or DC discharge between two electrodes, the space between which is filled with the reacting gases.

For oxide deposition, silane (SiH_4) and nitrous oxide (N_2O) are used as feedstock. The reaction that takes place is as follows:

$$3SiH_4 + 6N_2O \rightarrow 3SiO_2 + 4NH_3 + 4N_2$$

For nitride deposition, silane and ammonia (NH3) are used as feedstock. The reaction that takes place is as follows:

$$3SiH_4 + 4NH_3 \rightarrow Si_3N_4 + 24H_2$$

PECVD nitride is suitable for passivation layers.

4.12 Atomic Force Microscopy (AFM)

AFM was used repeatedly from time to time in this research to characterize the samples. The AFM tool used is shown in Figure 36.

AFM images give a decent idea about the particle distribution and sizes and also the surface roughness. The AFM tool consists of a cantilever with a sharp tip (probe) which scans the surface of the sample. The cantilever is usually silicon or silicon nitride with tip's radius of curvature of the order of nanometers. Forces between the tip and the sample lead to a deflection of the cantilever when the tip is brought into close proximity with the surface of the sample. This deflection is measured by a laser spot reflection from the top surface of the cantilever into an array of photodiodes. In most AFM systems, a feedback mechanism is also applied to adjust the tip to sample distance to maintain the same amount of force between the tip and the sample.

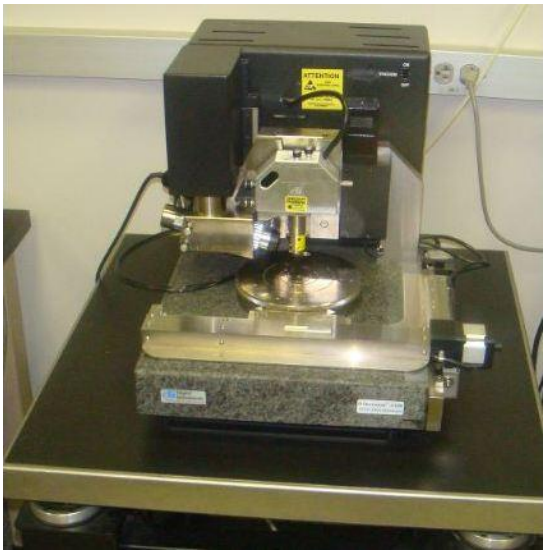

Figure 36. AFM tool.

4.13 High Temperature Furnace

Annealing of the samples was done in a high temperature tube furnace (shown in Figure 37). The sample temperature can be controlled from room temperature to 900^{o} C. The furnace enables annealing to be performed in both air and nitrogen environment. For this research all the samples were annealed in air.

Figure 37. High temperature tube furnace.

4.14 Spectrophotometer

The transmission and reflectance measurements (function of wavelengths) of the samples were performed using a Perkin-Elmer Lambda 9 spectrophotometer (shown in Figure 38). The lambda 9 is a versatile, high performance double-beam, double-monochromator UV/visible/near IR spectrometer. A double beam spectrophotometer is one which compares the light intensity between two light paths, one path containing a reference sample and the other the test sample. Two pre-aligned radiation sources, a deuterium lamp (for UV) and a halogen lamp (for visible and near IR) cover the working wavelength range of the spectrometer. It has a side window photomultiplier for UV/Visible range and a PbS (Lead sulfide) detector for the near IR range.

Figure 38. Perkin-Elmer Lambda 9 spectrophotometer.

4.15 Solar Simulator

The I-V measurements were done with the help of an Oriel 1kW solar simulator with a 1.5D filter (shown in Figure 39). Solar simulators can replicate the sun's illumination in an indoor environment. The power density of the oriel simulator with 1.5D filter is around 763 W/m^2.

Figure 39. An Oriel 1kw solar simulator with a 1.5D filter.

4.20 Fabricating Nanoparticles

Metal nanoparticles can be fabricated in many different ways depending on the application. There are many deciding factors which influence the fabrication method. Some of them are the cost, complexity of the process, arrangement of the nanoparticles (periodic/non-periodic) and the spacing between the nanoparticles (pitch). In this section we discuss the method employed for this research.

4.21 Metal Deposition and Annealing

This is probably the easiest and the cheapest method of fabricating metal nanoparticles. It is widely used to deposit random arrays of nanoparticles or so called 'metal islands'. The metal to be deposited (Ag/Au) is sputtered/evaporated onto the target substrate in an electron-beam deposition tool. Subsequent annealing follows the metal deposition which allows the thin metal films to contract into spherical particles. For this research, the samples were annealed at a temperature range of 200-300^{o} C for a period of 1 hour in a high temperature furnace.

Depending on the process conditions, the metal agglomerates due to surface tension and forms islands or random sized particles.

The thickness and the annealing conditions (temperature/duration) can be varied accordingly to get the desired size of the nanoparticle. Although this process doesn't guarantee uniform the particle size throughout the sample, it is the simplest method available to form these nanostructures and that's the reason this technique was chosen for this research.

4.22 EQE Response

The apparatus used to measure the EQE response was initially calibrated to a reference silicon sample. Thus all the EQE measurements done for this research are relative to that reference silicon sample and are not an absolute value.

The photocurrent was calculated by the integrating the following equation over the entire spectrum:

$$\boldsymbol{J_{sc}(\lambda) = Responsitivity\ X\ AM\ 1.5D\ spectrum}$$

Where $\boldsymbol{Responsitivity = EQE\ X\ \frac{\lambda}{hc/q}}$,

h: Planck's constant , c: Speed of light , q: Electron charge , λ: Wavelength of light

CHAPTER 5

RESULTS & DISCUSSIONS

5.10 Thin Film Characterization

Thin gold films were deposited on plain glass slides in the electron-beam evaporator. 6nm, 8nm and 12nm films as measured by the quartz crystal monitor were obtained at the end of the deposition. These films were then annealed in a tube furnace at different temperatures and for different times in order to control the size of the resulting nanoparticle which formed on the surface due to the surface tension of gold. The annealing was done in air at temperatures ranging from 200 – 400^{o} C. The annealing time was varied from 5 minutes to 1 hour. The resulting particles were then characterized by AFM and optical spectroscopy.

Transmission and reflection analysis can be done for these thin films using a spectrophotometer. The optical spectroscopy helps in understanding the desirable and the undesirable feature which can be used for a better understanding and for improving the processing conditions. For the solar cell application, more scattering into the cell, less reflection from the cell and less absorption of incident light by the nanoparticles is desired. The absorption in the nanoparticles (on glass slides) can be estimated by:

Absorption= 1- (Transmission + Reflection)

Unlike solar cells, there is no absorption in the glass slides and hence the absorption in the nanoparticles can be accurately determined.

The transmission and reflection spectroscopy are done for the thin films on the glass slides for a better understanding of the effect of variable particle sizes on their optical properties.

As mentioned in the previous sections, the size of the particle plays an important role in determining the amount of scattering and absorption. Since our method of fabricating

nanoparticles is relatively simple, it does not accurately control the size of these particles however it can still provide some valuable information about the trends obtained as the process conditions are changed. The deposition of gold films on the glass slides gave an idea of the thicknesses which were to be deposited on the solar cell in order to obtain the right particle size.

5.11 6nm gold film thickness

Gold thickness of 6nm was deposited on the glass slide and annealed at different temperatures (200^{o} C, 300^{o} C and 400^{o} C) for a period of 1 hour. AFM images of the resulting particles are shown in Figure 40.

It can be clearly seen from the images that as the annealing temperature is increased, the size of the particles also increases. This can be attributed to the fact that at higher temperatures, more and more gold particles agglomerate and form bigger particles.

In addition, the particles lose their spherical shape and become more elongated. This is an important aspect which helps to explain the red shift in the plasmon peaks during the transmission and reflection spectroscopy.

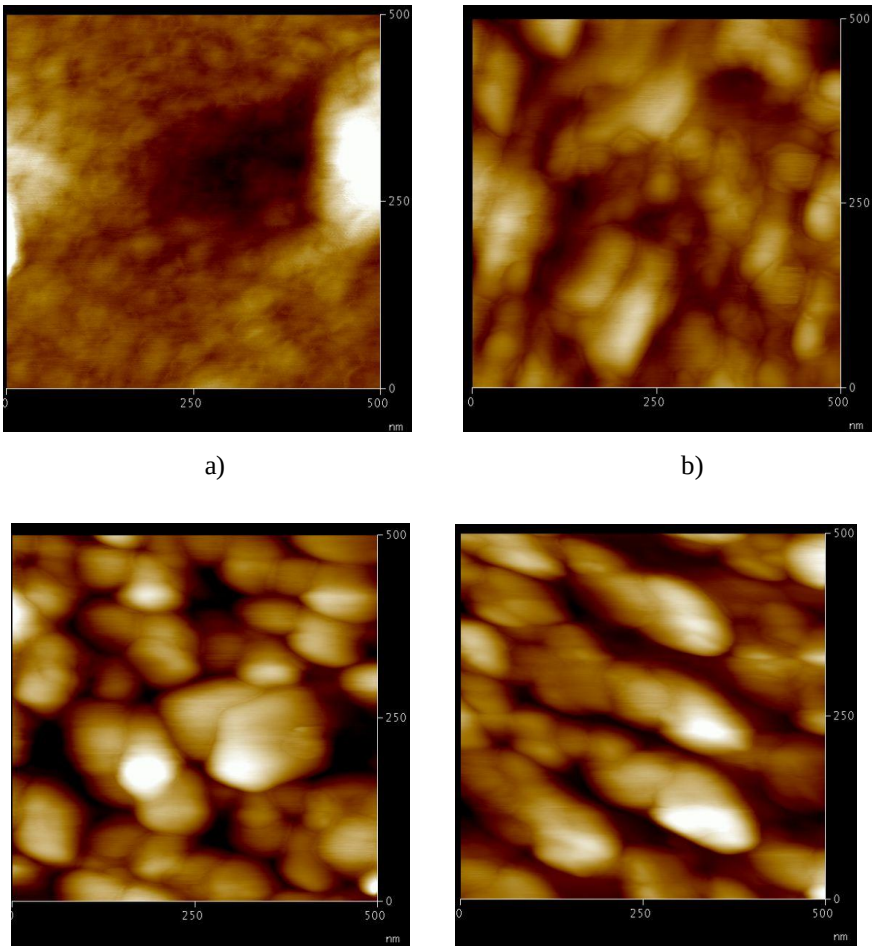

Figure 40. AFM images (taken at 500nm) of 6nm gold film annealed at different temperatures for 1 hour: a) no anneal, b) 200^{o} C, c) 300^{o} C and d) 400^{o} C.

Table 4 shows the gold nanoparticle sizes for a 6nm film annealed at different temperatures. The size of the particle was calculated by the section analysis of the AFM image.

Table 4. Size of nanoparticles at different annealing temperatures for 6nm gold film.

Annealing Temperature	Size of the nanoparticle
200° C	63 nm
300° C	100 nm
400° C	272 nm

Figure 41 shows the transmission spectroscopy of the 6nm gold film annealed at different temperatures. From the figure it can be seen that, as the gold film is annealed, the plasmon peak becomes more visible (around 500 nm).

The plasmon related dip can also be seen at higher temperatures. It becomes more narrower and shifts to a lower wavelength with the increase in temperature.

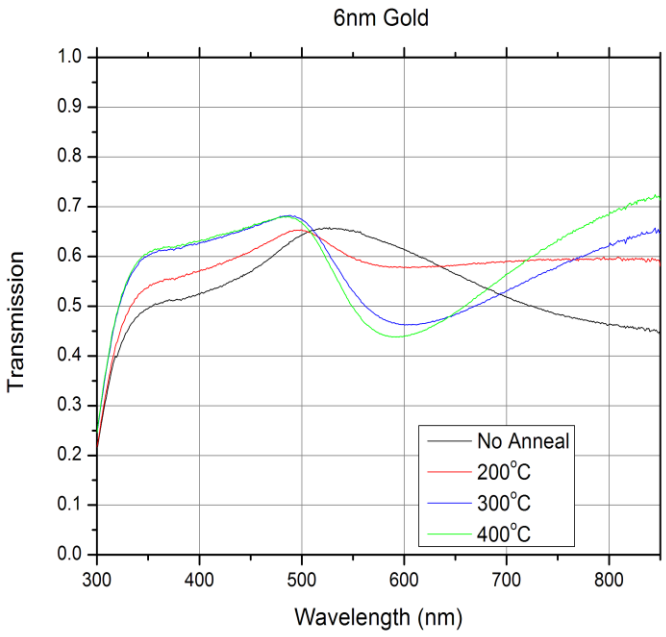

Figure 41. Transmission spectroscopy of 6nm gold film annealed at 200° C, 300° C and 400° C.

From the scattering and absorption cross-section equations mentioned in the earlier sections, it is well established that the smaller particles absorb more light and as particles become

become bigger in size, scattering dominates and absorption is less. The scattering can be of two types; forward or back scattering. The former can be seen as transmission and the later as reflection for our case. As seen in Figure 41, the transmission is more for gold films annealed at a higher temperature (400^{o} C and 300^{o} C) which corresponds to bigger particle sizes.

Figure 42 shows the reflection spectroscopy of the 6nm gold film at different temperatures.

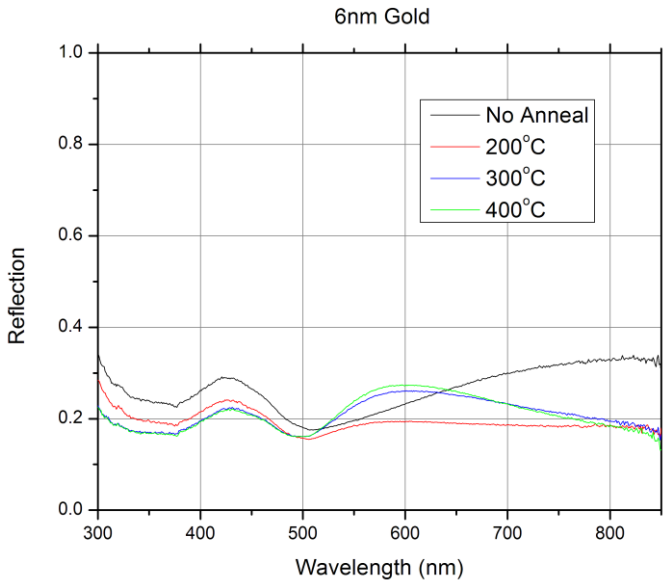

Figure 42. Reflection spectroscopy of 6nm gold film annealed at 200^{o} C, 300^{o} C and 400^{o} C.

The reduction in reflection for films annealed at higher temperatures can be attributed the opening up of more spaces; the increase in spacing between particles due to increase agglomeration of gold particles at higher temperatures. The film is no longer continuous and is less reflective.

5.12 8 nm gold film thickness

Gold thickness of 8nm was deposited on the glass slide and annealed at different temperatures (200^{o} C, 300^{o} C and 400^{o} C) for a period of 1 hour. AFM images of the resulting particles are shown in Figure 43.

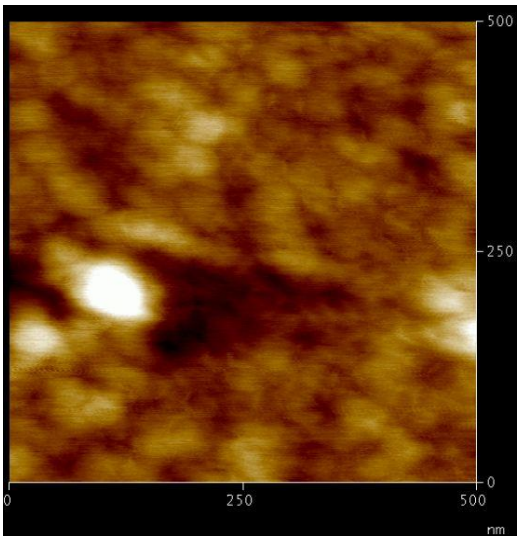

a)

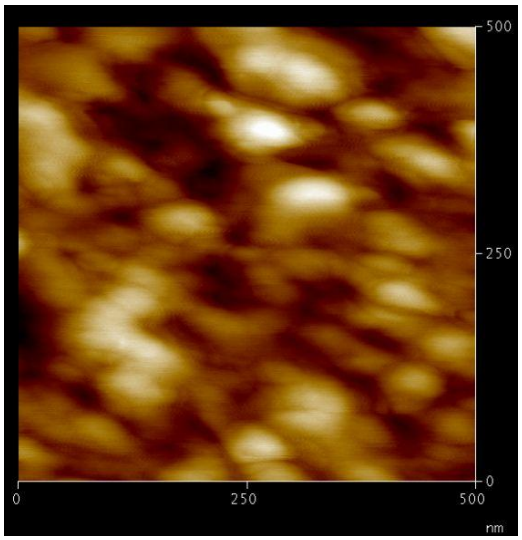

b)

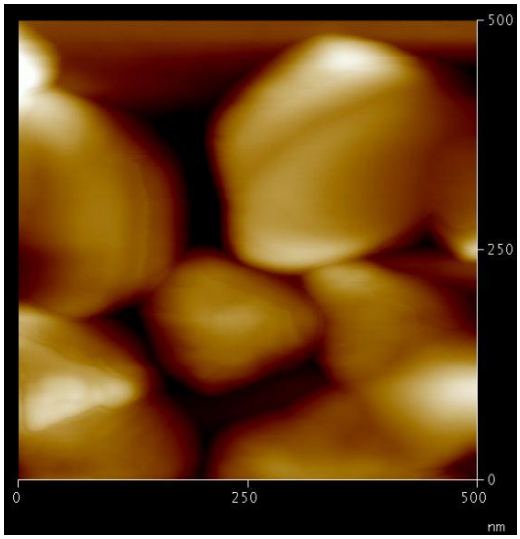

c)

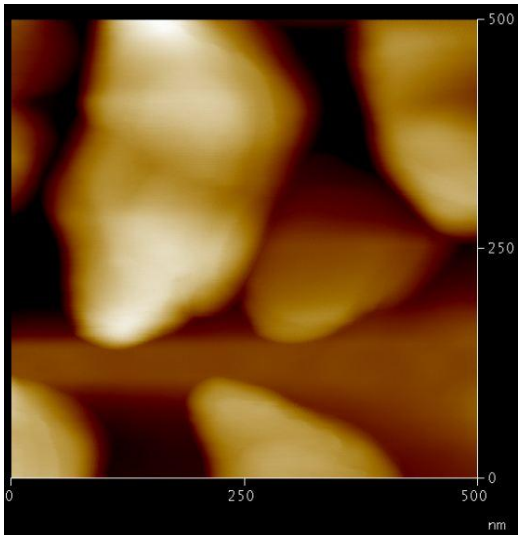

d)

Figure 43. AFM images (taken at 500nm) of 8nm gold film annealed at different temperatures for 1 hour: a) no anneal, b) 200^{o} C, c) 300^{o} C and d) 400^{o} C.

Table 5 shows the gold nanoparticle sizes for the 8 nm film annealed at different temperatures.

Table 5. Size of nanoparticles at different annealing temperatures for 8nm gold film.

Annealing Temperature	Size of nanoparticle
200^{o} C	85 nm
300^{o} C	275 nm
400^{o} C	393 nm

The transmission spectroscopy for the 8nm gold film is shown in Figure 44. Trends similar to transmission analysis of 6nm gold film are observed. The only major change is the red shift of the plasmon peak which arises from the increased particle size and the elliptical particle shape.

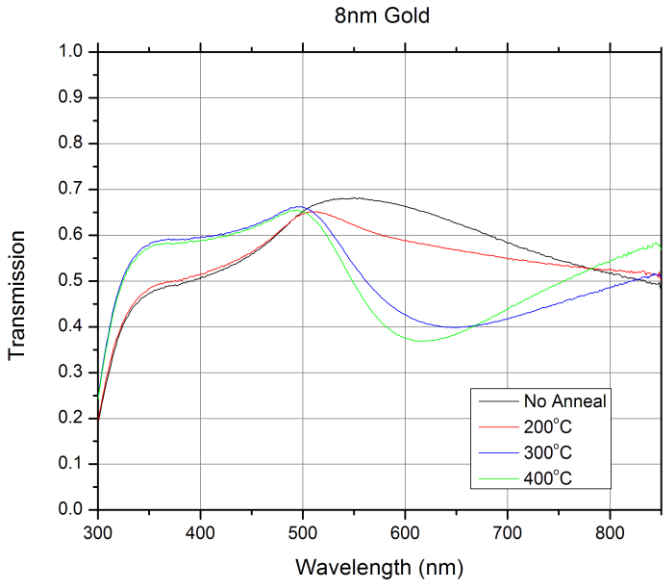

Figure 44. Transmission spectroscopy of 8nm gold film annealed at 200° C, 300° C and 400° C.

The reflection spectroscopy for the 8nm films is shown in Figure 45.

As for the case of the transmission spectroscopy, the reflection spectroscopy of 8nm gold film annealed at different temperatures also follow similar trends to the film with 6nm thickness. The only noticible change is the slight increase in reflection of the 8nm films compared to the 6nm ones.

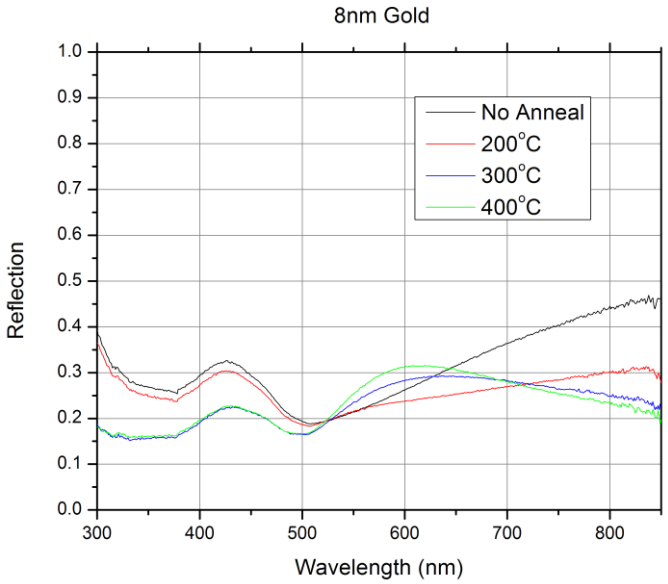

Figure 45. Reflection spectroscopy of 8nm gold film annealed at 200° C, 300° C and 400° C.

5.13 12 nm gold film thickness

Gold thickness of 12nm was deposited on the glass slide and annealed at different temperatures (200° C, 300° C and 400° C) for a period of 1 hour. AFM images of the resulting particles are shown in Figure 46. Images a) to c) were taken at a scale of 500 µm however the image d) was taken at a scale of 1um due to the large particle size. The increase in particle sizes, as we move from lower to higher temperature can be clearly seen in these images. At 400° C, the particle is no longer spherical or elliptical in shape and is more like a metal island.

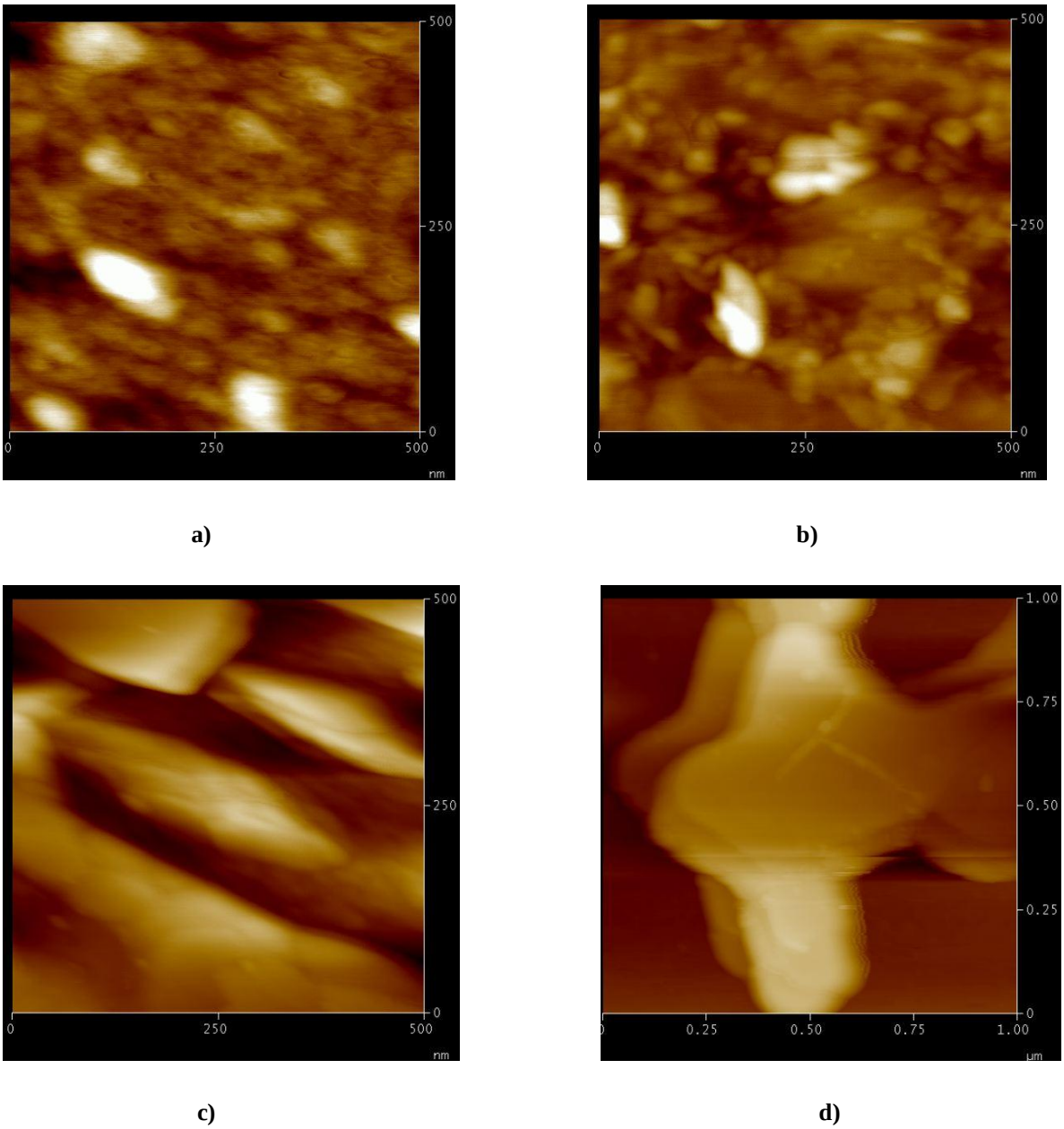

Figure 46. AFM images of 12nm gold film annealed at different temperatures for 1 hour: a) no anneal, b) 200^{o} C, c) 300^{o} C and d) 400^{o} C (taken at 1um).

Table 6 shows the gold nanoparticle sizes for the 12nm film annealed at different temperatures.

Table 6. Size of nanoparticles at different annealing temperatures for 12nm gold film.

Annealing Temperature	Size of the nanoparticle
200° C	125 nm
300° C	390 nm
400° C	N/A

At 400° C, the particle is irregular in shape and is basically a metal island, thus its exact size cannot be determined.

The transmission spectroscopy of the 12nm gold films is shown in Figure 47.

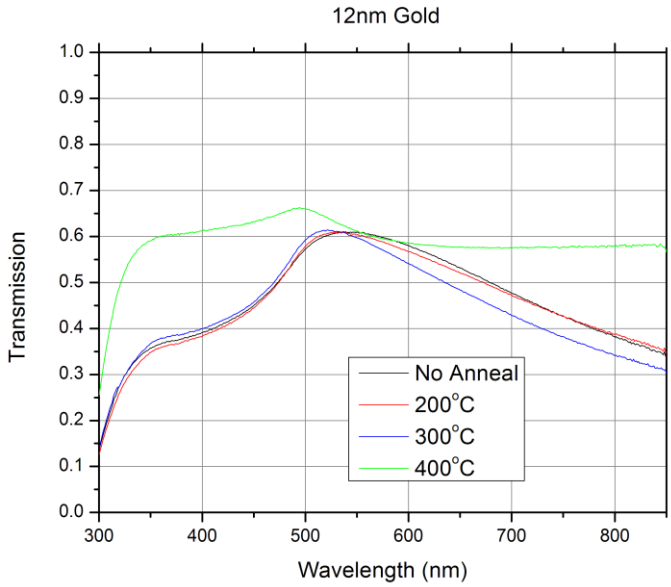

Figure 47. Transmission spectroscopy of 12nm gold film annealed at 200° C, 300° C and 400° C.

As we move from 8nm to 12nm gold thickness, we see a huge difference in the particle sizes. At 400° C, metal islands are formed. These bigger particles have very low absorption and end

up transmitting more light. The reflectance of such a film comprising of large particles is also very less (as shown in Figure 48) owing to the large spacing between particles/islands providing lot of open spaces for light to pass through.

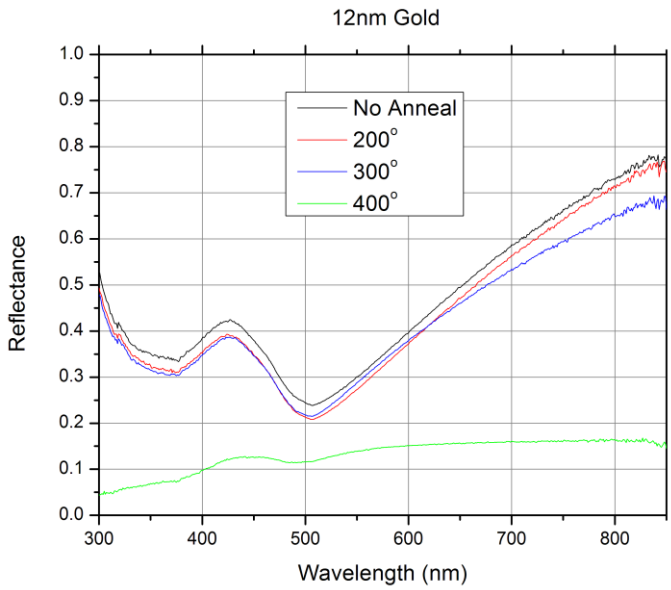

Figure 48. Reflection spectroscopy of 12nm gold film annealed at 200° C, 300° C and 400° C.

For the films annealed at lower temperatures, the particles are still spread out and acts as a near continous film. This results in light being highly reflected from these films.

After observing the optical response of different thicknesses of gold, we now make a comparison and decide on the optimum thickness of the gold film required for solar cell application. Annealing at high temperatures clearly improves the transmission and reduces the reflection upto a point.

Figure 49 shows a comparison in the transmission, reflection and absorption spectra for the 6nm, 8nm and 12nm gold film thicknesses annealed at 200° C. The temperature of 200° C was chosen for the comparison as the gold films on the solar cell would be annealed at around that temperature. The commercial solar cells have a metal grid on top and annealing

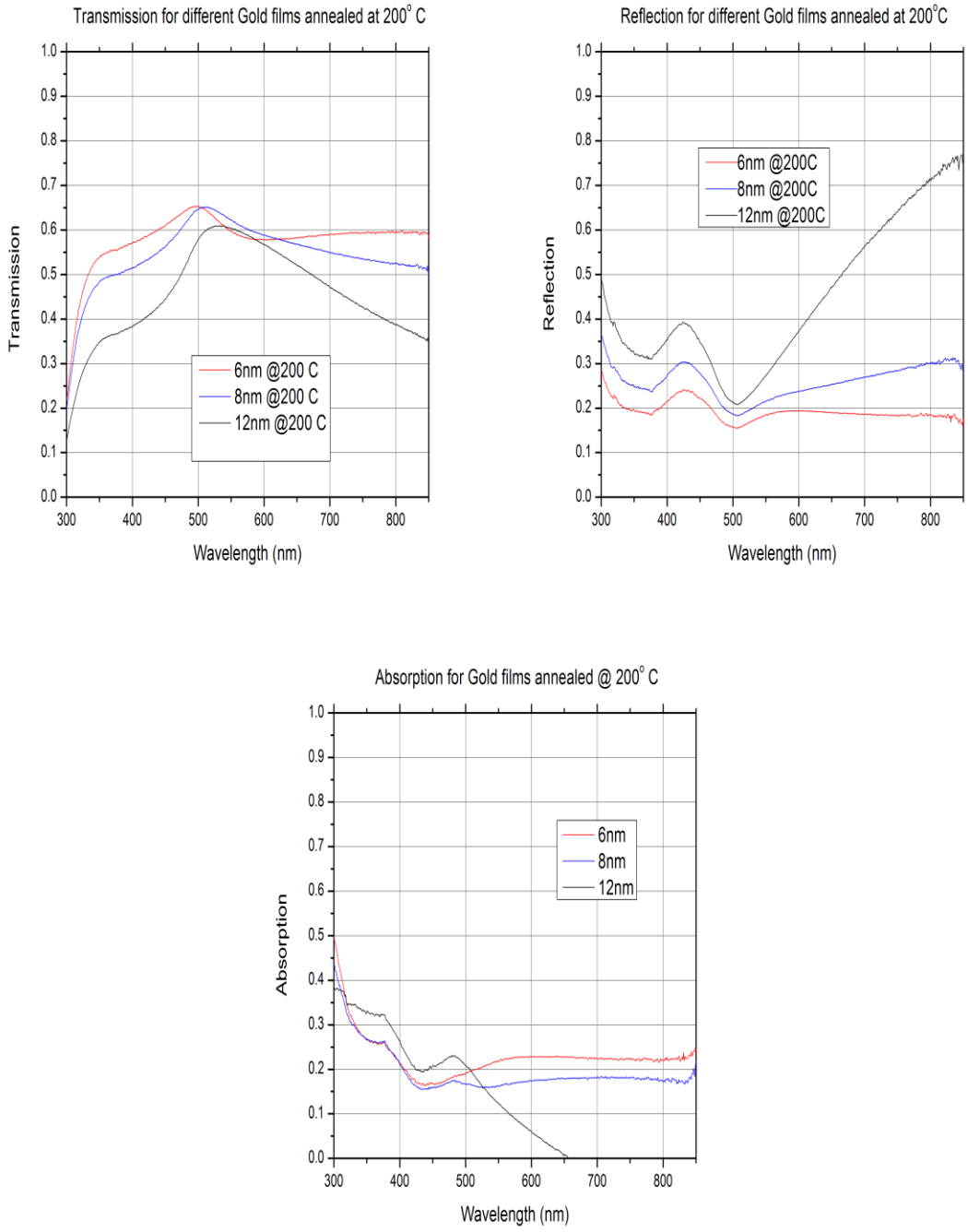

Figure 49. Comparison of the Transmission, reflection and absorption spectra of 6nm, 8nm and 12nm of gold film annealed at 200° C.

them at high temperatures would result in the melting or removal of that grid. Hence 200^{o} C was chosen as a point of reference.

From the above plots, it can be seen that for films annealed at 200^{o} C, as the film thickness increases, the transmission decreases and reflectance increases. Gold thicknesses of 6nm and 8 nm outperform 12nm in transmission and reflectance, however, absorption is really low for 12nm compared to the other two. This is expected, as the particle size becomes bigger in size, the absorption losses are less.

There is a slight error in the absorption curve (for 12nm gold film) at longer wavelengths; the absorption becomes negative as the sum of transmission and reflection becomes greater than 1. This can be a attributed to an error in calibration of the instrument during the initial setup or the inability of the IR photodetector to collect all the light. As we would expect the absorption for thicker films to be negligible at longer wavelengths, this error can be ignored.

We now compare the transmission, reflectance and absorbance of the three gold thicknesses annealed at 300^{o} C (Figure 50). Since the annealing temperature plays an important role in determining the physical shape and size of the particle which in turn affects its optical properties, choosing the right temperature is important.

By comparing the optical performances of these films annealed at 200^{o} C and 300^{o} C, we can pick the temperature which gives the best results.

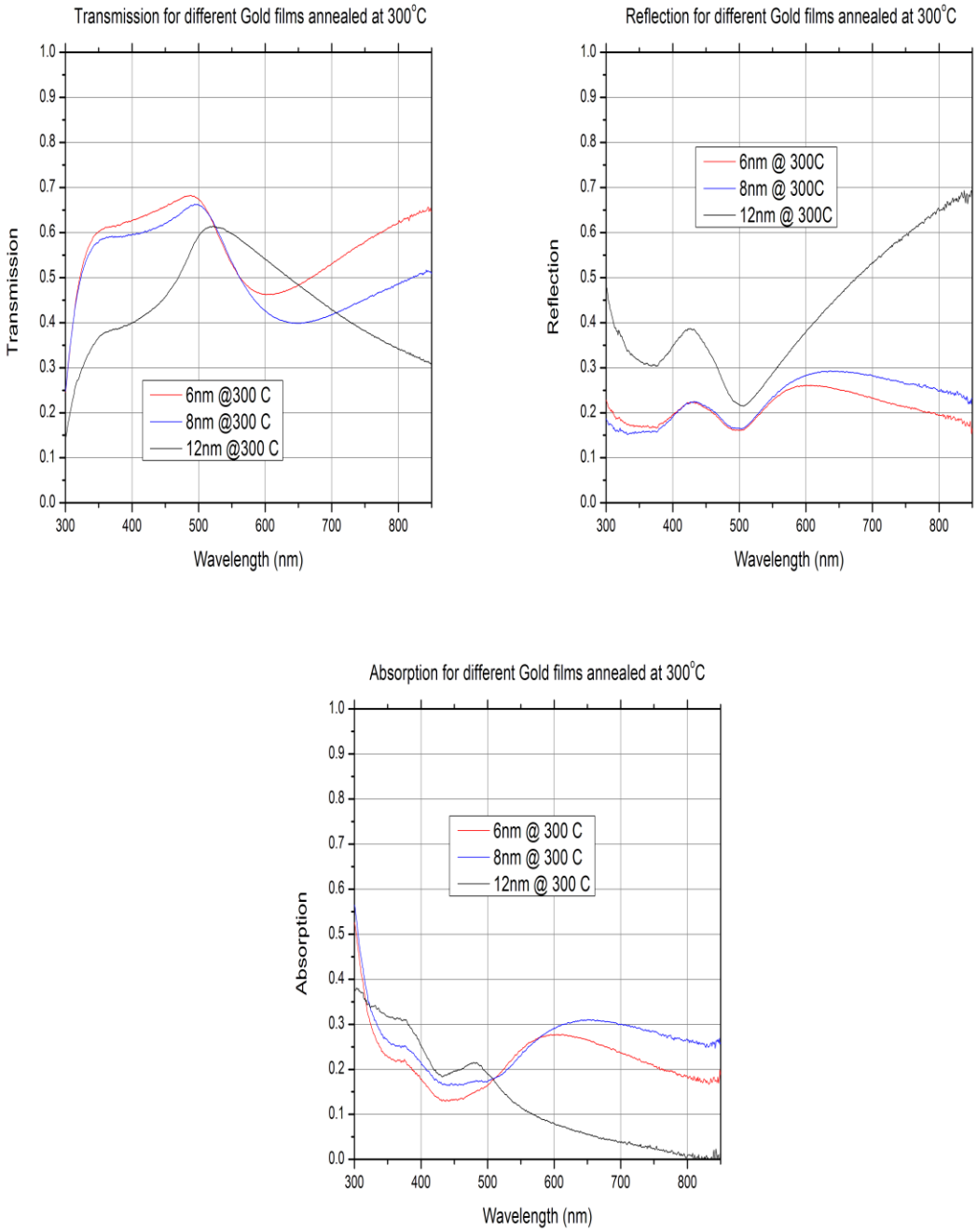

Figure 50. Comparison of the Transmission, reflection and absorption spectra of 6nm, 8nm and 12nm of gold film annealed at 300° C.

From the Figure 50, it can be clearly seen that the transmission and reflectance curves follow a general trend which was observed in Figure 49 as well. At 300^{o}C, thicknesses of 6nm and 8nm show superior optical properties suitable for solar cell application compared to the 12nm film thickness.

Absorption for the 12nm film is lower than that of 6nm and 8nm as explained earlier. Contrary to the absorption curve in Figure 49, the absorption of the 8nm film seems higher than the 6nm film. This cannot be easily explained as we would expect the thicker film to have a less absorption. It could be related to the orientation or the topography of the gold nanoparticles on the sample. Although unlikely, there could also be a glitch or an error on the part of the spectrophotometer during measurement.

We now summarize the important observations made for the thin film characterization for the annealing temperatures of 200^{o} C and 300^{o} C in table 7.

Table 7. Summary of optical properties of 6nm, 8nm and 12nm gold thicknesses annealed at 200^{o} C and 300^{o} C.

Gold Film Thickness	**Annealing at 200^{o} C**			**Annealing at 300^{o} C**		
	Transmission	**Reflection**	**Absorption (Longer Wavelength)**	**Transmission**	**Reflection**	**Absorption**
6nm	High	Low	High	High	Low	Moderate
8nm	Moderate	Moderate	Moderate	Moderate	Moderate	High
12nm	Low	High	Low	Low	High	Low

From Table 7 it can be seen that at both 200^{o}C and 300^{o}C, thinner films (6-8nm) perform well.

The films demonstrate different optical behavior at different wavelengths which in turn is affected by the annealing temperature, thus choosing one particular temperature over the other becomes a difficult task. The logical choice is to take the average of the two temperatures and use it to anneal the gold films on solar cells. Hence we take 250^{o} C as our choice of annealing temperature.

Although, we have demonstrated that thin films perform better when deposited on glass slides, it does not necessarily mean that the same thicknesses deposited on the solar cells would provide the same outcome. It is important to note that, plasmons are very sensitive to the material and dielectric environment. Variation in the structure of the solar cell can cause drastic changes in the optical properties.

Thin film characterization gave us some knowledge about how the optical properties are influenced by film thicknesses and annealing conditions. This can now serve as a starting point and we can try replicating these nanoparticles on the solar cells.

5.20 Solar Cell Characterization

Results from the thin film characterization were taken into account while replicating similar nanostructures on the solar cells. The solar cells were bought from the vendor and diced into a number of samples (20 mm x 13 mm). These were essentially single crystalline solar cells, which were processed after etching the anti-reflection coating from them.

Initially, the role of the dielectric spacer layer was investigated. Experiments were undertaken to prepare samples with and without the dielectric coating to inspect the spectral response. For all the samples, the gold films were annealed at 250^{o} C for 1 hour.

Figure 51 shows the external quantum efficiency (EQE) plot for some of these samples.

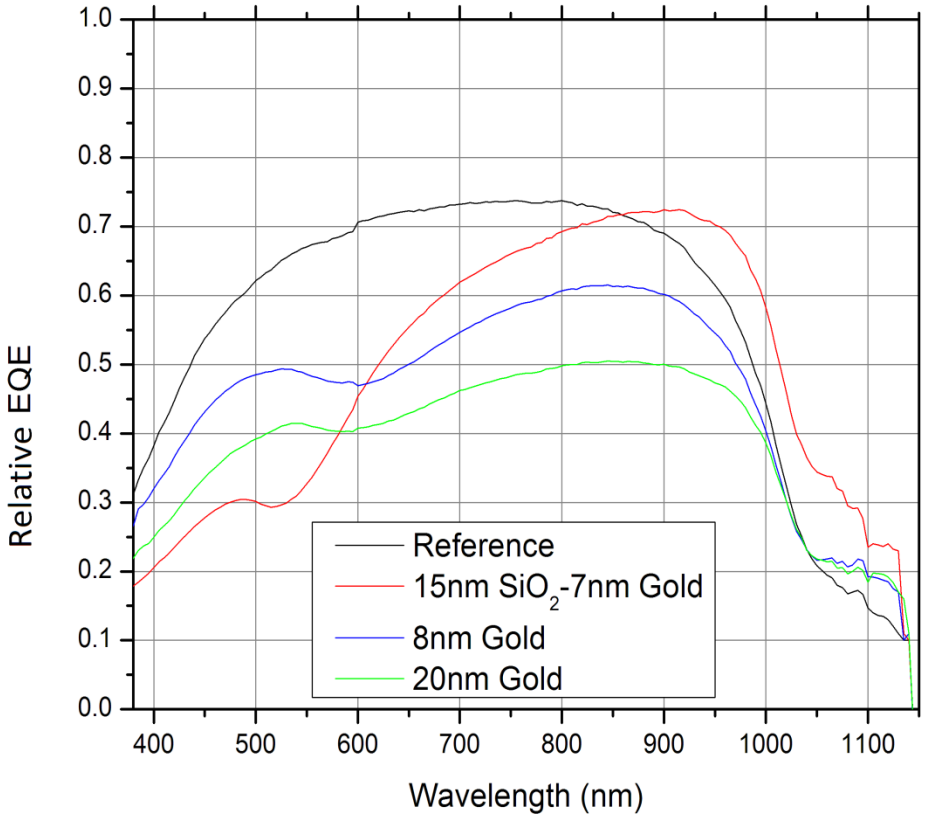

Figure 51. EQE comparison of solar cell samples of 7nm (with oxide), 8nm and 20nm gold thicknesses with the reference sample (no oxide, no gold).

From the above figure it can be observed that without the dielectric spacer layer, there is hardly any EQE enhancement apart from the slight increase at around 1050-1140 nm, which is negligible. It can also be seen, that moving from 8nm to 20 nm gold thicknesses results in a decrease in the EQE which is due to the reduced forward scattering and increased back scattering (explained in the thin film characterization section). The reference sample constitutes of the solar cell with no oxide or gold layer on top of it.

With the dielectric spacer layer, a clear increase in the EQE from the reference can be observed. At higher wavelengths (~850nm), the enhancement can be explained in terms of an increased coupling or light trapping and also due to the fact that the metal nanostructures can act as an antireflection coating (reduced reflection at higher wavelengths). Moreover, the thickness and the type of the dielectric play an important role in changing the coupling and subsequent light trapping. This would be experimented later in this section.

At shorter wavelengths, the EQE suffers due to the absorption in the metal nanoparticles. Light gets absorbed in the metal structures and gets converted into heat and thus does not couple into the semiconductor. Hence lesser number of incident photons are absorbed in the semiconductor.

The above plot provides some valuable information regarding the importance of the dielectric spacer. As mentioned earlier, no real EQE enhancement can be observed for the samples without the dielectric layer and thus keeping that in mind, all the samples which were processed later had the spacer layer prior to the gold deposition. It should also be mentioned here that our solar cell samples had a rough top surface, so depositing a spacer layer also helped in surface passivation and reducing the surface recombination.

Different gold thicknesses were deposited over different thicknesses of the dielectric spacer layer. For the dielectric spacer, SiO_2 and Si_3N_4 were considered. Table 8 compares some important properties of these two layers.

Table 8. Comparison of refractive indices and dielectric constants of SiO_2 and Si_3N_4.

Properties	**SiO_2**	**Si_3N_4**
Refractive Index	1.46	2.05
Dielectric Constant	3.9	7.5

For the following experiments, mono crystalline solar cells different from the ones shown in Figure 51 were purchased from Silicon Solar Inc.

Gold thicknesses of 6nm, 8nm, and 10nm were deposited on these solar cells and the annealing was carried out at 250^{o} C for 1 hour as before.

5.21 6nm Gold Thickness

Gold thickness of 6nm was deposited on 4 samples: 30nm SiO_2, 15nm SiO_2, 30 Si_3N_4 and 15nm Si_3N_4.

Figure 52 shows the comparison of EQE for these 4 samples with the reference sample (no dielectric layer, no gold).

From the above family of curves, it can be observed that the EQE enhancements begin to occur at around 640-680 nm. It is due to the reasons mentioned before, namely the increased light coupling due to forward scattering and the gold nanostructures acting as an anti-reflection coating at longer wavelengths. The enhancement can only be observed above the plasmon resonances when there is a constructive interference between the scattered and the incident light. Below the plasmon resonance, there is a destructive interference between the incident and the scattered light leading to a reduction in EQE.

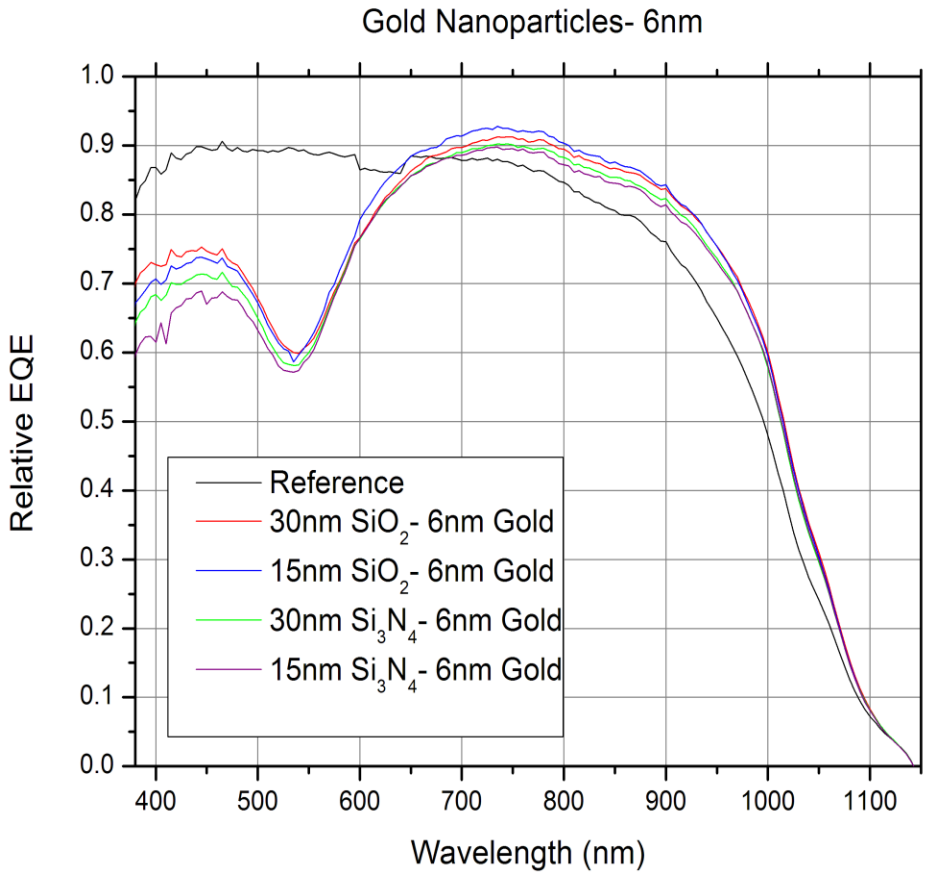

Figure 52. EQE comparison of solar cells with 15 nm and 30nm of dielectric layer (SiO_2, Si_3N_4) and 6nm of gold. The reference sample is also shown.

The dip in the EQE, observed at around 550nm is due to the increased absorption in the gold nanoparticles which can also be seen in the Figure 50 (gold absorption for 6nm film annealed at 300^{o}C). These are the plasmon resonance associated dips. The slight shift is due to the change in dielectric environment and also the slight difference in the annealing temperature (250^{o} C for this case)

Comparing the two dielectric layers, we can see that Si_3N_4 having a higher refractive index, red shifts the point where the enhancement occurs. By using SiO_2 as the dielectric layer,

more enhancements in the EQE can be observed compared to Si_3N_4. The dip around 550nm is much deeper for Si_3N_4 compared to SiO_2. This can be explained by the fact that for the same gold thickness, the particles on Si_3N_4 are smaller than the ones on SiO_2.Smaller particles have more absorption compared to bigger particles as explained previously.

Moreover, changing the dielectric thickness also results in a change in coupling. From the above curve it can be noted that by increasing the dielectric layer thickness, there is a reduction in EQE at shorter wavelengths and an increase in EQE at higher wavelengths. Also the dip shifts upwards as larger particles would have smaller absorption.

The reference sample with no oxide and no gold particles has a very high EQE. It might be possible that the etching of the anti-reflection coating from the reference sample may not be complete and there still might be some coating remaining on the sample which is causing this high EQE.

5.22 8nm Gold Thickness

Gold thickness of 8nm was deposited on 4 samples: 30nm SiO_2, 15nm SiO_2, 30 Si_3N_4 and 15nm Si_3N_4.

Figure 53 shows the comparison of EQE for these 4 samples with the reference sample (no dielectric layer, no gold)

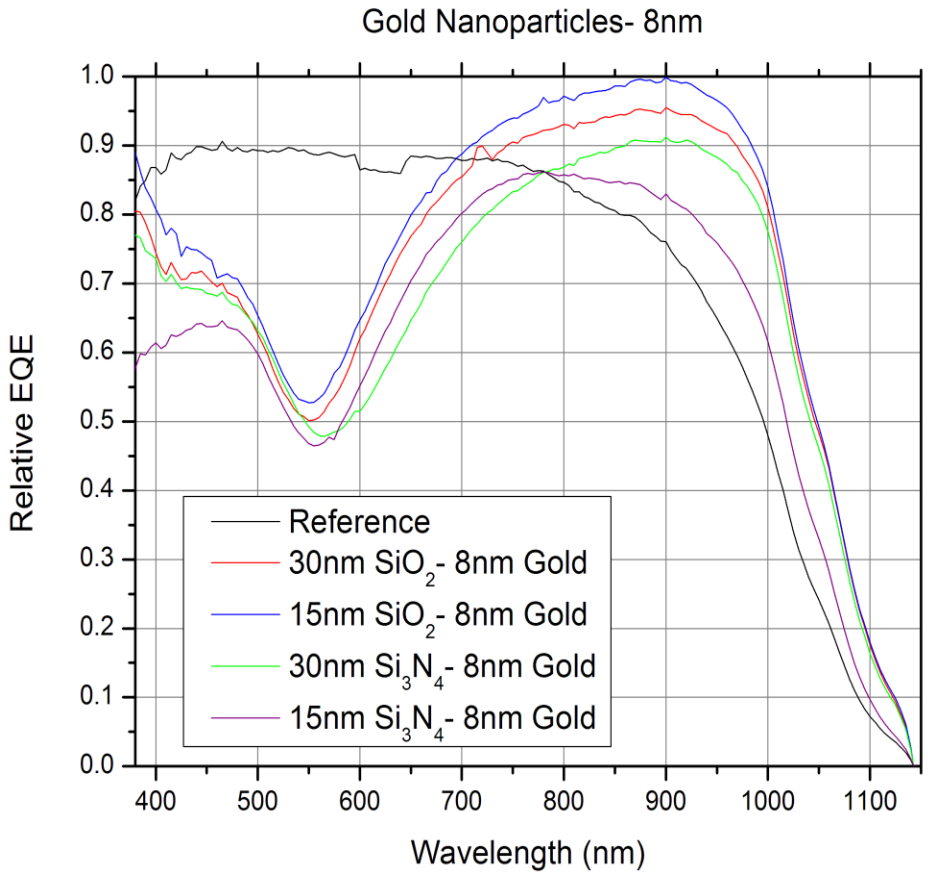

Figure 53. EQE comparison of solar cells with 15 nm and 30nm of dielectric layer (SiO_2, Si_3N_4) and 8nm of gold. The reference sample is also shown.

Similar family of curves is obtained in the above figure. The EQE enhancements begin to occur at around 680-770 nm. This red shift is expected due to the increased particle size.

As mentioned before, the dip in the EQE curve which occurs around 550-580 nm is due to the increased absorption in the gold particles. The dip for Si_3N_4 is much deeper compared to SiO_2 as before.

The sample with SiO_2 layer performs better than the layer with Si_3N_4. As again, the red shift for the high refractive index Si_3N_4 is also observed in the above curve. However the trend of

the reduction in EQE at shorter wavelengths and an increase in EQE at higher wavelengths with the increase in thickness of the dielectric layer observed in Figure 52 is not observed here. This shows the level of complexity involved in understanding the coupling behavior. The amount of light coupled into the semiconductor does not only depend on the thickness of the dielectric but also on other factors like: size of the particle, spacing between the particles and their orientation.

A really high EQE is observed for the sample with 15nm layer of SiO_2 underneath the gold. The increase of EQE at higher wavelengths exceeds the amount of decrease in EQE at shorter wavelengths leading to an overall increase in EQE over the entire spectrum.

5.23 10nm Gold Thickness

Gold thickness of 10nm was deposited on 4 samples: 30nm SiO_2, 15nm SiO_2, 30 Si_3N_4 and 15nm Si_3N_4.

Figure 54 shows the comparison of EQE for these 4 samples with the reference sample (no dielectric layer, no gold)

The EQE enhancements begin to occur at around 710-860 nm showing a significant red shift from the previous curves.

Again, SiO_2 performs better than Si_3N_4 and a deeper dip is observed for Si_3N_4 as before.

The sample with 30nm of SiO_2 shows a considerable increase at longer wavelengths compared to other samples. Even at shorter wavelengths, its response is far better than its counterparts.

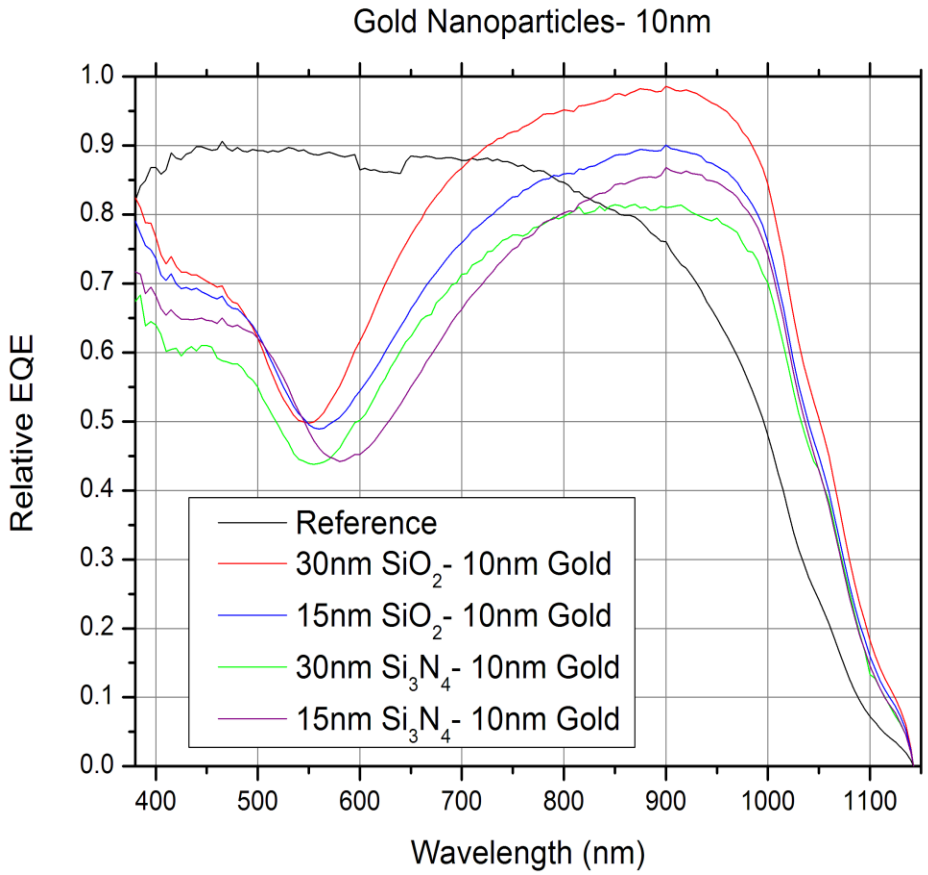

Figure 54. EQE comparison of solar cells with 15 nm and 30nm of dielectric layer (SiO_2, Si_3N_4) and 10nm of gold. The reference sample is also shown.

5.24 8nm Silver Thickness

Silver thickness of 8nm was deposited on two solar cell samples having a dielectric layer of 15 and 30nm SiO_2.

Silver is less lossy compared to gold, thus this experiment was done to improve the response at shorter wavelengths and also to have a better understanding of the plasma resonances.

Figure 55 shows the comparison of EQE for these 2 samples with the reference sample (no dielectric layer, no silver)

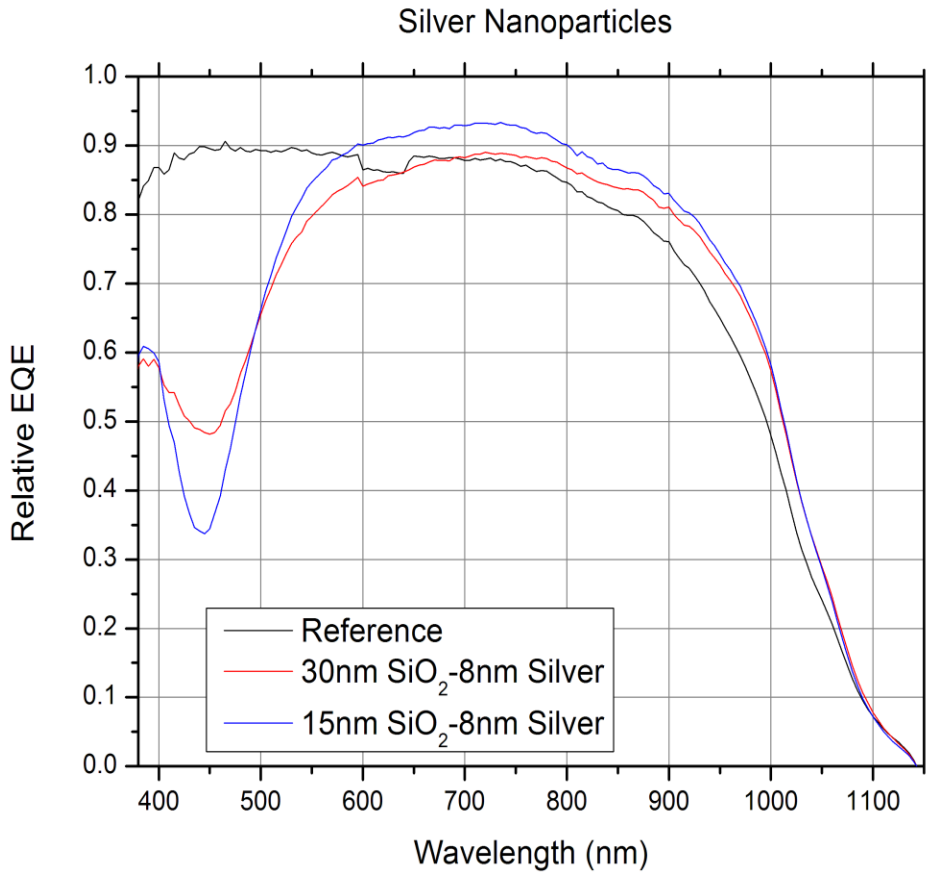

Figure 55. EQE comparison of solar cells with 15 nm and 30nm of SiO_2 layer and 8nm of silver. The reference sample is also shown.

As expected, tremendous improvements in the blue response are observed for the two samples compared to the previous gold samples. The dip in the EQE is around 440nm, which corresponds to the wavelength at which plasmon resonance occurs for silver.

Enhancements at higher wavelengths begin to occur at around 560nm for 15 nm SiO_2 and at around 700nm for the 30nm SiO_2 sample. The fall in the dip can be clearly seen as the dielectric thickness is reduced.

Although the blue response is significantly improved, the improvement in red response is not as large as observed for the gold samples with the same metal and dielectric thicknesses.

5.25 Comparison

We now compare the samples with the good results by plotting them on the same graph and observing the clear trends.

Figure 56 shows the EQE comparison of these solar cell samples.

The above plot provides a lot of information regarding the plasmonic enhancement of solar cells. A clear red shift is observed as we move from silver to gold.

A trend in the position of the dip can also be seen clearly as we move from 6 to 10nm gold film thicknesses. Better enhancement at longer wavelengths is observed for thicker films while better performance at shorter wavelengths is observed for thinner films.

The 30nm SiO_2, 8nm silver provides a good blue response compared to the gold samples but looses out in the red region, though a clear enhancement in EQE can be seen from 670nm onwards.

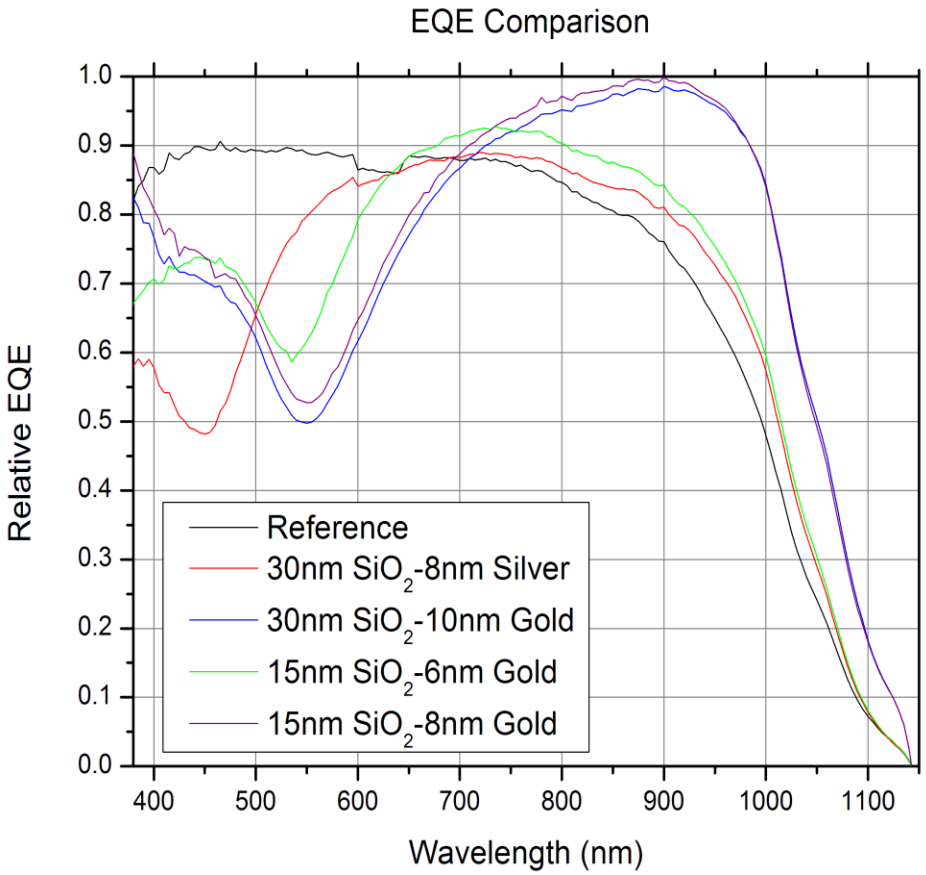

Figure 56. EQE comparisons for different solar cell samples.

Processing conditions can be engineered further and better response from silver nanoparticles can be expected.

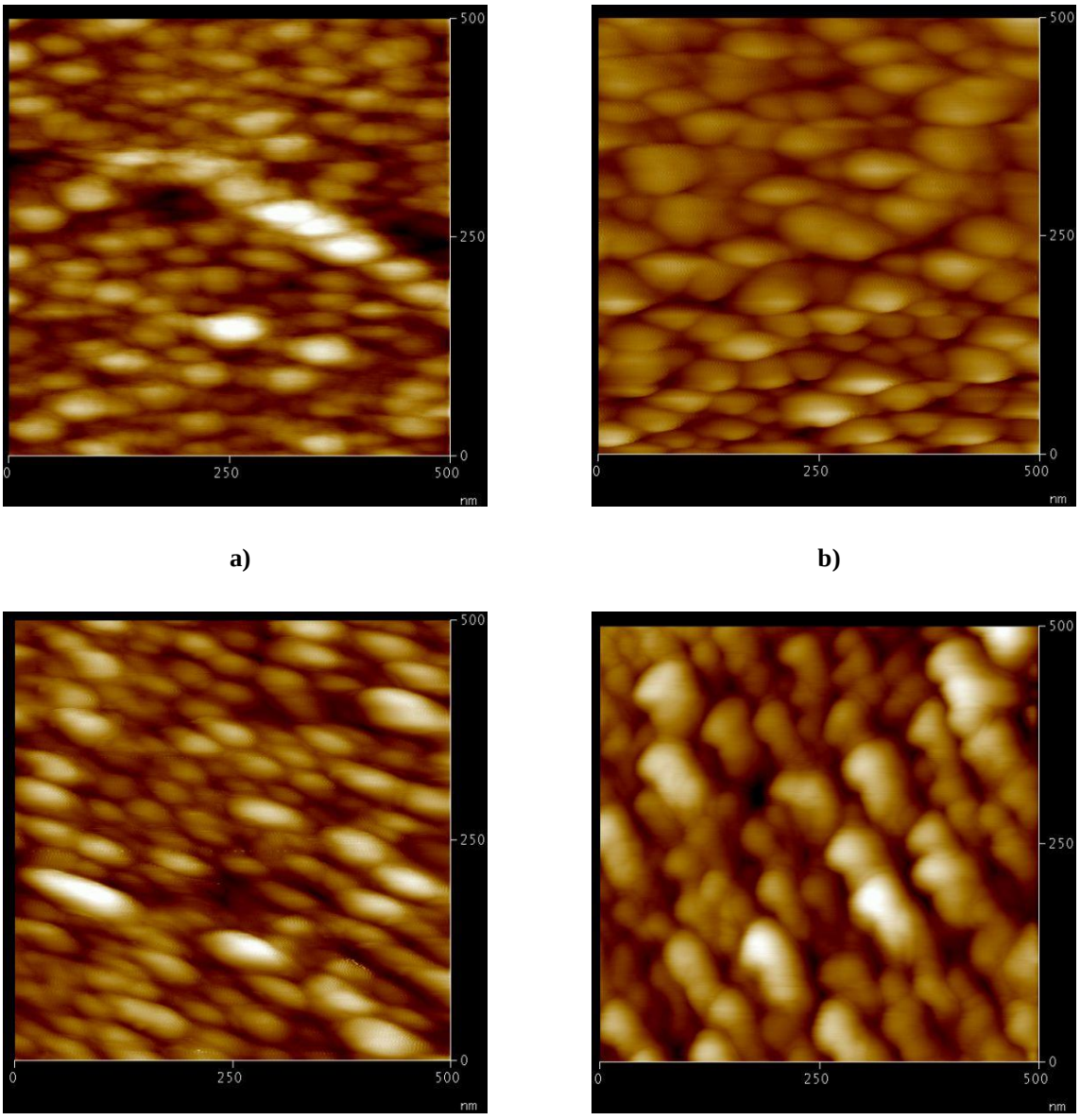

Figure 57. AFM images of a) 15nm SiO_2, 6nm gold, b) 30nm SiO_2, 8nm Silver, c) 15nm SiO_2, 8nm gold and d) 30nm SiO_2, 10nm gold.

The 15nm SiO_2, 8nm gold and 30nm SiO_2, 10nm gold samples perform really well at longer wavelengths with EQE reaching almost 1 at 900nm.

The AFM images of these 4 samples are shown above. We can observe that as we move from 6nm towards 10nm, the particles become bigger and elliptical, causing the red shift in plasmon resonances. The silver particles (image b) appear to be more spherical and uniform compared to the gold particles (a, c, d).

The photocurrent (current density) can be calculated and extracted from the EQE plot, when averaged over the AM 1.5D radiation. The various photocurrents were calculated and normalized to the reference sample.

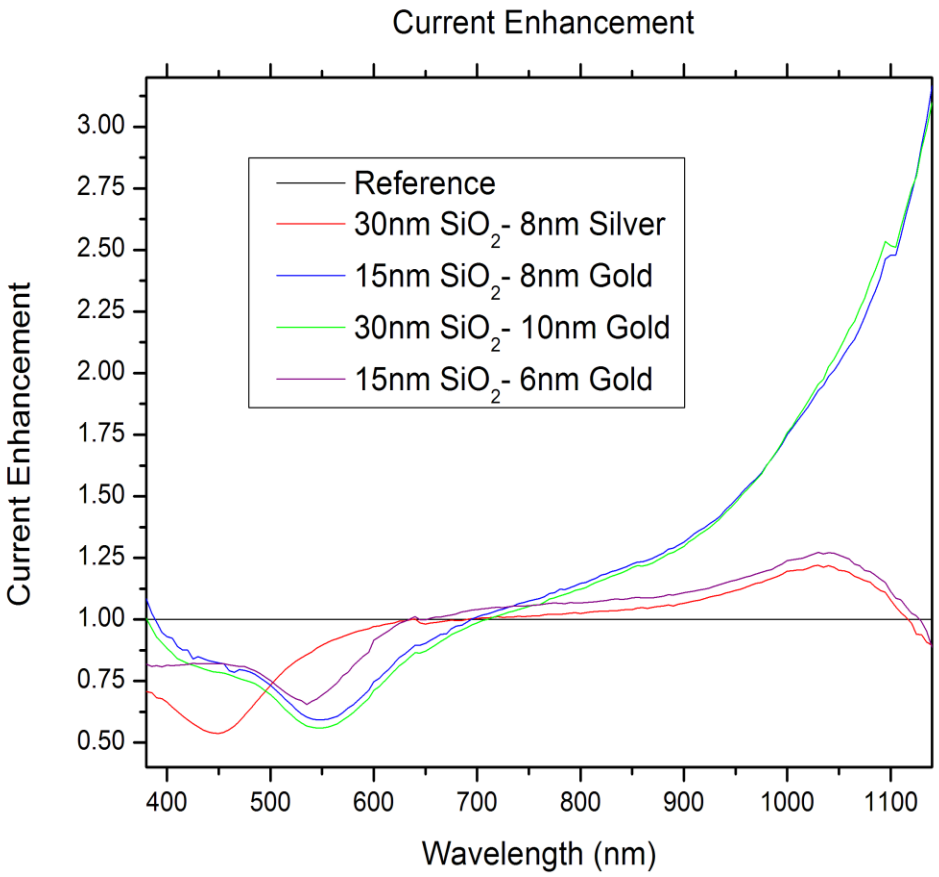

Figure 58. Photocurrent enhancement of solar cell samples relative to the reference sample.

Figure 58 shows the photocurrent enhancement of the above four solar cells relative to the reference cell.

The above plot shows that the photocurrent at shorter wavelengths is lower than that of the reference sample due to the absorption in the nanoparticles; however the enhancements at longer wavelengths are significant.

For the two samples: 15nm SiO_2, 8nm gold and 30nm SiO_2 and 10nm gold, the photocurrent enhancement at the longer wavelengths overshadows the depreciation at shorter wavelengths, giving an overall increase the current density.

At 1100nm the photocurrent is increased by a factor of 2.5 and around 1140nm it is almost a factor of 3, which is considerable.

Table 9 compares the current density for these solar cell samples with the reference and the change in the overall current density.

Table 9. Current density and the total change in current density for different solar cell samples.

Solar Cell Sample	**Jsc (mA/cm^2)**	**Change in Total Jsc**
Reference	29.20	-
30nm SiO_2- 8nm Silver	27.84	↓ 4.88 %
30nm SiO_2- 10nm Gold	29.46	↑ 0.89 %
15nm SiO_2- 6nm Gold	28.53	↓ 2.29 %
15nm SiO_2- 8nm Gold	30.15	↑ 3.25 %

Enhancement in photocurrent over the entire wavelength range is observed for 30 nm SiO_2, 10 nm gold (0.89%) and 15nm SiO_2, 8nm gold (3.25%). This percentage could be further increased with a better control over the size, shape and spacing between the metal nanoparticles.

The rest of the samples don't show an overall increase in the photocurrent, however they still show a significant amount of increase at longer wavelengths. The degradation of performance by silver nanoparticles can be attributed to some extent, to the oxidation effects which might be occurring between the time of deposition and the time of EQE measurement. The exact nature of the oxidation effect on the optical properties of silver is not known.

The complexity of the plasmon phenomenon is too deep and thus the results that have been obtained in this research can't be generalized for other solar cell structures. For the solar cell application, it is essential to obtain a decent coupling of light into the semiconductor to demonstrate an overall enhancement in the performance.

Small variations in the processing conditions can cause drastic effects as shown by the above results and the key to maximize the enhancement is to get the right structure.

This research has demonstrated an enhancement in photocurrent like the studies mentioned in the literature review section. An important thing to note here is that the samples used in this research were wafer based solar cells hence the potential of enhancement is not much compared to the other thin film solar cells used in the previous studies. The wafer based cells already absorb a good amount of light in the visible region thus the effect of plasmons isn't significant in that region. In particular, the thickness of the solar cell is important in determining the effectiveness of this approach.

This study can be applied directly to silicon photodiodes and can be engineered to provide good sensitivities at particular wavelengths (as the requirement) by tuning the plasmon resonances.

5.26 Summary

Thin film characterization of gold films was done to understand the plasmon behavior and served as a platform to engineer the same nanostructures on the silicon solar cells. The optical spectroscopy namely the transmission, reflection and absorption measurements were performed to figure out the right particle size for the best performance. The annealing conditions were also decided by these experiments.

An attempt to enhance the photocurrent of silicon solar cells was made. The dielectric environment was altered to observe the effect in EQE and to understand the coupling of light into the semiconductor.

Enhancement in EQE and photocurrent response of the solar cells was demonstrated at longer wavelengths where the reference silicon solar cell performed poorly.

CHAPTER 6

CONCLUSION & FUTURE WORK

6.10 Conclusion

The goal of this thesis was to study the plasmonic enhancement of silicon solar cells. Metal nanoparticles of gold and silver were employed in this study.

Thin film characterization of gold films was done initially to understand the plasmon behavior for different processing conditions. Nanoparticles of different sizes were obtained by annealing the films at different conditions. The optical spectroscopy was done to explore the transmission, reflection and absorption in the gold films. The results obtained were directly applied to solar cells.

An attempt to enhance the photocurrent of solar cells by increasing scattering and light trapping and subsequent absorption was made. Efforts to improve the efficiency of silicon solar cells near its band gap proved fruitful. Gold nanoparticles showed more absorption compared to silver nanoparticles, however more enhancements at longer wavelengths was observed for the former compared to their counterpart. The dielectric environment was varied in terms of type of the dielectric and its thickness. It was shown by the EQE plots that SiO_2 fared much better than Si_3N_4, although Si_3N_4 having a higher refractive index red shifted the wavelength at which the enhancement occurred. Thicknesses of the dielectrics were experimented in order to get better coupling of light into the semiconductor.

This research was successful in demonstrating an overall 3.25 % increase in the photocurrent of mono crystalline solar cells. A high EQE and photocurrent was observed above 800nm for almost all the samples. A 2.5 fold increase in photocurrent was observed at 1100 nm and a 3 fold increase at 1130 nm.

This research can be directly applied for thin film solar cells and silicon photodiodes. Much work still needs to be done in this area as many concepts relating to the plasmon theory are not easily understood.

6.20 Future Work

A lot of work still needs to be done to understand the important concepts of plasmon theory and its applicability to solar cells. Many techniques can be employed and plenty more experiments can be performed which are beyond the scope of this master's thesis to provide a clear picture of the physics relating to surface plasmons.

6.21 Copper Nanoparticles

Like gold and silver, copper nanoparticles can be similarly fabricated on solar cells to observe a high degree of enhancement in photocurrent. The plasmon resonance frequency of copper is greater than that of gold so it is expected to red shift the enhancement to even longer wavelengths and is a potential candidate for achieving a decent increase in efficiency.

6.22 Fabrication of Nanoparticles using Anodized Aluminum Oxide

The metal nanoparticle size and the distance between two particles (pitch) can be accurately controlled and experimented to provide a more complete study. Spacing and the size of the nanoparticles play an important role in determining the amount to coupling of light into the semiconductor.

Using Anodized Aluminum Oxide (AAO) template assisted approach; high density nanoparticle arrays can be fabricated. This technique enables deposition of a wide range of nanoparticle materials over large areas of surfaces simultaneously and it reasonably inexpensive, though it involves a fair amount of processing steps. The templates can be

produced by evaporation of aluminum onto the substrate and subsequent anodization of the aluminum to produce the resulting nanoporous alumina films. The pore sizes of these templates can be tuned within the range of ~25 to ~100 nm [1]. A final chemical etch step is required to make sure that the pores extend deep through the template onto the underlying substrate. Figure 59 shows the schematic of the various steps involved in this process.

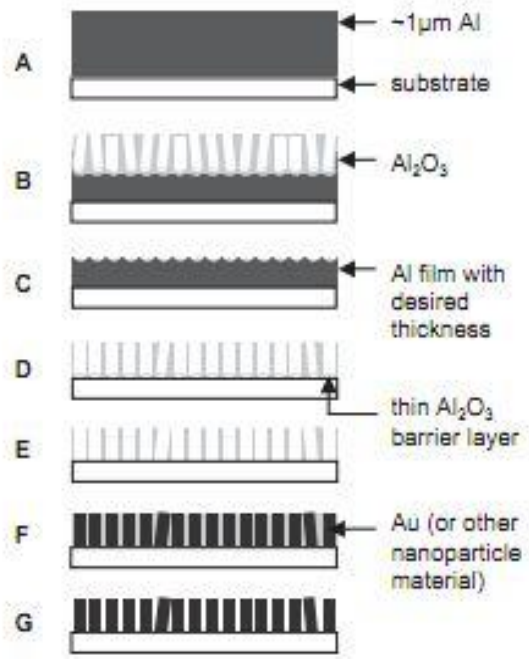

Figure 59. (A-G) Schematic of typical process used to fabricate nanoparticle arrays on surface using alumina template approach [1].

The process flow is listed below:

a) Evaporation of a ~1µm thick aluminum film onto the substrate.
b) Partial anodization of the film (~500-900 nm) by using oxalic or sulfuric acid baths.
c) Removal of the first alumina film by chemical etching (typically phosphoric acid) to leave a patterned Al film.

d) Anodization of the remaining Al, leaving behind a thin barrier layer at the bottom of the pores.
e) Removal of the barrier layer with a short chemical etch.
f) Nanoparticle material deposition into the template pores.
g) Removal of the template, leaving behind the nanoparticle array.

Figure 60 shows an SEM image of gold nanodot arrays fabricated using this method.

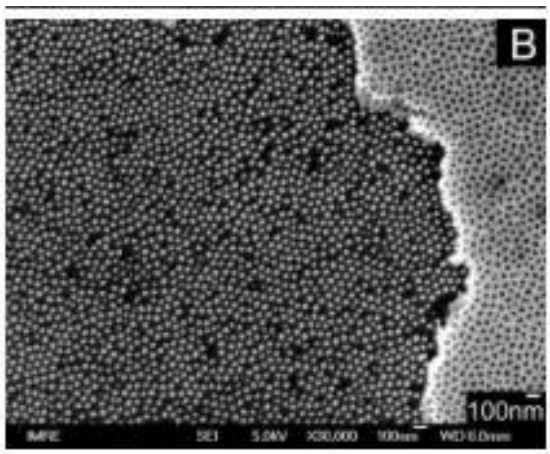

Figure 60. SEM image (top view) of gold nanodot array with an average dot diameter of 38 nm ± 9nm.The templates have been partially removed using adhesive tape to reveal the Au dots on the surface [1].

6.23 Fabricating Nanoparticles using Interference Lithography

Lithographic Techniques offer best control over nanoparticle size, shape, and spacing; however these techniques can be expensive, limited to serial processing and suitable to only a small number of material systems [1]. Laser interference lithography (LIL) enables to pattern periodic structures over a large area. Its principle involves interference of two coherent light beams to form a horizontal standing wave producing a periodic pattern which can be recorded on the photoresist. The period (P) of this pattern is dependent on the wavelength of

light (λ) and the half angle (θ) of the two incident beams. A second exposure is done after a 90^{o} rotation of the sample, to create a grid pattern on the photoresist. After the pattern transfer, this periodic structure can be used as a template for forming metal nanoparticles [2]. To explain LIL in detail, a Lloyd's mirror configuration is considered and is shown in Figure 61.

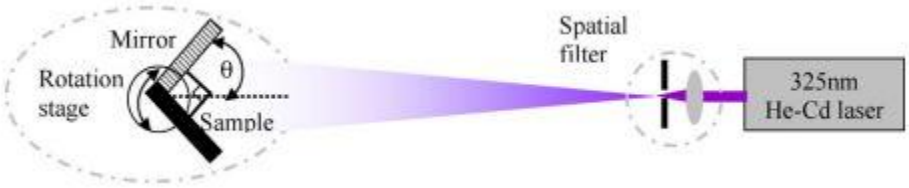

Figure 61. Lloyd's mirror configuration setup [2].

A 15mW He-Cd laser at 325nm is used as a light source. The mirror and the sample holder are fixed perpendicular to each other. Half of the expanded beam can be reflected by the mirror and be made to interfere with the other half which falls on the substrate. Since the mirror surface flatness and high reflectance at different incidence angles play an important role in enhancing the beam interference contrast, A UV-enhanced aluminum coating mirror can be applied to achieve equal reflectance at different incident angles. A spatial filter is also employed to remove the high frequency noise from the beam [2].

The work of Xie et. al. has been investigated for this section in order to provide a detailed discussion of LIL.

Low fringe contrast problem arises due to inability to adjust accurately the equalness of the two lasers for constructive and destructive interference, resulting in lithographic errors. A 100 nm thick i-line positive photoresist PFI-88 A6 can be used to overcome the low fringe contrast problem. Figure 62 shows the schematic drawing of the two beam interference and double layer resist stack coating employed by Xie's group.

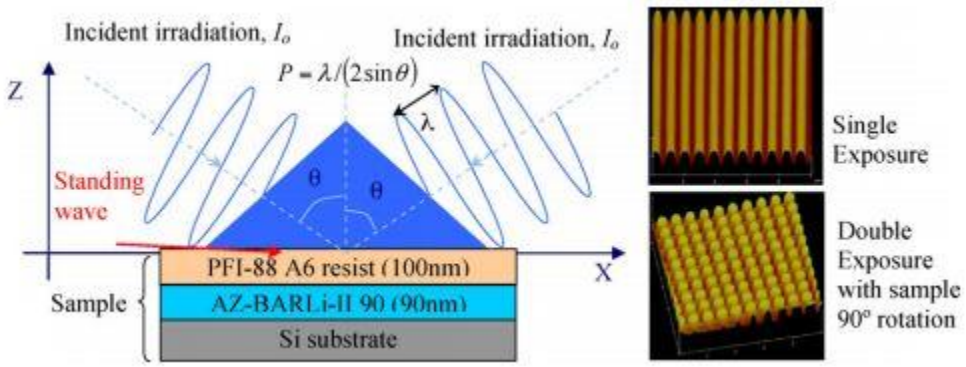

Figure 62. Schematic drawing showing standing wave of two beam interference and double layer resist stack for pattern recording [2].

An anti-reflection coating of AZ-BARLi-II 90 was coated on the Si substrate to provide a uniform dot pattern with smooth and round edge quality.

The horizontal standing wave interference period can be calculated from $\boldsymbol{p = \lambda/(2\,sin\,\theta)}$ [2]

For the positive photoresist in LIL, after double exposure and develop, the resulting dot patterns are shown in Figure 63 along with the process parameters.

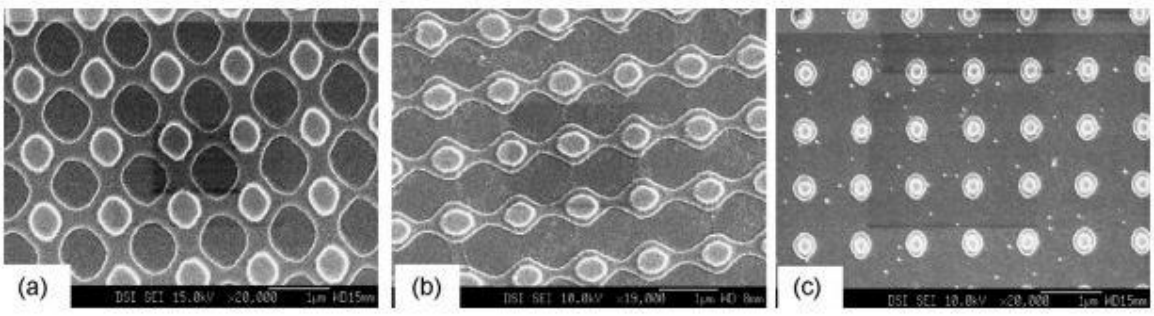

Figure 63. SEM images of dot pattern with different exposure time. Substrate: Si (1 0 0), ARC: AZ-BARLi-II 90, resist: PFI-88 A6, thinner: 2-heptanone resist-thinner ratio: 2:3, developer: CD-26, ARC spin coating: 3000 rpm for 60s, two steps ARC baking: 100° C for 60 s and 180°C for 90s, resist spin coating: 4000 rpm for 60s, resist baking: 90°C for 90 s, LIL angle: 10°, develop time: 45 s. The exposure time is: (a) 2.5 min, (b) 3min and (c) 6min [2].

In the above figure, the dots represent the places where the photoresist is remaining since a positive photoresist was used. It can be seen that such a pattern can be used as a template for

fabricating periodic metal nanoparticles. By evaporating/sputtering metal onto this template and a subsequent lift-off, a periodic arrangement of metal nanoparticles could be obtained. This approach gives provides an excellent control over the nanoparticle size and pitch.

Thus using LIL to pattern substrates provides an easy alternative to the AAO approach and can be used to fabricate periodic metal nanoparticles viably.

6.24 References

[1] Sander, M.S., "Nanoparticle Arrays on Surfaces Fabricated Using Anodic Alumina Films as Templates". Advanced functional materials (1616-301X), 13 (5), p. 393, 2003.

[2] Xie Q., "Fabrication of nanostructures with laser interference lithography". Journal of alloys and compounds (0925-8388), 449 (1-2), p. 261, 2008.

Other references:

[14] Y. A. Akimov, et al., "Nanoparticle-enhanced thin film solar cells: Metallic or dielectric nanoparticles?," Applied Physics Letters, vol. 96, Feb 2010.

[15] Y. A. Akimov, et al., "Surface Plasmon Enhancement of Optical Absorption in Thin-Film Silicon Solar Cells," Plasmonics, vol. 4, pp. 107-113, Jun 2009.

[16] F. J. Beck, et al., "Asymmetry in photocurrent enhancement by plasmonic nanoparticle arrays located on the front or on the rear of solar cells," Applied Physics Letters, vol. 96, Jan 2010.

[17] F. J. Beck, et al., "Tunable light trapping for solar cells using localized surface plasmons," Journal of Applied Physics, vol. 105, Jun 2009.

[18] R. Biswas, et al., "Surface Plasmon Enhancement of Optical Absorption of Thin Film A-SI:H Solar Cells," in 2009 34th Ieee Photovoltaic Specialists Conference, Vols 1-3, 2009, pp. 1903-1906.

[19] K. R. Catchpole and S. Pillai, "Surface plasmons for enhanced silicon light-emitting diodes and solar cells," Journal of Luminescence, vol. 121, pp. 315-318, Dec 2006.

[20] A. Dhawan and J. F. Muth, "Plasmon resonances of gold nanoparticles incorporated inside an optical fibre matrix," Nanotechnology, vol. 17, pp. 2504-2511, May 2006.

[21] V. E. Ferry, et al., "Plasmonic Nanostructure Design for Efficient Light Coupling into Solar Cells," Nano Letters, vol. 8, pp. 4391-4397, Dec 2008.

[22] C. Hagglund, et al., "Electromagnetic coupling of light into a silicon solar cell by nanodisk plasmons," Applied Physics Letters, vol. 92, Feb 2008.

[23] B. Lamprecht, et al., "Metal nanoparticle gratings: Influence of dipolar particle interaction on the plasmon resonance," Physical Review Letters, vol. 84, pp. 4721-4724, May 2000.

[24] P. Matheu, et al., "Metal and dielectric nanoparticle scattering for improved optical absorption in photovoltaic devices," Applied Physics Letters, vol. 93, Sep 2008.

[25] K. Nakayama, et al., "Plasmonic nanoparticle enhanced light absorption in GaAs solar cells," Applied Physics Letters, vol. 93, Sep 2008.

[26] C. Noguez, "Surface plasmons on metal nanoparticles: The influence of shpae and physical environment," Journal of Physical Chemistry C, vol. 111, pp. 3806-3819, Mar 2007.

[27] B. S. Richards, "Comparison of TiO2 and other dielectric coatings for buried-contact solar cells: a review," Progress in Photovoltaics, vol. 12, pp. 253-281, Jun 2004.

[28] D. M. Schaadt, et al., "Enhanced semiconductor optical absorption via surface plasmon excitation in metal nanoparticles," Applied Physics Letters, vol. 86, Feb 2005.

[29] H. R. Stuart and D. G. Hall, "Absorption enhancement in silicon-on-insulator waveguides using metal island films," Applied Physics Letters, vol. 69, pp. 2327-2329, Oct 1996.

[30] H. R. Stuart and D. G. Hall, "Enhanced dipole-dipole interaction between elementary radiators near a surface," Physical Review Letters, vol. 80, pp. 5663-5666, Jun 1998.

[31] H. R. Stuart and D. G. Hall, "Island size effects in nanoparticle-enhanced photodetectors," Applied Physics Letters, vol. 73, pp. 3815-3817, Dec 1998.

[32] S. P. Sundararaian, et al., "Nanoparticle-induced enhancement and suppression of photocurrent in a silicon photodiode," Nano Letters, vol. 8, pp. 624-630, Feb 2008.

[33] F. J. Tsai, et al., "Absorption enhancement of an amorphous Si solar cell through surface plasmon-induced scattering with metal nanoparticles," Optics Express, vol. 18, pp. A207-A220, Jun 2010.

[34] Z. L. Wang, et al., "Three-dimensional self-assembly of metal nanoparticles: Possible photonic crystal with a complete gap below the plasma frequency," Physical Review B, vol. 64, Sep 2001.

[35] E. T. Yu, et al., "Plasmonic nanoparticle scattering for enhanced performance of photovoltaic and photodetector devices - art. no. 70331V," in Plasmonics: Nanoimaging, Nanofabrication, and Their Applications Iv. vol. 7033, S. Kawata, et al., Eds., 2008, pp. V331-V331.